

DTIC FILE COPY

4

NSWC TR 88-394

AD-A223 047

**AN EXPERIMENTAL STUDY OF THE PLASMA
FOCUS DEVICE AS A CHARGED PARTICLE
ACCELERATOR**

BY DR. RALPH F. SCHNEIDER

RESEARCH AND TECHNOLOGY DEPARTMENT

1 NOVEMBER 1988

Approved for public release; distribution is unlimited.

DTIC
ELECTE
JUN 21 1990
S E D
CD



NAVAL SURFACE WARFARE CENTER

Dahlgren, Virginia 22448-5000 • Silver Spring, Maryland 20903-5000

90 06 21 061

UNCLASSIFIED

SECURITY CLASSIFICATION OF THIS PAGE

REPORT DOCUMENTATION PAGE

1a. REPORT SECURITY CLASSIFICATION UNCLASSIFIED			1b. RESTRICTIVE MARKINGS	
2a. SECURITY CLASSIFICATION AUTHORITY			3. DISTRIBUTION/AVAILABILITY OF REPORT Approved for public release; distribution is unlimited.	
2b. DECLASSIFICATION/DOWNGRADING SCHEDULE			5. MONITORING ORGANIZATION REPORT NUMBER(S)	
4. PERFORMING ORGANIZATION REPORT NUMBER(S) NSWC TR 88-394			7a. NAME OF MONITORING ORGANIZATION	
6a. NAME OF PERFORMING ORGANIZATION Naval Surface Warfare Center		6b. OFFICE SYMBOL (If applicable) R41	7b. ADDRESS (City, State, and ZIP Code)	
6c. ADDRESS (City, State, and ZIP Code) White Oak Laboratory 10901 New Hampshire Avenue Silver Spring, MD 20903-5000			9. PROCUREMENT INSTRUMENT IDENTIFICATION NUMBER	
8a. NAME OF FUNDING/SPONSORING ORGANIZATION		8b. OFFICE SYMBOL (If applicable)	10. SOURCE OF FUNDING NOS.	
8c. ADDRESS (City, State, and ZIP Code)			PROGRAM ELEMENT NO.	PROJECT NO.
			TASK NO.	WORK UNIT NO.
11. TITLE (Include Security Classification) An Experimental Study of the Plasma Focus Device as a Charged Particle Accelerator				
12. PERSONAL AUTHOR(S) Schneider, Dr. Ralph E.				
13a. TYPE OF REPORT Final		13b. TIME COVERED FROM 10/82 TO 5/85	14. DATE OF REPORT (Yr., Mo., Day) 1988, November, 01	15. PAGE COUNT 128
16. SUPPLEMENTARY NOTATION				
17. COSATI CODES			18. SUBJECT TERMS (Continue on reverse if necessary and identify by block number)	
FIELD	GROUP	SUB. GR.		
20	19		Plasma focus Electron beam Ion beam Thomson spectrometer	
19. ABSTRACT (Continue on reverse if necessary and identify by block number) The dense plasma focus has been investigated at many laboratories as a possible fusion device. Typical plasma parameters for this device are electron temperatures of 1 keV, densities of 10^{19} per cc, and confinement times of 100 ns. Characteristic of the plasma focus discharge are intense soft and hard x-ray, optical and microwave radiations. Also, emitted from the focus are electrons, ions and, with certain filling gases, neutrons. The emphasis of this work is to investigate the electron and ion emission from the plasma focus and the development of appropriate diagnostics to accomplish this task. The viewpoint of the focus as a bipolar diode may provide a natural description of the observed phenomena. A Mather geometry plasma focus device has been constructed. Diagnostics used for electron measurements include current monitors, a calorimeter, a magnetic energy analyzer, and an emittance meter. Ion beam measurements were performed using a flux-meter, a pinhole camera, an ion beam emittance meter, and a Thomson parabola analyzer. (Cont.)				
20. DISTRIBUTION/AVAILABILITY OF ABSTRACT <input checked="" type="checkbox"/> UNCLASSIFIED/UNLIMITED <input type="checkbox"/> SAME AS RPT <input type="checkbox"/> DTIC USERS			21. ABSTRACT SECURITY CLASSIFICATION UNCLASSIFIED	
22a. NAME OF RESPONSIBLE INDIVIDUAL Dr. Ralph E. Schneider			22b. TELEPHONE NUMBER (Include Area Code) (301) 394-2345	22c. OFFICE SYMBOL R41

DD FORM 1473, 84 MAR

83 APR edition may be used until exhausted
All other editions are obsoleteUNCLASSIFIED
SECURITY CLASSIFICATION OF THIS PAGE

UNCLASSIFIED

SECURITY CLASSIFICATION OF THIS PAGE

Block 19. (Abstract) (Cont.)

In addition, opening switch behavior has been investigated. Intense electron beams are observed with pulse lengths approximately 5 ns at energies of 20 to 200 keV and currents of 1 kA and above. The root-mean-square (rms) emittance of the electron beam is found to be approximately 1 cm-rad. Ion measurements show copious ion emission of very energetic ions up to several MeV. A measurement of rms emittance of the ion beam was made. Results support the bipolar diode model of the plasma focus device.

UNCLASSIFIED

SECURITY CLASSIFICATION OF THIS PAGE

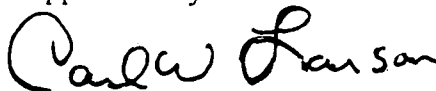
FOREWORD

The dense plasma focus has been investigated at many laboratories as a possible fusion device. Typical plasma parameters for this device are electron temperatures of 1 keV, densities of 10^{19} per cc, and confinement times of 100 ns. Characteristic of the plasma focus discharge are intense soft and hard x-ray, optical and microwave radiations. Also emitted from the focus are electrons, ions, and with certain filling gases, neutrons. The emphasis of this work is to investigate the electron and ion emission from the plasma focus and the development of appropriate diagnostics to accomplish this task. The view-point of the focus as a bipolar diode may provide a natural description of the observed phenomena. A Mather geometry plasma focus device has been constructed. Diagnostics used for electron measurements include current monitors, a calorimeter, a magnetic energy analyzer, and an emittance meter. Ion beam measurements were performed using a fluxmeter, a pinhole camera, an ion beam emittance meter, and a Thomson parabola analyzer. In addition, opening switch behavior has been investigated. Intense electron beams are observed with pulse lengths approximately 5 ns at energies of 20 to 200 keV and currents of 1 kA and above. The root-mean-square (rms) emittance of the electron beam is found to be approximately 1 cm-rad. Ion measurements show copious ion emission of very energetic ions of up to several MeV. A measurement of rms emittance of the ion beam was made. Results support the bi-polar diode model of the plasma focus device.

I would especially like to thank Dr. Moon-Jhong Rhee for his guidance and direction throughout this experimental work. Also, I would like to thank Dr. John R. Smith, Dr. Won Namkung, and Mr. Cheng-Mu Luo for their collaboration while working on these experiments.

Accession For	
NTIS GRA&I	<input checked="" type="checkbox"/>
DTIC TAB	<input type="checkbox"/>
Unannounced	<input type="checkbox"/>
Justification	
By _____	
Distribution/	
Availability Codes	
Dist	Avail and/or Special
A-1	

Approved by:



CARL W. LARSON, Head
Radiation Division



CONTENTS

<u>Chapter</u>	<u>Page</u>
1 OVERVIEW OF PLASMA FOCUS RESEARCH	1-1
INTRODUCTION	1-1
PLASMA FOCUS ACCELERATOR	1-3
THE EXPERIMENTAL DEVICE	1-7
2 OPERATION CHARACTERISTICS OF THE PLASMA FOCUS	2-1
BREAKDOWN STAGE	2-1
CURRENT SHEATH RUNDOWN STAGE	2-2
OPENING SWITCH STUDIES	2-3
3 ELECTRON BEAM MEASUREMENTS	3-1
ELECTRON BEAM CURRENT MEASUREMENTS	3-1
ELECTRON BEAM CALORIMETER	3-3
ELECTRON ENERGY MEASUREMENTS	3-7
ELECTRON BEAM EMITTANCE	3-9
4 ION BEAM STUDIES	4-1
ION BEAM FLUX MEASUREMENTS	4-1
ION PINHOLE CAMERA ANALYSIS	4-3
THOMSON SPECTROMETER ION DIAGNOSTIC	4-4
NEUTRAL PARTICLES	4-7
EMITTANCE OF ION BEAM	4-7
5 ANALYSIS OF EXPERIMENTAL RESULTS	5-1
NONREPRODUCIBILITY	5-1
ANALYSIS	5-2
COMPARISONS	5-3
CONCLUSIONS	5-5
REFERENCES	6-1
DISTRIBUTION	(1)
<u>Appendix</u>	<u>Page</u>
A MAGNETIC ELECTRON ENERGY ANALYZER RESOLUTION	A-1
B THOMSON SPECTROMETER RESOLUTION	B-1

ILLUSTRATIONS

<u>Figure</u>		<u>Page</u>
1-1	MATHER GEOMETRY PLASMA FOCUS GUN SHOWING BREAKDOWN, RUNDOWN AND FOCUS STAGES OF CURRENT SHEATH	1-10
1-2	SEQUENCE OF INSTABILITY IN THE PLASMA FOCUS	1-11
1-3	LUMPED CIRCUIT MODEL OF THE PLASMA FOCUS. AS THE PLASMA RESISTANCE INCREASES, A HIGH VOLTAGE APPEARS ACROSS THE DIODE LOAD AND THE INSULATOR	1-12
1-4	CURRENT CHARGED TRANSMISSION LINE WITH MATCHED LOAD	1-13
1-5	UNMATCHED LOAD PULSE OUTPUT	1-14
1-6	PLASMA FOCUS DEVICE	1-15
1-7	SPARK GAP SWITCH	1-16
1-8	DIAGNOSTICS RING FOR TRANSMISSION LINE CURRENT AND VOLTAGE MEASUREMENTS	1-17
1-9	DETAIL OF THE MATHER GEOMETRY GUN	1-18
1-10	INVERTED MATHER GEOMETRY GUN USED FOR ELECTRON BEAM STUDIES	1-19
2-1	OPTICAL MICROSCOPE VIEW OF INSULATOR SURFACE	2-5
2-2	SCANNING ELECTRON MICROSCOPE VIEW OF INSULATOR SURFACE	2-5
2-3	FRAMING PHOTOGRAPHS OF THE PLASMA FOCUS	2-6
2-4	ELECTRICAL SCHEMATIC OF THE PLASMA FOCUS	2-7
2-5	PLOT OF OUTPUT VOLTAGE VERSUS CURRENT DROP FOR THE PLASMA FOCUS DEVICE TO FIND THE TRANSMISSION LINE IMPEDANCE	2-8
2-6	ANALYSIS FOR DIODE LOAD RESISTANCE R_L (COMPARE WITH FIGURE 1-5)	2-9
2-7	TRANSMISSION LINE DIAGNOSTICS SIGNALS (INTEGRATED). CURRENT IS ON THE LEFT AND VOLTAGE ON THE RIGHT.	2-10
3-1	E-BEAM ROGOWSKI COIL TRACES (INTEGRATED) 1.42 kA/div	3-14
3-2	PLOT OF PEAK ELECTRON BEAM CURRENT AS A FUNCTION OF PRESSURE FOR A VARIETY OF FILLING GAS	3-16
3-3	PLOT OF BANK CURRENT AT FOCUS I_{pf} VERSUS PRESSURE FOR A VARIETY OF FILLING GAS	3-17
3-4	FARADAY CUP DIAGNOSTIC WITH CURRENT SIGNALS	3-18
3-5	WITNESS FILM FOR ELECTRON BEAM. (FIVE EXPOSURES ON A WITNESS FILM FOR E-BEAM IN 0.5 TORR Ar)	3-19

ILLUSTRATIONS (Cont.)

<u>Figure</u>		<u>Page</u>
3-6	OPEN SHUTTER PHOTO OF E-BEAM. OPEN SHUTTER PHOTOGRAPH OF BEAM PASSING THROUGH 0.32 TORR Ar. IN THE CENTER OF THE PHOTO IS A GRAPHITE BLOCK CONNECTED TO 1/2-INCH Al ROD FOR FARADAY CUP MEASUREMENTS	3-19
3-7	PLOT OF ELECTRON BEAM INDUCED PLASMA CURRENT DECAY TIME AS A FUNCTION OF GAS PRESSURE AND DISTANCE WHERE THE FARADAY CUP IS 12.5 AND 33 cm FROM THE BEAM PORT	3-20
3-8	E-BEAM CALORIMETER	3-21
3-9	CALORIMETER BRIDGE CIRCUIT. THE CHART RECORDER MEASURES V_{ab}	3-22
3-10	OUTPUT VOLTAGE OF BRIDGE AS A FUNCTION OF THERMISTOR CHANGE IN TEMPERATURE FOR THE APPLIED VOLTAGE 5.05 V	3-23
3-11	ANALYSIS OF CALORIMETER RESPONSE	3-24
3-12	PLOT OF TOTAL BEAM ENERGY AS A FUNCTION OF TOTAL INDUCTIVE ENERGY DURING FOCUS FOR CONVERSION EFFICIENCY	3-25
3-13	PLOT OF TOTAL BEAM ENERGY AS A FUNCTION OF DISTANCE DOWN THE HOLLOW CENTER ELECTRODE	3-26
3-14	MAGNETIC ELECTRON ENERGY ANALYZER	3-27
3-15	A SOLENOID ACTIVATED GATE VALVE	3-28
3-16	MICRODENSITOMETER SCAN OF PHOTOGRAPHIC FILM SHOWING THE ELECTRON ENERGY DISTRIBUTION	3-29
3-17	MICRODENSITOMETER SCAN OF PHOTOGRAPHIC FILM FOR ENERGY DISTRIBUTION OF A SERIES OF Ar SHOTS	3-30
3-18	CROSS-SECTIONAL VIEW OF THE SLIT-PINHOLE EMITTANCE METER	3-31
3-19	A TYPICAL GAUSSIAN INTENSITY PROFILE $\beta(x'_i)$ CREATED BY THE ANALYZER SLIT AT x_i . FOR $i=1$, THE MEAN DIVERGENCE ANGLE x'_i , rms WIDTH σ_i , AND HEIGHT β_i ARE SHOWN.	3-32
3-20	MICRODENSITOMETER SCAN OF RADIACHROMIC FILM FOR EMITTANCE ANALYSIS	3-33
3-21	$f_2(x, x')$ CONTOUR PLOT SHOWING 0.01, 0.1, 0.5, AND 0.9 CONTOURS	3-34
4-1	TRACK PIT ETCHING. PATHS OF ION THROUGH THE PLASTIC WILL ETCH AT A LARGER VELOCITY, v_T , THAN BULK ETCH, v_G	4-9
4-2	ION FLUX DISTRIBUTION AS A FUNCTION OF POLAR ANGLE	4-10
4-3	RESOLUTION OF THE PINHOLE CAMERA. R_c IS THE SEPARATION OF TWO OBJECTS WHICH CAN JUST BE RESOLVED ON THE DETECTOR	4-11
4-4	PINHOLE PICTURES OF 250, 250 AND 500 mTORR Ar SHOTS	4-12
4-5	STEREOSCOPIC ANALYSIS OF TWO ION SOURCES. THEIR SEPARATIONS IN X AND Z COORDINATES DEPEND ON THE SEPARATIONS S_R AND S_L	4-13
4-6	THE COMPACT THOMSON SPECTROMETER	4-14
4-7	AN EXAMPLE OF A TYPICAL Ar RESULT FROM THE SPECTROMETER	4-15
4-8	ENERGY SPECTRA FOR H IONS.	4-16
4-9	ENERGY SPECTRA FOR He IONS	4-17
4-10	ENERGY SPECTRA FOR N IONS.	4-18
4-11	ENERGY SPECTRA FOR Ne IONS	4-19
4-12	ENERGY SPECTRA FOR Ar IONS	4-20

ILLUSTRATIONS (Cont.)

<u>Figure</u>		<u>Page</u>
4-13	ION TRACK DISTRIBUTIONS FOR EMITTANCE ANALYSIS	4-21
4-14	$f_2(x,x')$ CONTOUR PLOT SHOWING 0.01, 0.1, 0.5 AND 0.9 CONTOURS	4-22
5-1	A THOMSON SPECTROGRAM WITH A CONSTANT ELECTRIC DEFLECTION SAME VALUES AS FIGURE 4-7	5-7
5-2	ANALYSIS OF FIGURE 5-1	5-8
5-3	THE ELECTRON BEAM SCALING LAW $I_{beam} \propto I_{back}^{2.9}$ PREDICTED IN REFERENCE 21 AND THE RESULT IN THIS WORK	5-9
A-1	GEOMETRY FOR MAGNETIC ELECTRON ENERGY ANALYZER RESOLUTION ANALYSIS.	A-4
A-2	RESOLUTION FUNCTION FOR THE MAGNETIC ANALYZER.	A-5
B-1	PINHOLE IMAGE GEOMETRY FOR THOMSON SPECTROMETER COLLICATOR	B-7
B-2	SEPARATION OF PARABOLAS FOR CHARGE RESOLUTION ANALYSIS	B-8
B-3	CHARGE STATE RESOLUTION OF THE THOMSON SPECTROMETER. THE LINE SEPARATES THE REGIONS WHERE CHARGE IS RESOLVED FROM REGIONS WHERE IT IS UNRESOLVED	B-9
B-4	ISOTOPE RESOLUTION HYPERBOLA	B-10
B-5	GEOMETRY FOR ENERGY RESOLUTION	B-11
B-6	CONTOURS OF CONSTANT RELATIVE ENERGY OR MOMENTUM UNCERTAINTY WHICH ARE ELLIPSES	B-12
B-7	PLOT OF RELATIVE UNCERTAINTY VERSUS ENERGY PER CHARGE FOR THE SPECTROMETER USED TO OBTAIN ION ENERGY SPECTRA . . .	B-13

TABLES

<u>Table</u>		<u>Page</u>
3-1	COMPARISON OF Ar AND N ₂ SERIES	3-9
5-1	COMPARISON OF MAJOR CHARGED PARTICLE BEAM RESULTS	5-4

CHAPTER 1

OVERVIEW OF PLASMA FOCUS RESEARCH

INTRODUCTION

The plasma focus, developed in the Soviet Union and the United States by Filippov¹ and Mather,² is basically a linear pinch in a geometry which allows rapid compression of the plasma prior to the pinch by magnetic self forces. In addition to the high plasma densities of 10^{19} per cc^{3,4,5} and temperatures of a few keV^{3,6} which may last a hundred ns, many interesting phenomena are observed. Among these are intense radiations in the microwave,^{7,8,9} optical,^{8,10} soft,^{8,11} and hard^{5,7,8,11-15} x-ray regions. Electron,^{4,5,11,12,15,17-24} ion,^{3-6,16,18-21,25-34} and neutron^{3-7,16,18,21,30-32,35} emissions have also been investigated at many laboratories.

The plasma focus originated from a simple coaxial plasma accelerator concept.³⁶ Mather investigated a higher pressure mode of operation of the device¹ while Filippov's investigation centered around new methods of breakdown across insulators for z-pinch applications.¹ When it was observed that copious neutrons were produced by this device, investigations began into possible use of this device for fusion applications; however, it was soon realized that an ion beam-target interaction explained the neutron distribution better than a thermonuclear model.^{3,18,31}

The plasma focus discharge consists of three main stages: (1) breakdown across the insulator, (2) rundown stage, and (3) collapse to focus or instability. The breakdown is initiated across the insulator in Figure 1-1 through a low pressure gas (0.1-5.0 Torr) by closing a switch connected to a high voltage capacitor. It has been observed that in some modes of operation the breakdown may occur between the inner and outer electrodes away from the insulator surface and may show some filamentary structure.³⁷⁻³⁹ This regime,

which may depend on filling pressure and insulator geometry, is associated with poor focus formation and should be avoided. It has been suggested by Krompholz, et al.,³⁹ that a circular knife edge placed at the junction of the outer electrode and the base of the insulator may serve to enhance the E-field and lead to uniform breakdown which will improve the final focus formation reproducibility.

The rundown stage occurs as the current sheath lifts off the insulator surface and is driven down the center electrode length by $J_r B_\theta$ forces. In the snowplow model, as the current sheath advances through the gun region, all the gas in the gun region is pushed out leaving vacuum behind. The current sheath travels at an approximately constant velocity of a few cm/ μ sec which is determined by momentum balance between the filling gas and the magnetic pressure behind the current sheath. In cylindrical coordinates, the parabolic shape of the current sheath is given by the function³⁹:

$$z(r) = -\frac{a}{2i} \left[k(k^2 - i^2)^{1/2} - (1-i^2)^{1/2} - i^2 \ln \frac{k+(k^2 - i^2)^{1/2}}{1+(1-i^2)^{1/2}} \right], \quad (1-1)$$

where a is the center electrode radius, k is r/a , and i is an experimentally determined parameter given by the momentum balance condition:

$$i = \left(\frac{\mu_0 I^2}{8n\pi^2 a^2 v^2} \right)^{1/2}, \quad (1-2)$$

where I is the current flowing through the sheath, n is the density of gas and v is the velocity of the sheath. The quantity i approximately equals unity.

The $m=0$ instability, which has the highest growth rate,⁴⁰ occurs after the current column carrying 100 kA to 1 MA collapses toward the axis due to $J_z B_\theta$ forces. It is during this instability stage that most physically interesting phenomena occur. From the hot ($T_e=1$ keV), dense ($n=10^{19}$ cm⁻³) plasma, intense optical, soft x-ray and microwave radiations are observed. In addition,

electrons and ions are accelerated in the focus to energies of a few hundred keV per charge which have been attributed to the $m=0$ instability by some models.⁴¹⁻⁴⁵ Byproducts of these are hard x-rays from brehmstrahlung as the electrons strike the copper electrodes; also, (if the filling gas is deuterium) 10^8 - 10^9 neutrons per shot are produced by ion beam-target spallation reactions. Semi-empirical models of the $m=0$ instability in the plasma focus by R. Deutsch⁴⁵ and Hohl and Gary⁴² indicate that a voltage on the order of 100 kV may be induced in the focus by the $m=0$ instability. These models assume some typical $m=0$ constriction velocities observed with streak camera photography or current reduction.

It has been observed with laser scattering experiments⁴⁶ that subsequent to the onset of the $m=0$ instability, there is a rapid increase in the electronic temperature accompanied by a period of resistive magnetic field diffusion through the plasma to the axis. It has been speculated that lower hybrid, or electron cyclotron drift instabilities may be responsible for some of the heating^{43,47} and subsequently, ion acoustic instability may dramatically increase the resistivity of the plasma. In fact, recently microwave emission has been observed in the plasma focus which may be attributed to the lower hybrid drift instability.⁴⁸ Figure 1-2 shows a temporal progression of these phenomena.

Particle energies of up to several MeV have been observed but the yields at these energies are typically a few orders of magnitude below those in the 100 keV range. The physical mechanism of the intense particle beam generation in a plasma focus device is unclear up to the present time. The goal of this work is to investigate the physical nature of the plasma focus electron and ion beams in hopes that an understanding of this diode-like behavior will lead to an improved physical understanding of the plasma focus device as an excellent source of electron and ion beams in the regime considered. This requires that the source of the most intense beams be investigated.

PLASMA FOCUS ACCELERATOR

A plasma focus device may be described by a simple lumped circuit model as in Eltgroth⁴⁹ and Mather.⁵⁰ In Figure 1-3, C_{ext} is the external capacitance which

consists mostly of the capacitance of the main capacitor bank. Stray capacitance is negligibly small. L_{ext} is the external circuit inductance which arises from the bank inductance and all other circuit inductances exclusive of the gun region-plasma sheath inductance. R_{ext} is the external circuit resistance excluding the gun region-plasma sheath resistance. L_p is the gun-plasma sheath inductance which is a variable quantity, changing with the geometry of the current sheath. R_p is the gun-plasma sheath resistance. Finally, R_L is either the diode load resistance or the leakage resistance across the insulator which is in parallel with R_p . At time $t=0$ the switch is closed and the current begins to flow through the circuit. Subsequent to the current sheath breakdown across the insulator in the gun region, R_p is on the order of milliohms (Spitzer resistivity) as pointed out by Mather. R_{ext} , which may be due to the spark gap switch, might be much higher. L_p is calculable and found to be less than or the same order of magnitude as L_{ext} , depending on the position and shape of the current sheath. N_{ext} is a dominant element by the nature of the device. The net effect of these circuit elements is to produce a ringing circuit which is underdamped by the total resistance which may mostly appear in the spark gap and the plasma current sheath. The instability occurs as the sheath collapses toward the axis at which time the plasma resistivity rapidly rises and the current flowing through the circuit begins to drop. A significant induced voltage appears across the diode load R_L at this time. It may be shown that in the focus stage $L \frac{dI}{dt}$ is much larger than $I \frac{dL}{dt}$. In fact, it is important to note that the signs of these two terms are opposite each other¹² during the plasma pinch stage. $I \frac{dL}{dt}$ opposes the flow of current⁴⁹ and $L \frac{dI}{dt}$ favors production of the beam. Another important point to be considered is the leakage current across the insulator. The induced voltage that appears at the time of the focus will also appear across the insulator. If the current sheath has not swept out all of the gas between the electrodes, there may be a possibility of a subsequent breakdown across the insulator which will immediately short circuit the diode load.

If the $m=0$ instability completely interrupts the current flow at the time of the instability the voltage approaches infinitely large in this model. The circuit model requires some further input to describe the form of the plasma resistance as a function of time in order to predict the diode voltage and current. Unfortunately, the theory of the plasma focus instability is not

sufficient at the present time to accomplish this task. This is the motivation for the development of a transmission line theory of the plasma focus.

A transmission line theory of the plasma focus was developed in an attempt to explain the presence of a finite voltage pulse.⁵¹ In essence, a transmission line theory accounts for the presence of an electromagnetic field and the dissipation of its energy in a resistive load. The simplest possible model for the plasma focus is found in Figure 1-4. Immediately after the formation of the current sheath, the plasma focus is modeled as a current charged transmission line shown in Figure 1-4 with the switch at 1 closed. This assumes that the resistance of the current sheath and sparkgap are negligible, and all characteristic impedances of each section of the plasma focus device are matched to Z_0 . At this stage, the current charged transmission line can be thought of as two oppositely traveling waves of current:

$$I = I_+(t - \frac{z}{v}) + I_-(t + \frac{z}{v}) , \quad (1-3)$$

where the magnitude of I_+ and I_- is $I_0/2$ (half the total charging current), and v is the velocity of transverse electromagnetic (TEM) wave propagation in the transmission line. The voltage waves are of the form:

$$V = I_+/Z_0 - I_-/Z_0 , \quad (1-4)$$

where $Z_0 = \sqrt{(L_u/C_u)}$, L_u is the inductance per unit length, and C_u is the capacitance per unit length. At time $t=0$, the switch is opened. The reflection and transmission coefficients determined by boundary conditions in this simple model are:

$$\rho_v = \frac{(R_L - Z_0)}{(R_L + Z_0)} , \text{ and} \quad (1-5)$$

$$\tau_v = \frac{2R_L}{(R_L + Z_0)} , \quad (1-6)$$

(satisfying the boundary conditions $1 + \rho_v = \tau_v$ and conservation of energy $\rho_v^2 + \tau_v^2 = 1$); hence, if the load resistance R_L is matched to the impedance of the

transmission line, ρ_v equals 0 and τ_v equals 1. Subsequently, the right traveling current wave in Figure 1-4 is dissipated in the load resistance. The output pulse is of duration $2l/v$, voltage $I_0 Z_0/2$, and current $I_0/2$. It is important to emphasize that these parameters arise from an ideal opening switch and perfect impedance matching. These depend upon the detailed physics of the focus instability which are not well understood.

As a simple non-ideal case, we may suppose that the load resistance is not precisely matched to that of the transmission line. In this case, the reflection and transmission coefficients are no longer 0 and 1, respectively. The two distinctly different regimes are $R_L > Z_0$ and $R_L < Z_0$. If R_L is greater than Z_0 , then ρ_v is greater than 0 and τ_v is greater than 1. It can easily be seen that the output voltage will consist of multiple pulses of changing polarity, the i^{th} pulse having amplitude $I_0 Z_0 (-\rho_v)^{i-1} (1+\rho_v)/2$ and duration $2l/v$ as depicted in Figure 1-5. On the other hand, if $R_L < Z_0$, ρ is less than 0 and the output will all be of one polarity. See Figure 1-5. The distribution of this current output between electron and ion currents will depend upon the diode characteristics. We will describe the bi-polar diode in the following section.

The acceleration of ions and electrons across a diode has been investigated quite extensively. The simple relativistic diode model for the plasma focus maybe a one-dimensional, bi-polar, Child-Langmuir diode. In this model, two semi-infinite slabs of plasma are separated by a fixed distance with a fixed voltage supplied between them. The resultant current flow is space charge limited. The ratio of ion current to electron current is given by:⁵²

$$\frac{I_{\text{ion}}}{I_e} = \left[\frac{m_e}{M_i} \frac{(\gamma + 1)}{2} \right]^{1/2}, \quad (1-7)$$

where m_e and M_i are the electron and ion rest mass, $(\gamma + 1) m_e c^2/e$ is the voltage across the diode, c is the velocity of light in vacuum, and e is the electronic charge.

A correction including two-dimensional effects has been proposed by Goldstein and Lee⁵³ and applied to the plasma focus by Gullickson.⁵⁴ In the so-called pinch-reflex diode, pinching of the electron beam across the gap enhances ion

current somewhat, but electron current still dominates the net current flow across the diode for most geometries. The ratio of ion current to electron current is the same as above multiplied by the factor $(r_d^2 + d_d^2)^{1/2}/d_d$ where r_d is the radius of the cylindrical diode (plasma) and d_d is the gap spacing. This factor arises from the geometry. Due to the pinching of the electron flow, it has an effectively longer gap to traverse than the ions. Unfortunately, it is quite difficult to determine the interrelationships between r_d , d_d , γ , and currents in the real plasma focus diode in which these quantities are not fixed. It is hoped that these experimentally observed quantities will help in the eventual physical understanding of the plasma focus diode in order that the very attractive features found in this compact accelerator may find many applications.

THE EXPERIMENTAL DEVICE

A prototype plasma focus accelerator has been constructed in order to investigate the diode-like behavior of the instability. The major systems of this accelerator are: (1) a capacitor bank and charging system, (2) a triggering system, (3) a transmission line section, (4) a diagnostics section, and (5) a Mather geometry plasma gun. See Figure 1-6.

The capacitor bank used is either a single 3 kJ, 20 kV low inductance (40 nH) capacitor or a set of four connected in parallel. This bank is charged through a 500 Kilo Ohm resistor by a Universal Voltronics model bal 22-35 power supply. The device is triggered by a spark gap switch with a midplane trigger electrode shown in cross section in Figure 1-7. Typically the gap utilizes nitrogen gas at or slightly above atmospheric pressure. The breakdown field is given by:

$$E_{br} \text{ (kV/cm)} = [24.6p + 6.7(p/d_{eff})^{1/2}] F^{-1} \quad (1-8)$$

where p is the pressure in atmospheres, d_{eff} is the effective electrode gap separation and F is the field enhancement factor, i.e., the ratio of the maximum to the mean field on the electrodes. For our spherical electrodes, d_{eff} is $0.115d$, where d is the actual gap spacing, and the field enhancement factor F is

1.8.⁵⁵ The gap spacing used varied somewhat, however remained near 1 cm for most experiments. An estimate of switch inductance given by Miller gives 14 nH/cm hence our switch adds about 14 nH to the total inductance. A Thyratron tube circuit is used to provide the high voltage (18-24 kV) pulse to the trigger electrode to initiate gap breakdown.

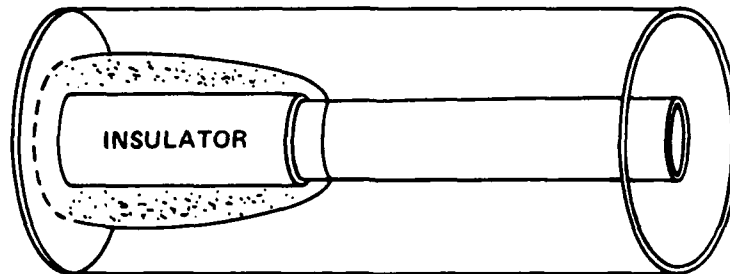
The transmission line section consists of a 30 cm long coaxial line with an inner conductor diameter of 5.1 cm and an outer conductor diameter of 14.6 cm. The total inductance is 64 nH for this section. The characteristic impedance (Z_0) is $\frac{60}{\sqrt{\epsilon}}$ ohms for this geometry, where ϵ is the dielectric constant of the medium between the conductors. For a water dielectric, this gives $Z_0 = 7$ ohms, while for air, 60 ohms. Water is used exclusively in this work due to its conductive properties assisting in holding off a corona discharge across the insulator before firing, therefore the matched output pulse would be 18 nsec in duration and the output voltage would be one half the charging current times 7 ohms.

A 2.5 cm long diagnostics section is inserted between the transmission line and the coaxial gun. See Figure 1-8. A Rogowski coil⁵⁶⁻⁵⁹ is made from 30 windings on a ring with a 9 mm² cross section and a mean radius of 7.65 cm. The coil signal is integrated with a 50 μ s (= measured R,C) passive integrating circuit. The calibration is calculated to be 68.55 kA/V. A capacitive voltage divider probe (D-dot) is constructed by placing a 1 cm radius disc 1 cm from the inner surface of the diagnostics ring. The signal from the probe is integrated by a passive 2.63 μ s integrator. The calibration is calculated to be 19.2 kV/V with water dielectric in the transmission line. The B-dot probe was not used in any experiments discussed in this work.

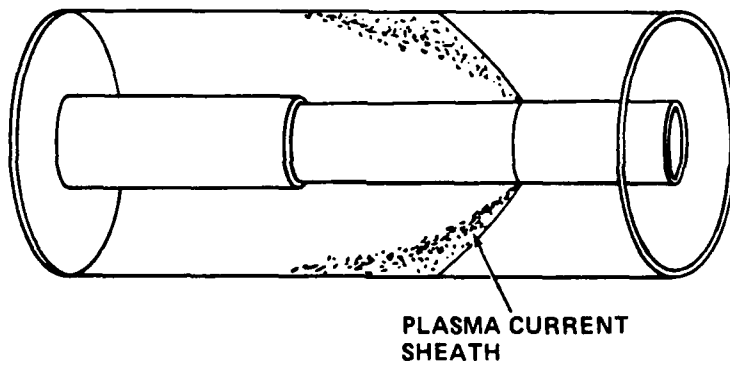
The usual Mather geometry plasma gun is shown in Figure 1-9. It consists of a 7.5 cm inner diameter copper outer electrode (cathode) and a 2.5 cm diameter inner electrode (anode). For most experiments, a squirrel cage outer electrode is used which is made from 12, 0.125-inch copper rods spaced equally on a 7.5 cm diameter. A pyrex glass insulator separates the inner electrode from the brass backplate which is electrically the cathode. The insulator is fixed in place on the plexiglass with silicone sealant. The 2.6 cm long insulator surface is made

flush with the cylindrical surface of the inner electrode with a small gap between them (1 mm) to prevent mechanical shock on the inner electrode from shattering the glass. This geometry is utilized for ion beam measurements since the ions are accelerated away from the anode. In order to investigate the electron beam which is accelerated down the middle of the hollow center electrode, we must invert the usual gun geometry as shown in Figure 1-10. In this experimental arrangement, the capacitor bank is charged negatively so that the center conductor on the transmission line becomes the plasma focus gun cathode.

1) BREAKDOWN



2) RUNDOWN



3) FOCUS

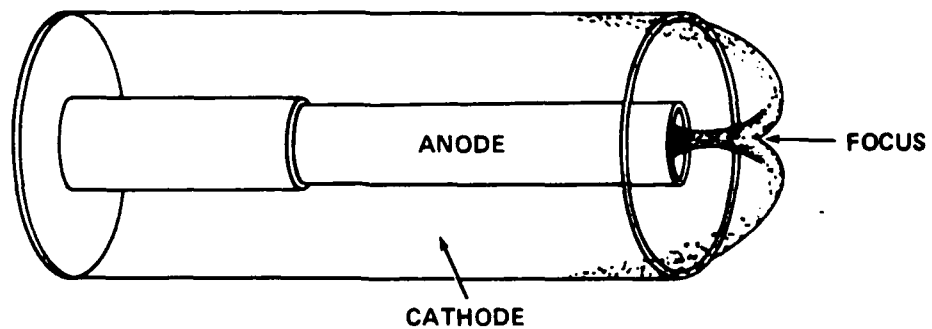


FIGURE 1-1. MATHER GEOMETRY PLASMA FOCUS GUN SHOWING BREAKDOWN, RUNDOWN AND FOCUS STAGES OF CURRENT SHEATH

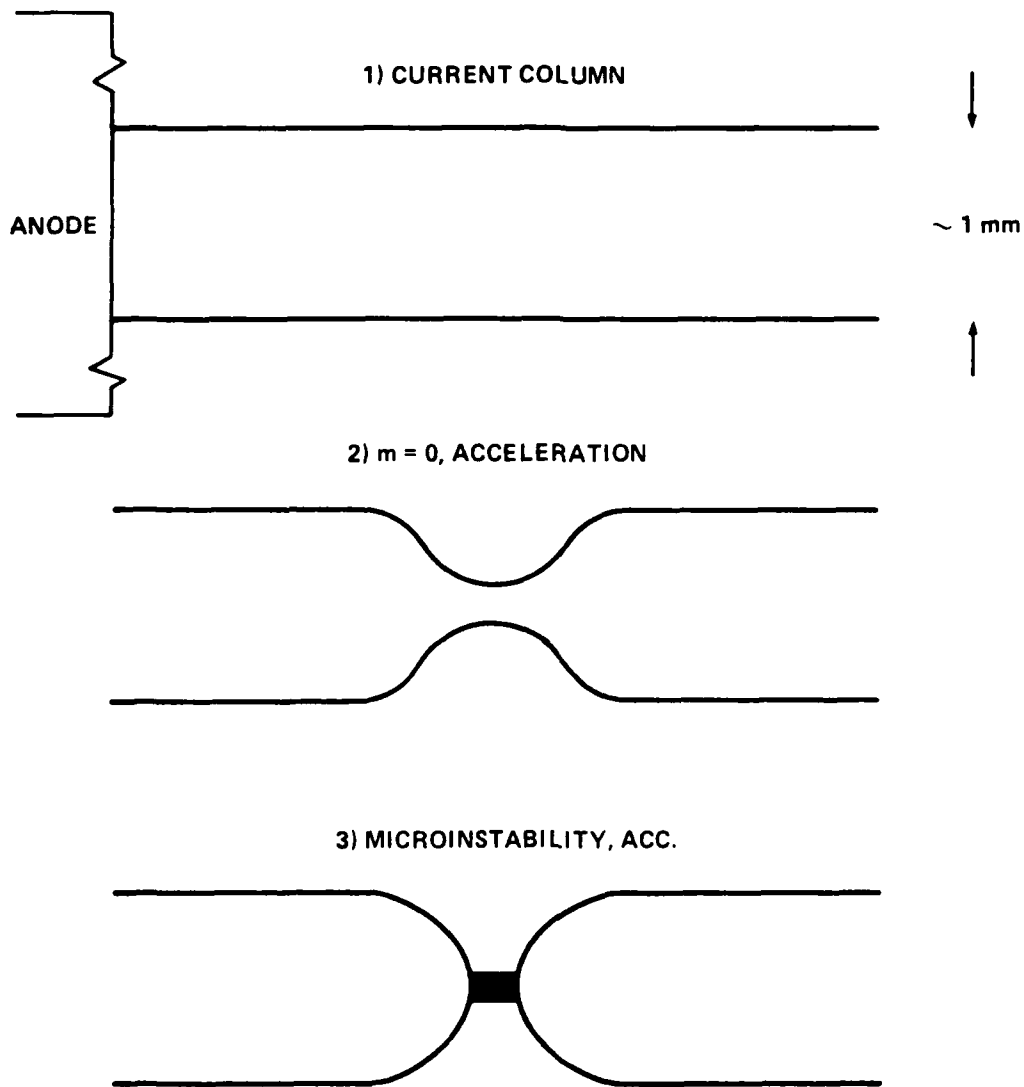


FIGURE 1-2. SEQUENCE OF INSTABILITY IN THE PLASMA FOCUS

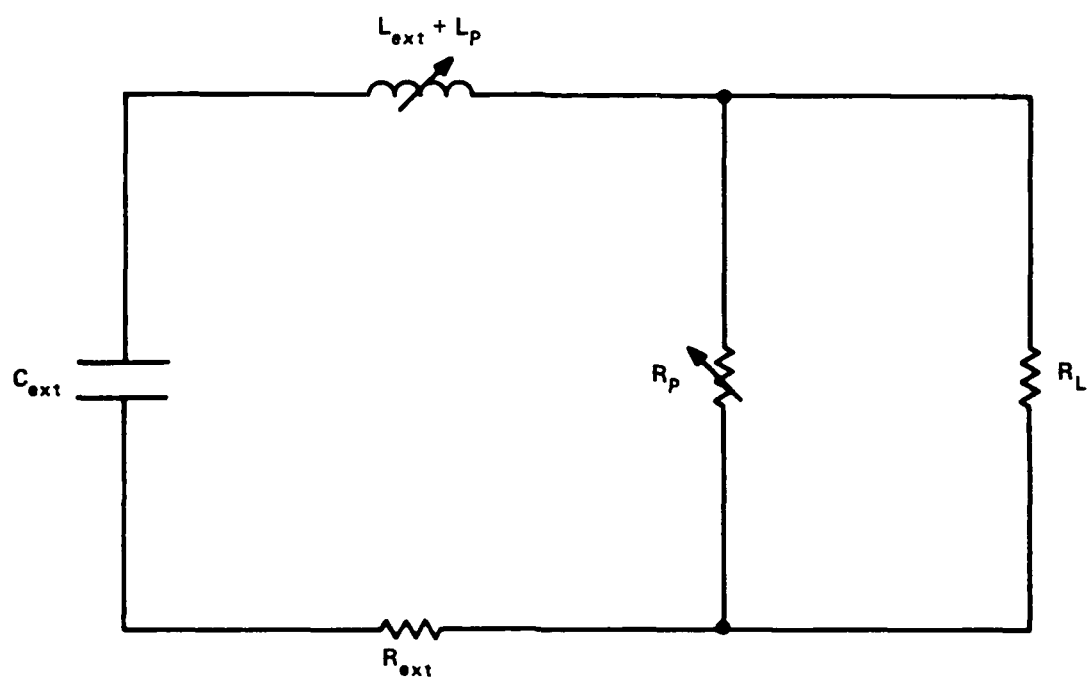


FIGURE 1-3. LUMPED CIRCUIT MODEL OF THE PLASMA FOCUS. AS THE PLASMA RESISTANCE INCREASES, A HIGH VOLTAGE APPEARS ACROSS THE DIODE LOAD AND THE INSULATOR.

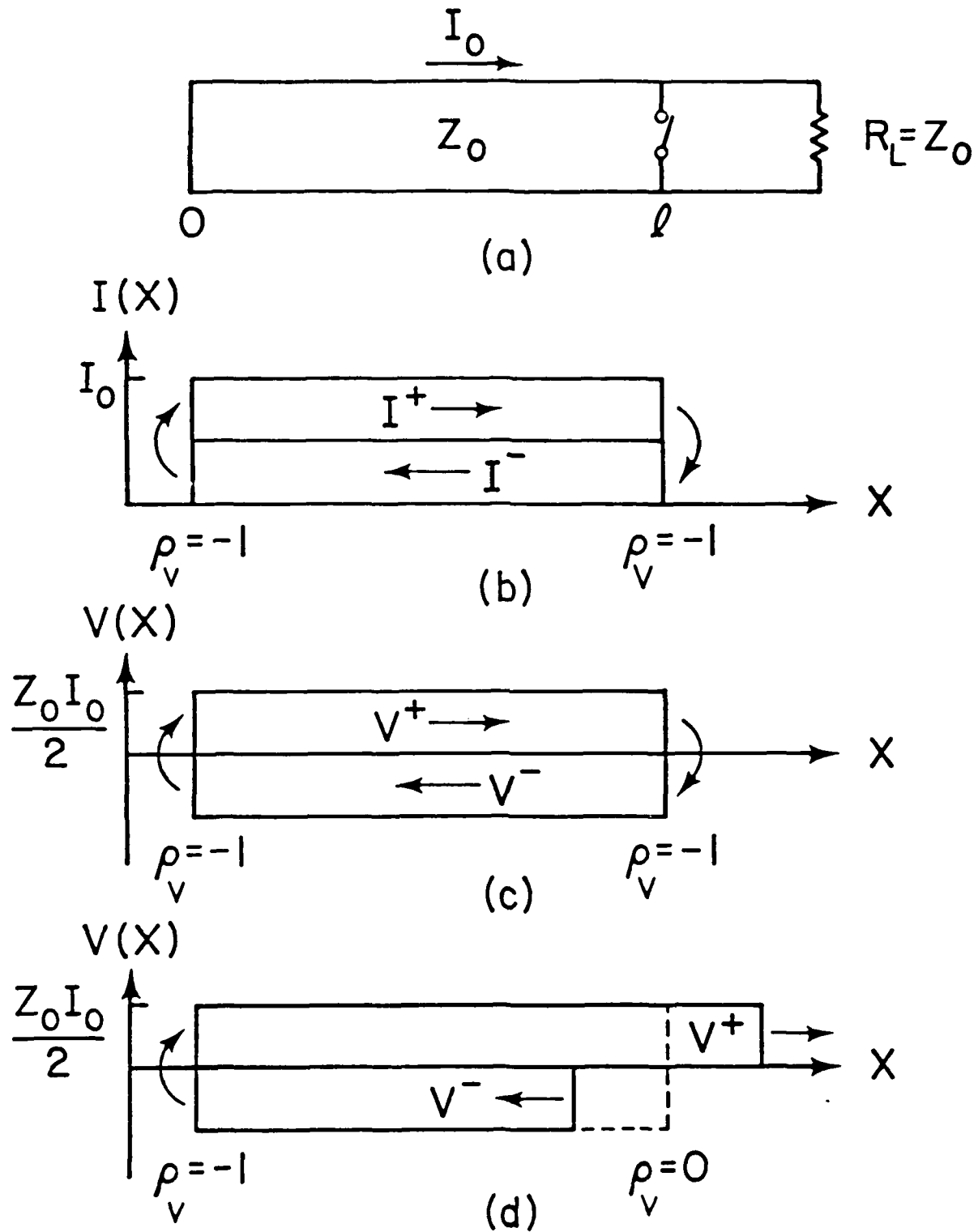
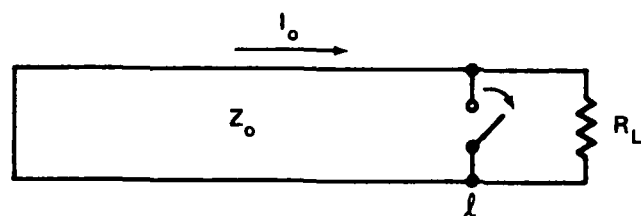
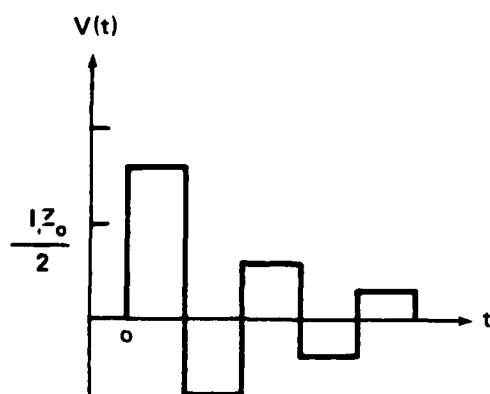


FIGURE 1-4. CURRENT CHARGED TRANSMISSION LINE WITH MATCHED LOAD



a) $R_L > Z_o$



b) $R_L < Z_o$

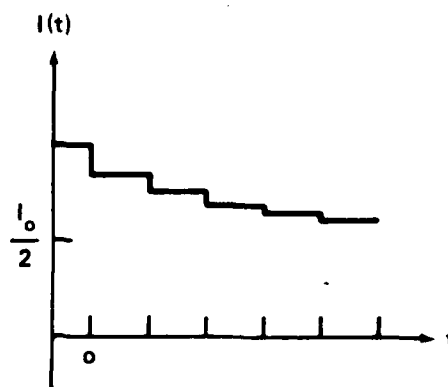
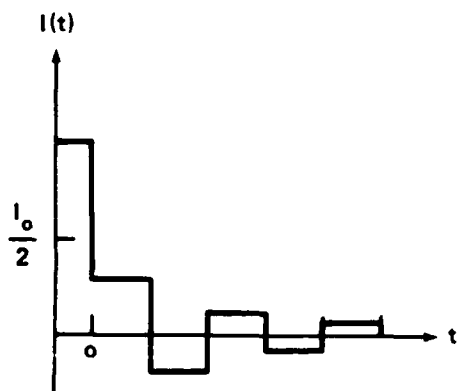
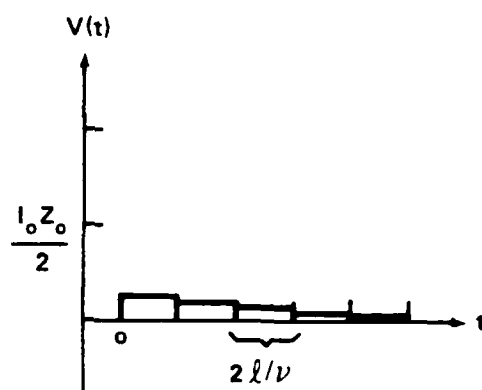


FIGURE 1-5. UNMATCHED LOAD PULSE OUTPUT

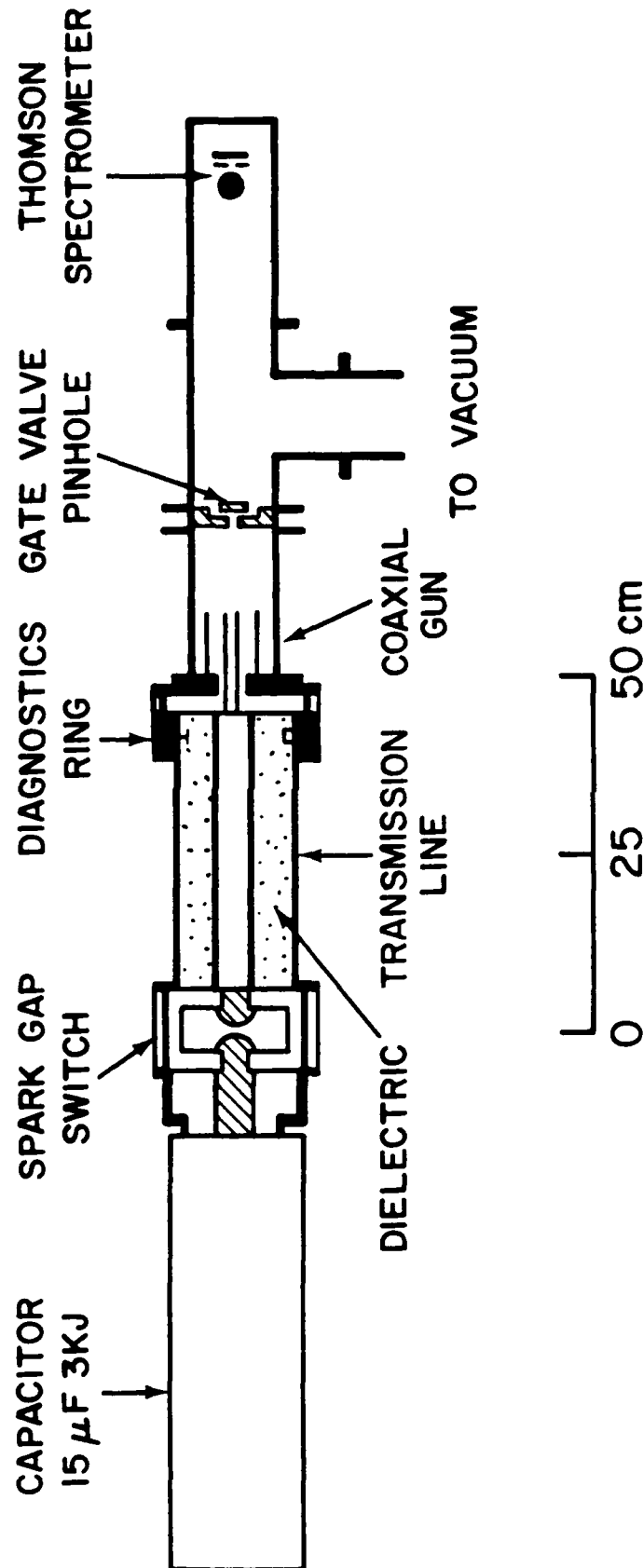


FIGURE 1-6. PLASMA FOCUS DEVICE

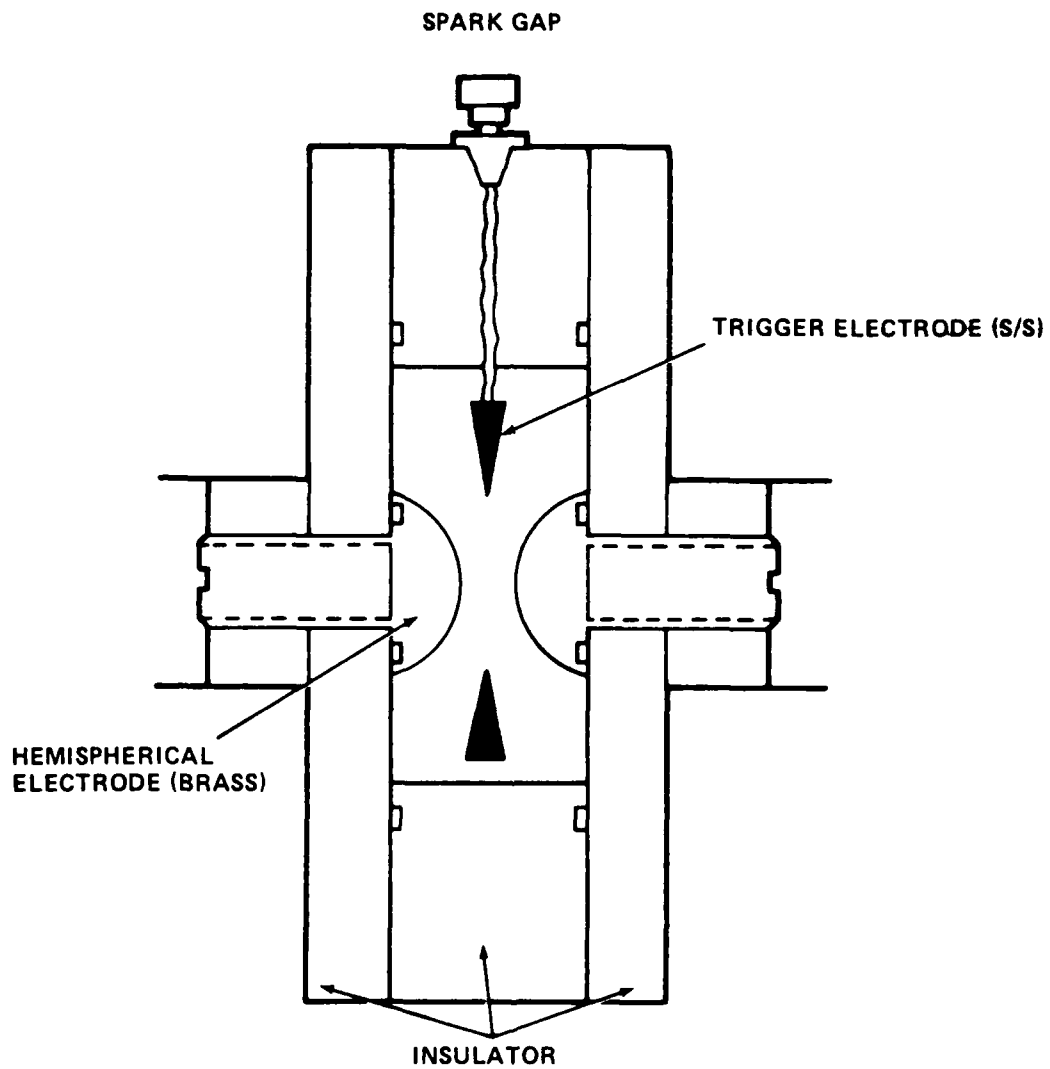


FIGURE 1-7. SPARK GAP SWITCH

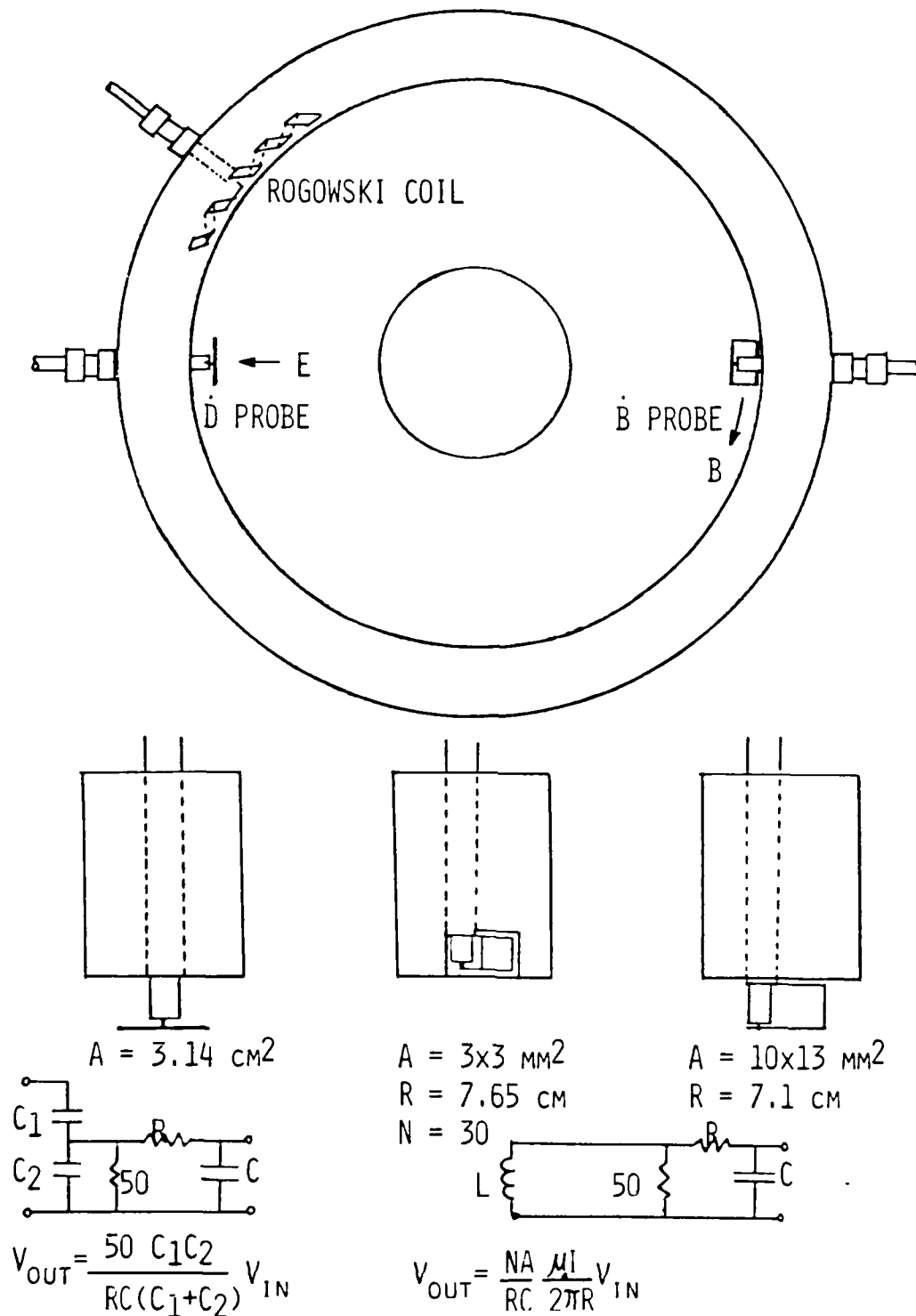
DIAGNOSTICS RING

FIGURE 1-8. DIAGNOSTICS RING FOR TRANSMISSION LINE CURRENT AND VOLTAGE MEASUREMENTS

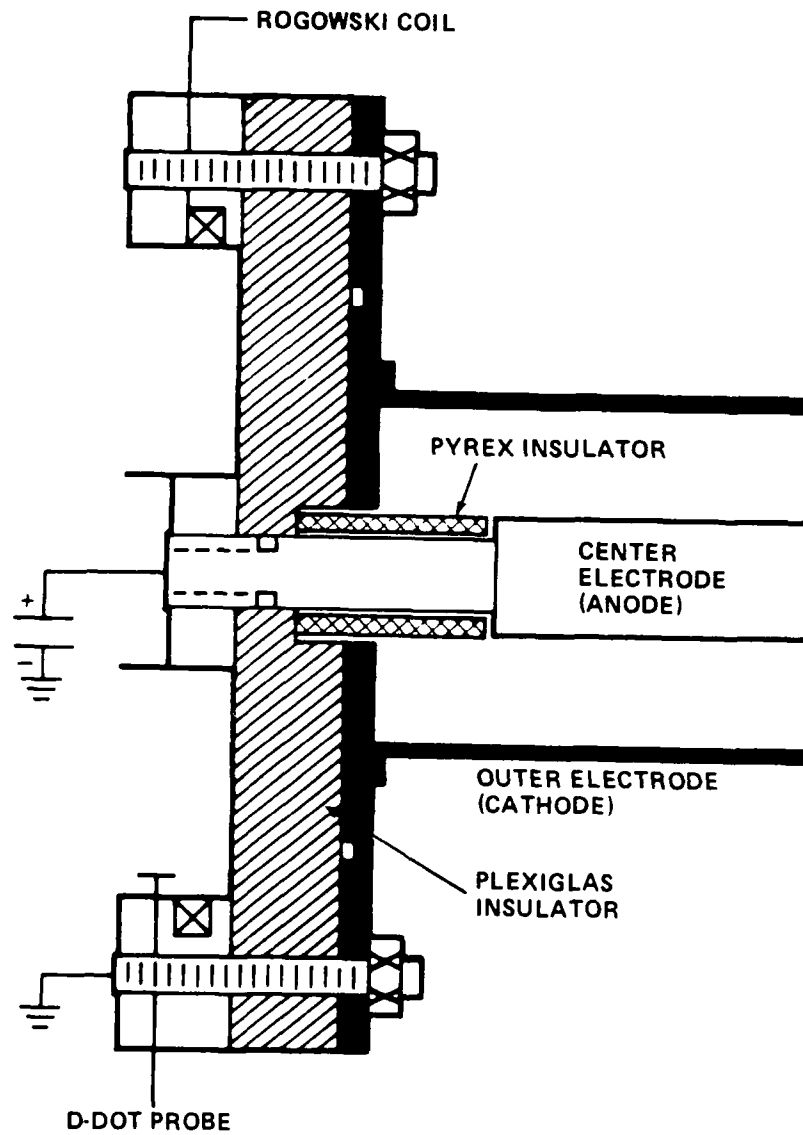


FIGURE 1-9. DETAIL OF THE MATHER GEOMETRY GUN

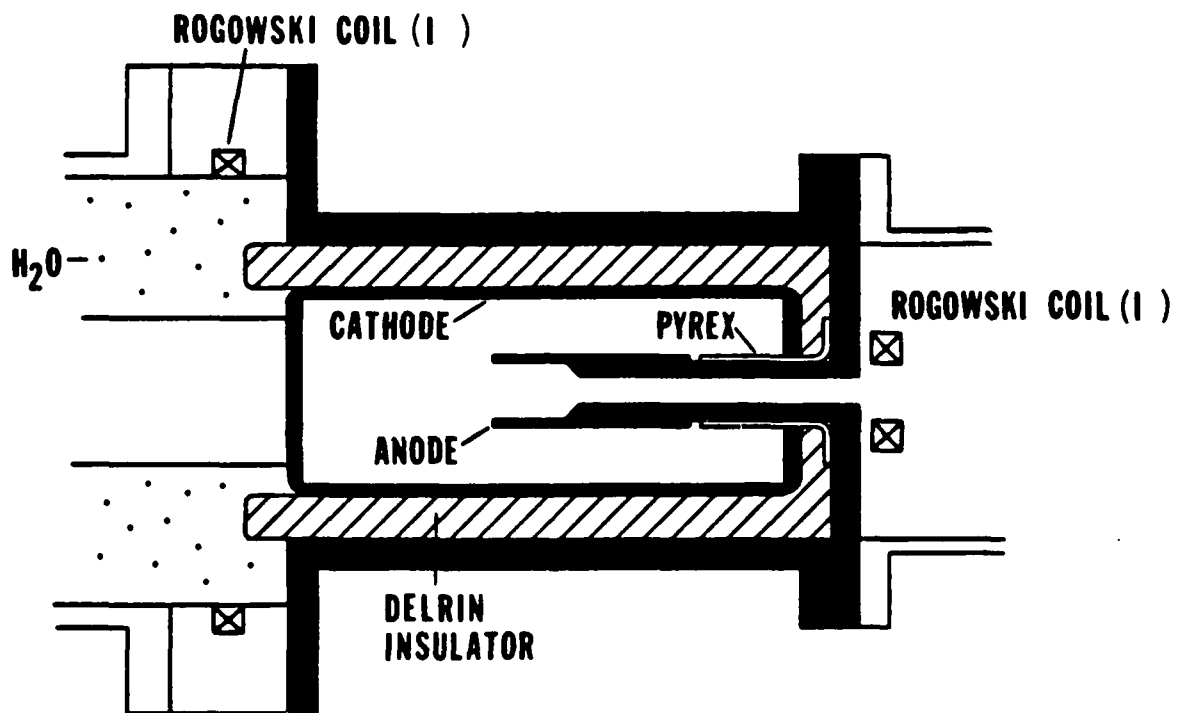


FIGURE 1-10. INVERTED MATHER GEOMETRY GUN USED FOR ELECTRON BEAM STUDIES

CHAPTER 2

OPERATION CHARACTERISTICS OF THE PLASMA FOCUS

BREAKDOWN STAGE

A symmetric and uniform initial breakdown across the pyrex insulator in the plasma gun may be quite important to the formation of a symmetric and reproducible focus. The breakdown occurs as a high voltage appears between the anode and cathode subsequent to the triggering of the spark gap switch. The conditioning process of the insulator has been evident in many experiments. Typically, a new plasma focus device insulator requires anywhere from 0 to 60 shots before a reproducible current drop in the main transmission line Rogowski coil, or a corresponding voltage spike, is evident. This process of conditioning has been observed in vacuum spark gaps;⁶⁰ however, we wish to include the plasma focus device as one undergoing the similar type of conditioning process. In the plasma focus device, high currents well above 100 kA are passed between the electrodes through a very low pressure (sub Torr) gas. During this time, heating and sputtering of the electrode surfaces would result in the formation of a metallic vapor in the gun region which would preferentially redeposit on the electrodes due to their cooler temperatures (since their thermal conductivity is higher than that of the pyrex insulator). However, eventually some electrode material would be deposited on the pyrex insulator, and subsequent shots would then preferentially deposit on the regions which already have some metallic deposit. This process would lead to a clumping of the metallic deposits (or perhaps crystal growth) in these regions.

It was observed that our pyrex insulator became coated with a non-conducting metallic copper layer in our electron beam geometry gun which has all copper electrodes. This gun worked very reproducibly for several hundred shots before the insulator broke due to mechanical shock. When a chip of this insulator was

placed under an optical microscope, it was noticed that the surface showed crazing, in addition to the coating of copper. A picture of the insulator taken through an optical microscope is shown in Figure 2-1.

Regions of approximately $0.1 \times 0.1 \text{ mm}^2$ were evidently separated by the small surface cracks which may have served to maintain the overall non-conductive property of the insulator surface. Under the scanning electron microscope, further detail of the coating is evident in Figure 2-2, indicating that there are many micron-size clumps of metal which seem to be preferentially deposited along the surface cracks.

It is hypothesized that these regions of metallic coating may serve to grade the insulator naturally, providing a uniform and symmetric breakdown along the surface which leads to a symmetric and reproducible focus formation.

CURRENT SHEATH RUNDOWN STAGE

The sheath rundown stage is investigated with the use of a framing camera which has an exposure time of 10 nsec and a frame separation of 50 nsec. As pointed out previously, the velocity of the current sheath is mainly determined by momentum balance:

$$v = \left(\frac{\mu_0 I^2}{8n\pi^2 a^2} \right)^{1/2} = 4.2 \text{ cm}/\mu\text{s}, \quad (2-1)$$

where the values $I = 205 \text{ kA}$, $n = 2.35 \times 10^{-3} \text{ kg/m}^{-3}$, and $a = 1.27 \text{ cm}$ have been used for the 1 Torr argon (Ar) shot which we shall analyze. The average velocity of the sheath is determined during three different regimes in the shot from photographs similar to those shown in Figure 2-4. The three regimes are: (1) radial expansion outward from the insulator ($1.5\text{-}2.5 \mu\text{s}$), (2) motion down the coaxial electrodes ($2.5\text{-}3.4 \mu\text{s}$), and (3) radial collapse at the tip of the center electrode ($2.9\text{-}3.5 \mu\text{s}$). In regimes (1) and (3), the image converter camera is placed on axis of the system so that only the radial component of the velocity is measured as in Figure 2-3(A). For regime (2), the camera is placed so that a side-on view of the sheath is obtained as in Figure 2-3(B). The average velocity of the radial expansion from 1.5 to $2.5 \mu\text{s}$ is found to be

1.5 (+/- 0.2) cm/ μ s (the velocity along the center conductor), and it is found to average 1.4 (+/-0.2) cm/ μ s from 2.5 to 3.4 μ s. Finally, the radial collapse is found to average 2.6 (+/- 0.2) cm/ μ s during the time from 2.9 to 3.5 μ s. The error limits are approximately determined from the re-resolution of the framing photographs. The value found for case (2) shows approximate agreement with the simple existing theory which gives 4.2 cm/ μ s.

OPENING SWITCH STUDIES

The plasma focus device may be viewed as an opening switch connected to a load (i.e., plasma diode).⁶¹ Characteristics of the opening switch may be investigated with the transmission line Rogowski and voltage probes. A schematic of the plasma focus is found in Figure 2-4. The device is represented by a current charged transmission line with impedance Z_0 . Initially, the m=0 switch is closed, and the transmission line will charge to a current peak through LC ringing determined by the lumped circuit inductance and capacitance of the transmission line and capacitor. When the current flowing through the plasma (closed m=0 switch) reaches its peak (I_0), the m=0 instability opens the switch forcing the dissipation of the stored electromagnetic field energy through the load R_L (plasma diode) resulting in the acceleration of ions and electrons in the plus and minus z directions.

The characteristic impedance of the transmission line is found from the output voltage and current drop (see Figure 2-5). The slope of the graph from aleast squares fit is 6.88 ohms. For comparison the calculated value of impedance $\sqrt{(L_u/C_u)}$ is 7 ohms.

The diode load resistance may be found from the output current and voltage. For example, the shot in Figure 2-6 shows an output voltage of 150 kV with an output current of 157 kA giving $R_L = 0.96$ ohms. Figure 2-6 also shows the theoretical current and voltage waveforms assuming an ideal transmission line behavior with these values. The difference indicates a non-ideal behavior which may be attributed to the non-ideal opening switch action of the plasma focus. Indeed the voltage waveforms in Figure 2-7 indicate a wide shot-to-shot

variation, sometimes showing multiple peaks as well as single voltage peaks, not in agreement with the simple transmission line theory except that the pulse width is of the same order of magnitude. In a typical series of 21 shots of He-Armixture, about 38 percent of the shots showed single spikes, 43 percent showed double spikes, and 19 percent showed more than two peaks. The average FWHM of a single spike is 21 ns with a 5 ns standard deviation. The average peak to peak separation of double spikes is 17 ns with a standard deviation of 6 ns. This erratic behavior is one of the most important contributing factors in making the exact acceleration mechanism difficult to determine.

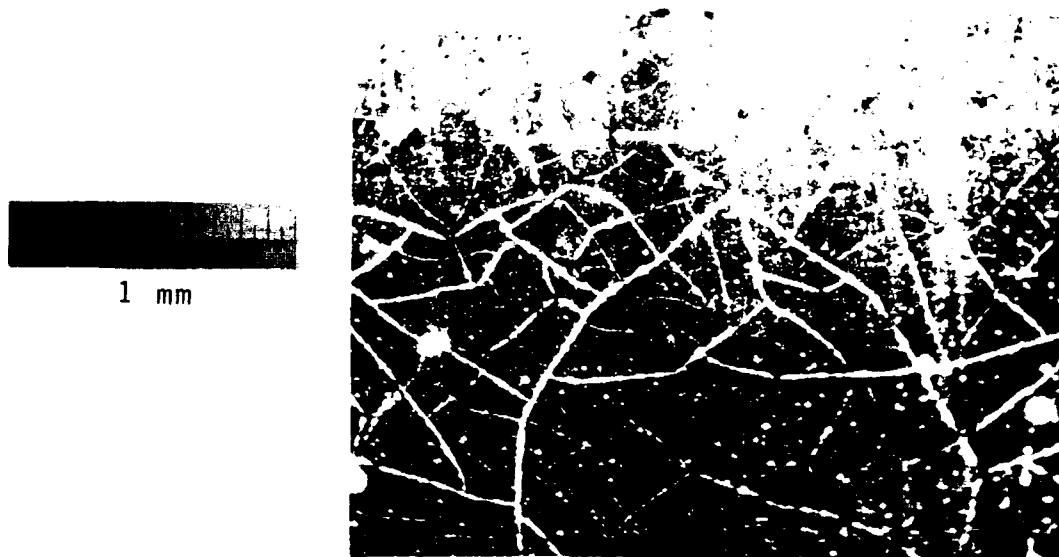


FIGURE 2-1. OPTICAL MICROSCOPE VIEW OF INSULATOR SURFACE

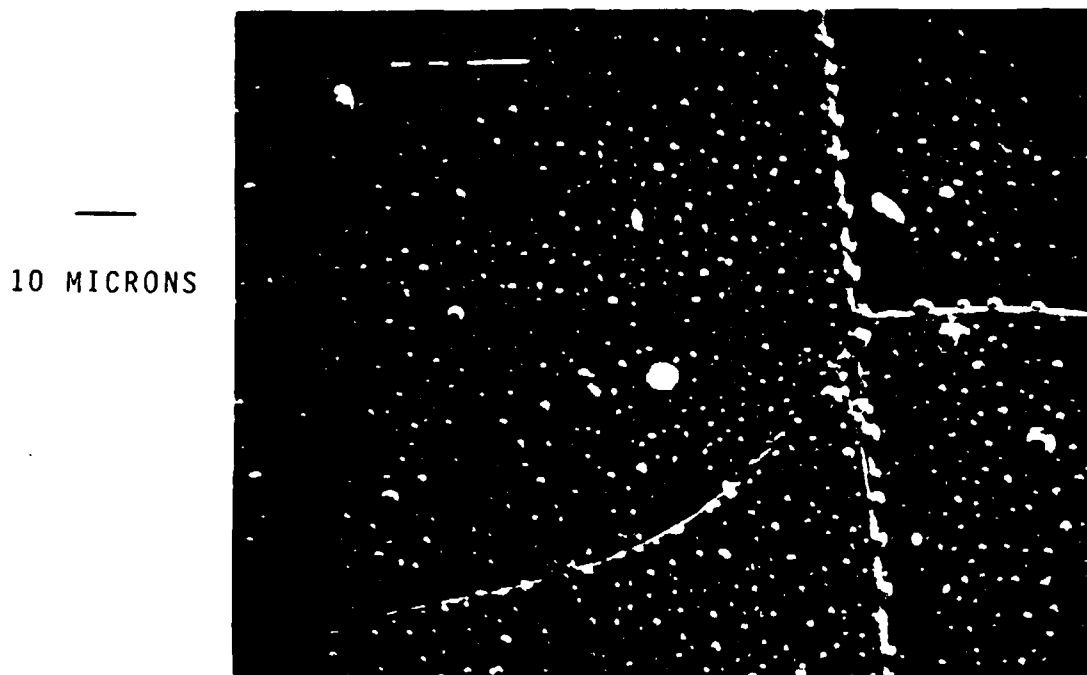
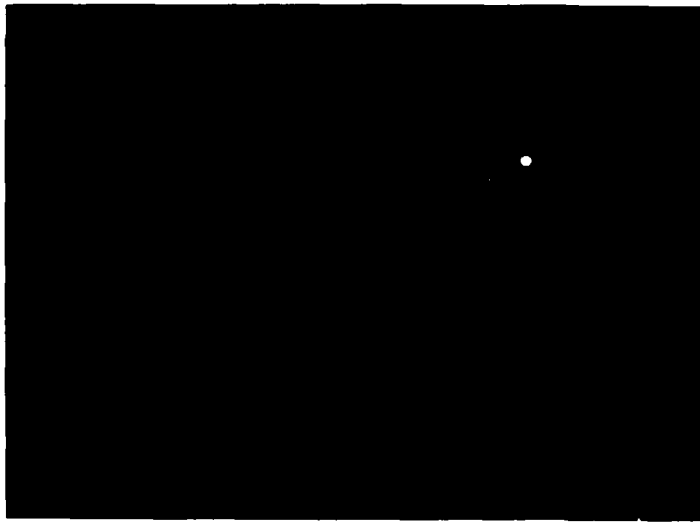
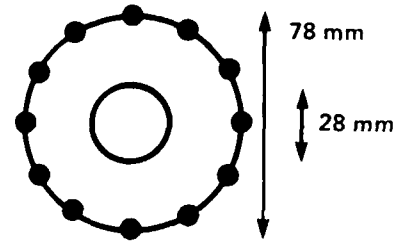


FIGURE 2-2. SCANNING ELECTRON MICROSCOPE VIEW OF INSULATOR SURFACE



(A) TAKEN ALONG THE Z-AXIS

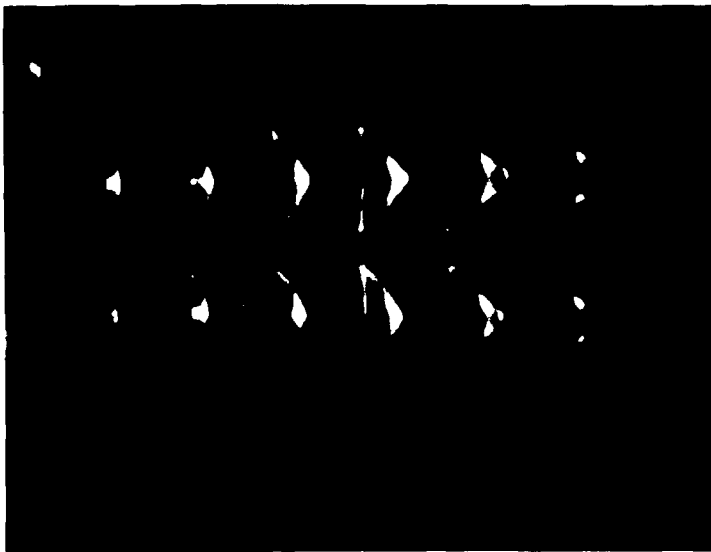
Ar 1.0 TORR. DELAY TIME 3.0 μ s



SEQUENCE

2 4 6 8 10 12

1 3 5 7 9 11



(B) SIDE-ON VIEW

He 1.0 TORR. DELAY TIME 2.8 μ s

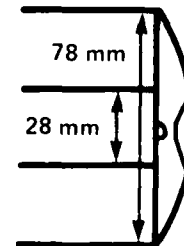


FIGURE 2-3. FRAMING PHOTOGRAPHS OF THE PLASMA FOCUS

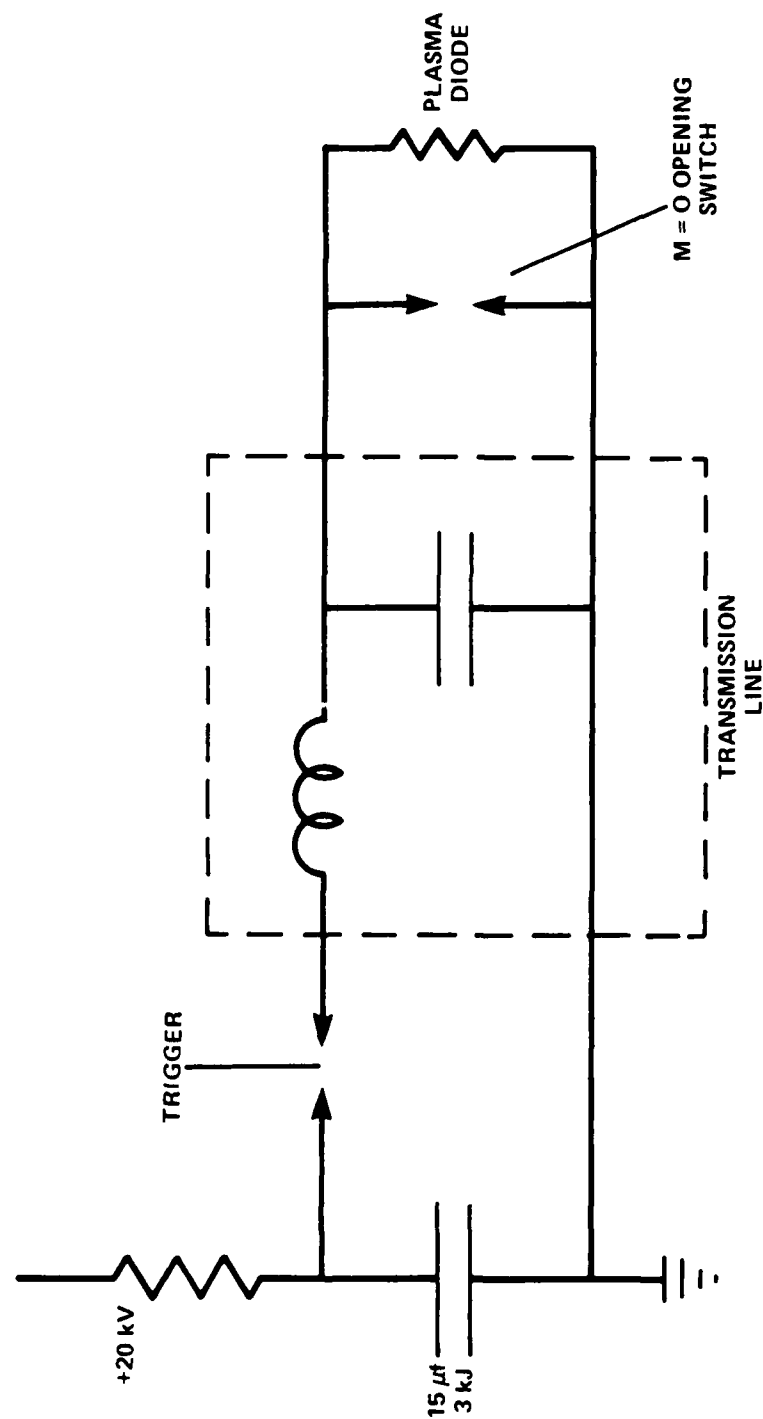


FIGURE 2-4. ELECTRICAL SCHEMATIC OF THE PLASMA FOCUS

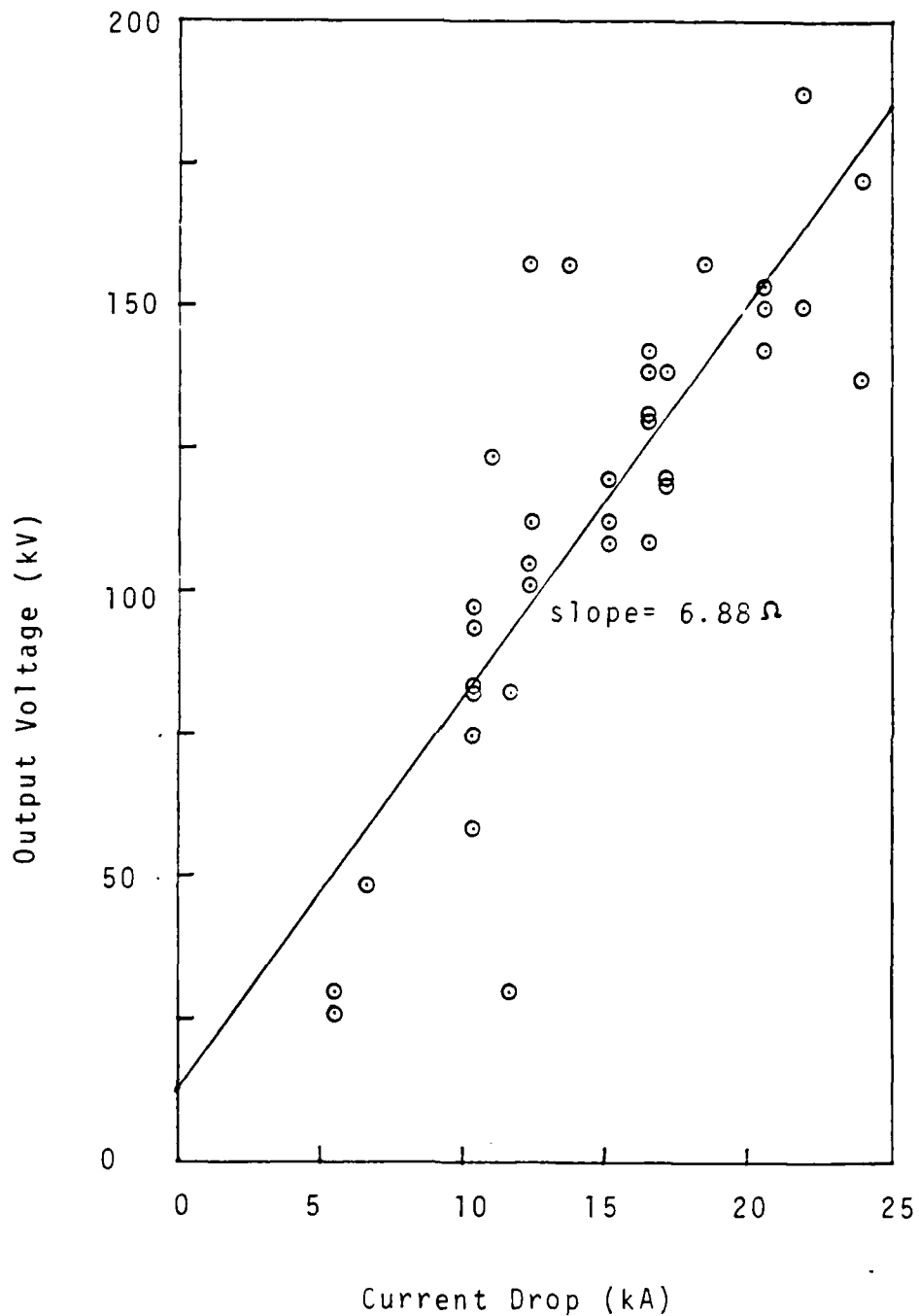
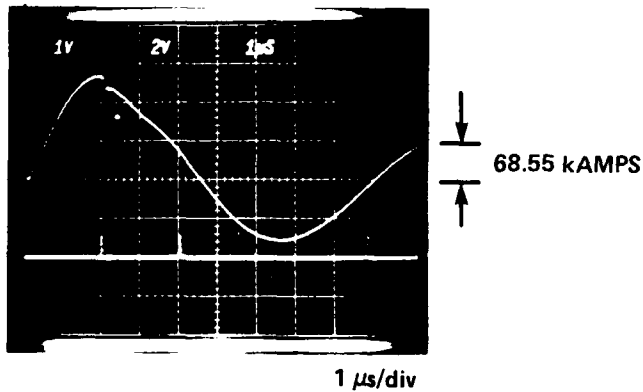
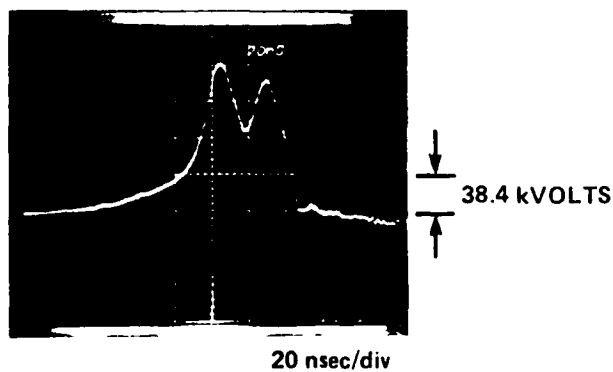


FIGURE 2-5. PLOT OF OUTPUT VOLTAGE VERSUS CURRENT DROP FOR THE PLASMA FOCUS DEVICE TO FIND THE TRANSMISSION LINE IMPEDANCE

(A) TRANSMISSION
LINE CURRENT

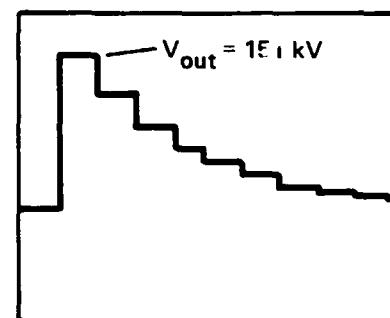
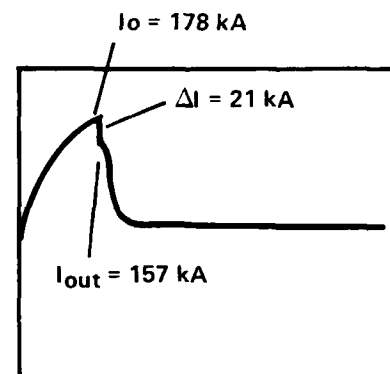


TRANSMISSION
LINE VOLTAGE



$$Z_0 = V/\Delta I = 7.3 \Omega$$

(B) MODEL TRACES



$$R_L = V_{out}/I_{out} = 0.96 \Omega$$

FIGURE 2-6. ANALYSIS FOR DIODE LOAD RESISTANCE R_L (COMPARE WITH FIGURE 1-5)

TRANSMISSION LINE PROBES

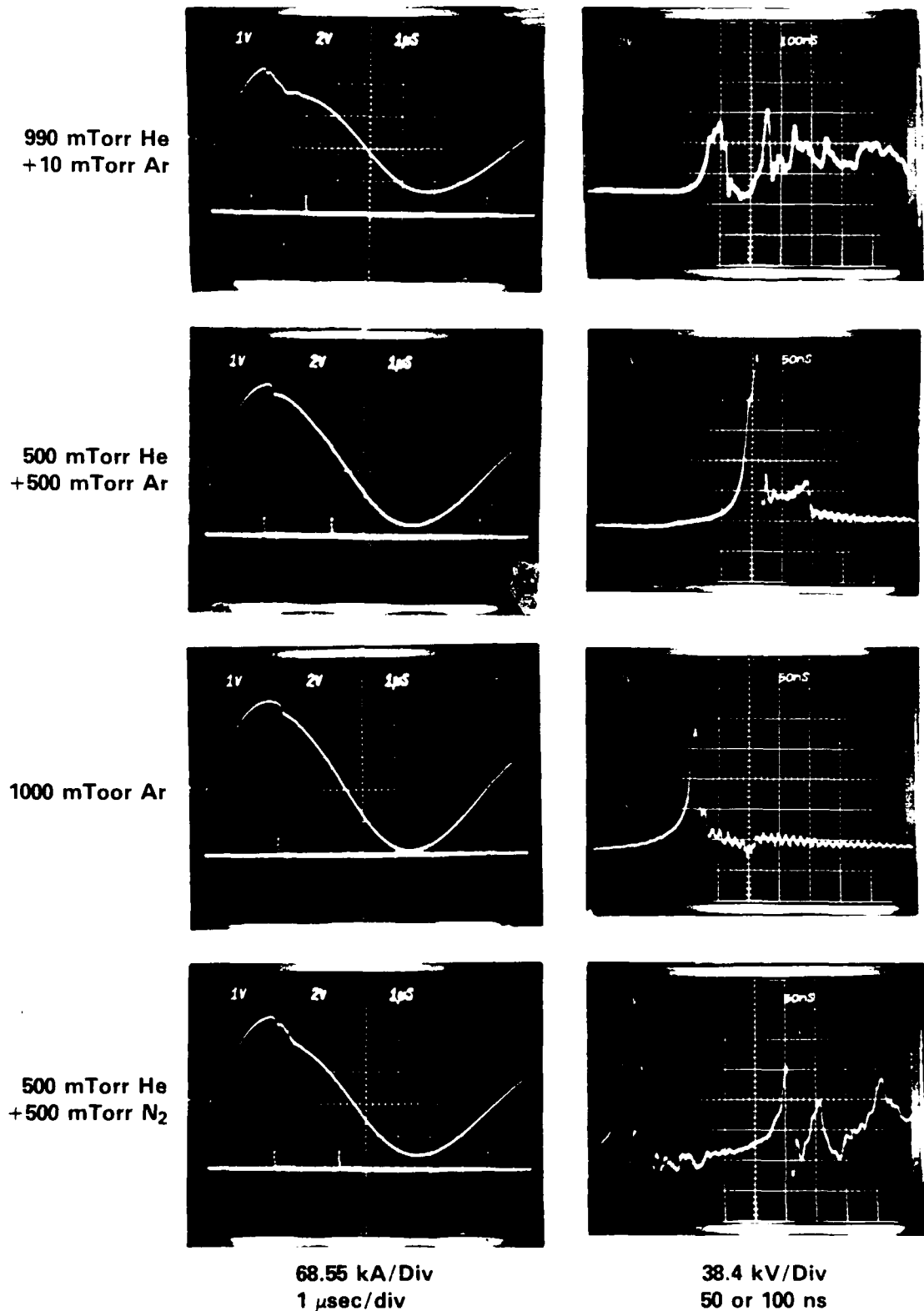


FIGURE 2-7. TRANSMISSION LINE DIAGNOSTICS SIGNALS (INTEGRATED). CURRENT IS ON THE LEFT AND VOLTAGE ON THE RIGHT.

CHAPTER 3

ELECTRON BEAM MEASUREMENTS

ELECTRON BEAM CURRENT MEASUREMENTS

A Rogowski coil has been used to measure the current associated with the electron beam produced by the plasma focus device.²² The coil consists of 12 windings on a plexiglas (poly-methyl methacrylate) ring of 3 mm x 3 mm cross section with a 3.5 cm mean diameter. A voltage is induced between the ends of the windings by the time varying magnetic field produced by the current pulse which passes through the ring. The induced voltage is:

$$\text{emf} = \frac{N\mu_0}{2\pi} \frac{A}{r} \frac{dI}{dt} , \quad (3-1)$$

where A is the cross-sectional area of the ring, N is the number of windings, μ_0 is the permeability of free space, and r is the mean radius. This signal is passed through a simple passive integrating circuit. Exact analysis of the circuit shows the output voltage will be given by:

$$V_{\text{out}} = 1/RC \left(\int V_{\text{in}} dt - \int V_{\text{out}} dt \right) . \quad (3-2)$$

It is readily apparent that if the current pulse timescale is much shorter than the RC time constant, the second term in the above equation is negligible and the Rogowski output will be proportional to the net current flowing through the coil. As the pulse time approaches RC, the correction term is no longer negligible.

With an RC=875 nsec integrator, the proportionality constant, $\frac{1}{RC} \frac{N\mu_0}{2\pi} \frac{A}{r}$, equals 729.1 amps/volt. The actual calibration is found to be 709 amps/volt by passing a known current pulse through the coil.

The Rogowski coil is placed directly at the output of the hollow center electrode drift tube as shown in Figure 1-10.

The signal risetime is calculated to be 0.3 ns, which is adequate for the e-beam. Sample results are shown in Figure 3-1. Figure 3-2 is a plot of the peak current as a function of gas pressure for helium, nitrogen, and argon gas. It should be noted that due to the pressure dependence of the current sheath velocity, the focus will occur earlier, i.e., at lower plasma currents (I_{pf}) at lower pressures. This data is plotted in Figure 3-3. One interesting feature of the current waveforms is the long time scale decay which indicates the flowing of plasma current through the Rogowski coil. As previously described, the current decay time read from this diagnostic requires correction due to the finite RC time of the integrator; however, the peak value of current which occurs quite early in the pulse may be read quite accurately without correction.

A Faraday cup may provide a more sensitive current-measuring device suitable for measuring the very short time scale beam current (10 ns). A 6.7 cm diameter, 1 cm thick graphite block is connected to a 0.05024 ohm T+M Research Products current viewing resistor. In order to maintain high vacuum (10^{-4} Torr) in the Faraday cup region, a foil is placed 2 cm downstream of the center electrode to isolate it from the plasma focus static filling gas. The Faraday cup is placed 1 cm downstream of the foil. This serves to insure that no beam filling gas interaction be recorded at the Faraday cup. The foils may also act as filters in that the foil thickness is comparable to the ranges of electrons in the foil material. In particular, a 6 micrometer thick mylar foil is the range thickness for 20 keV electrons, and a 13 micrometer Titanium foil is the range thickness for 50 keV electrons.⁶² The experimental setup and typical results for both foils are shown in Figure 3-4.⁶³ It is readily apparent that the energetic beam pulse full-width-half-maximum is approximately 5 ns and that the output current peak is 5.0 kA with a 6 μ Mylar foil and 4 ns, 0.64 kA with a 13 μ Ti foil. These presence of lower currents through the Ti foil may be due to the range thickness of the foil. In both foils, a hole is made where the beam passes through, indicating much of the beam energy is deposited in the foils raising the temperature above the melting point.

The dramatic difference between the time scales of the Rogowski coil current diagnostic and the Faraday cup diagnostic indicates the presence in the Rogowski coil results of plasma current induced in the plasma channel created by the beam. In order to investigate this phenomenon, the Faraday cup is connected to a 1.27 cm diameter aluminum rod and inserted into a drift tube of 10 cm inner diameter and 90 cm length. The distance of the Faraday cup from the center electrode beam port is adjustable by changing the length of the rod. The plasma channel, Al rod, and drift tube may be considered a lumped inductive path. The plasma channel has resistivity. Simple Spitzer resistivity for a channel of typical parameters is given by the equation:

$$\eta = 0.0103 \ln(\Lambda) T(\text{eV})^{-3/2} = 0.013 \Omega\text{-cm} . \quad (3-3)$$

Assuming typical parameters, $\ln(\Lambda) = 10$,⁶⁴ $T = 4 \text{ eV}$,⁶⁵ channel cross section = 0.95 cm^2 (estimated from a witness plate exposed 1.25 cm from the beam port in a 0.5 Torr Ar shot shown in Figure 3-5) for a channel length of 12.5 cm the net resistance is 0.171 ohms. Figure 3-6 is an open shutter photograph of the beam induced channel. The inductance of the current path is estimated assuming the current remains on axis, $L = 376 \text{ nH}$. The L/R decay time of this lumped circuit model is $2.20 \mu\text{s}$. This value is comparable to the experimental values found for the decay constant which are plotted in Figure 3-7. This is an indication of the relatively large cross section for ionization of the gas.

ELECTRON BEAM CALORIMETER

In order to better understand the electron beam production in a plasma focus device, a graphite block calorimeter is constructed.^{66,67} Other researchers⁶⁸ have reported large efficiencies in conversion from plasma energy to optical energy. Perhaps even though the beam parameters measured at the end of the center electrode (beam port) indicate relatively low e-beam production efficiency about 1 percent, the total beam energy may be much higher but lost to the walls of the center electrode. Much of this component of the beam may be of the lower energy electrons which may be more efficient in producing optical radiation. Hence, we wish to design a calorimeter capable of measuring the

total beam energy at the entrance to the center electrode as well as along its entire length.

A calorimeter is constructed (see Figure 3-8) from a graphite block to which a YSI44111 thermistor is thermally connected. The thermistor is a negative temperature coefficient resistor which is capable of operating in the range 40° to 150° C. Its resistance at room temperature is 100 kohms. The graphite block is insulated with shrink tubing over most of its length to provide thermal insulation and to force the beam current to pass through the entire length of the graphite. Fingerstock provides electrical contact between the block and ground.

If we consider only the graphite (neglecting heat capacity of the shrink tubing, thermal compound, and thermistor), we can find the beam energy per change in temperature calibration factor. Taking the graphite mass 12.0 gm and multiplying by the heat capacity (Cp) of graphite, 0.712 J/gm-K, we obtain 8.54 J/K. Variations of Cp with temperature are negligible in the range considered. The largest error in the experiment may be the loss of electron beam around the outer edge of the calorimeter. The thermistor, which is placed in the center of the block, provides a very sensitive method of measuring temperatures. In order to produce a record of these changes, the thermistor is connected to a bridge circuit. This circuit is shown in Figure 3-9. A Heath Schlumberger Model SR-255B Chart Recorder is connected between a and b. The voltage here depends on the change in the resistance of the thermistor:

$$V_{ab} = V \left(\frac{1}{1 + R_{T1}/R} \right) - \left(\frac{1}{1 + R_{T2}/R} \right) . \quad (3-4)$$

Within a small error:⁶⁹

$$\frac{R_{T1}}{R_{T2}} = \exp \left[\beta_T \left(\frac{1}{T1} - \frac{1}{T2} \right) \right] , \quad (3-5)$$

we obtain:

$$V_{ab} = V \left[\frac{1}{1 + \frac{R_{T1}}{R} e^{\beta \left(\frac{1}{T_2} - \frac{1}{T_1} \right)}} - \frac{1}{1 + \frac{R_{T1}}{R}} \right], \quad (3-6)$$

where β_T is calculated from data supplied by the thermistor manufacturer, $\beta_T = 4070$ K. Figure 3-10 shows a plot of output voltage versus temperature difference. Since the output voltage depends on the initial balancing of the bridge prior to a shot, there is a weak dependence on initial temperature.

In order to interpret the raw data obtained from the calorimeter diagnostic, it is necessary to have a model by which the chart recorder results can be understood. In the ideal case, a short pulse of power $P = IV$ is input to the calorimeter as in Figure 3.11(A). The duration of the pulse is negligibly small. The calorimeter diagnostic is time integrating. The chart recorder output, which is proportional to total energy, should be a step function as in Figure 3.11(B). In actuality, the calorimeter-thermistor system does not respond instantaneously. The risetime may be many seconds. The exact value depends on the environment immediately surrounding the thermistor. Calibration of the calorimeter in water heat baths give a risetime of 19s. This lies within the range supplied by the thermistor manufacturer (2.5s in well stirred oil, 25s in still air). Taking this risetime into consideration, the true response to a pulse input may be expressed as $A_0(1 - e^{-t/t_r})$ where A_0 is proportional to the energy and t_r is the risetime of the thermistor. See Figures 3-11(C). The last factor, the falltime, is due to heat loss from the calorimeter through surrounding gas, shrink tubing, epoxy, and fingerstock. The heat flow equation^{69,70,71} is:

$$\frac{q}{S_n} = -k \frac{dT(r,t)}{dn}, \quad (3-7)$$

where q is the heat transfer rate, n is a unit vector in a particular direction, S_n is the area perpendicular to n , $T(r,t)$ is the temperature, and k is the

thermal conductivity of the medium. In one dimension, we can integrate from x_1 to x_2 to obtain:

$$q = kS \frac{(T_1 - T_2)}{(x_1 - x_2)} , \quad (3-8)$$

where $T_{1,2} = T(x_{1,2})$. In cylindrical coordinates, the corresponding equation integrated from r_1 to r_2 over a z length Z is:

$$q = 2\pi kZ \frac{(T_1 - T_2)}{\ln(r_2 / r_1)} . \quad (3-9)$$

For the graphite block, the heat energy stored is $m_g Cp(T - T_{\text{initial}})$ where $m_g Cp$ is the product of mass and heat capacity of the graphite. The heat energy flow rate from the calorimeter is:

$$q = \frac{d}{dt} [m_g Cp (T - T_{\text{initial}})] . \quad (3-10)$$

Setting this equal to the expression above and assuming room temperature as the initial temperature bath, we arrive at the equation:

$$\Delta T = \Delta T_0 e^{-(t/t_f)} , \quad (3-11)$$

where ΔT_0 is the maximum(initial) temperature difference and:

$$t_f = m Cp \frac{\ln(r_2 / r_1)}{2\pi kZ} . \quad (3-12)$$

The quantity t_f can be thought of as a falltime that must be incorporated into the calorimeter response which may be described by the equation:

$$A_0(1 - e^{-(t/t_r)}) e^{-(t/t_f)} , \quad (3-13)$$

See Figure 3-11(D). Since there are many unknowns in the calculation of t_f , edge corrections, effective fingerstock conduction, etc., we will only use the value of t_f obtained experimentally from the output of the chart recorder. The quantity A_0 , or equivalently ΔT_0 , can then be extrapolated from the raw data. The total energy absorbed by the graphite is $m_g Cp \Delta T_0$ where ΔT_0 near room

temperature is 0.183 K/mV ΔV ; hence, total energy per output voltage calibration factor is 1.56 J/mV.

The energy absorbed by the graphite at differing total inductive energy during focus is shown in Figure 3-12. The error bars are representative of uncertainty in t_r and t_f measurements. Notice that only argon gas, which shows best reproducibility of shots as judged by the transmission line voltage probe, shows fairly well defined slopes at the two filling pressures tested. The lines are indicative of the efficiency of inductive energy conversion into beam energy, i.e., 0.6 percent at 2 Torr and 1.4 percent at 0.1 Torr Ar. The most convenient feature of this diagnostic is that it may be inserted into the hollow center electrode so that we may study the energy transport along this length. Figure 3-13 shows how the beam energy is transported for a pressures of 2 and 0.5 Torr argon. The solid line indicates the uniform beam divergence line. The lack of agreement shows the importance of space charge effects of beam propagation down the tube.

ELECTRON ENERGY MEASUREMENTS

A simple magnetic analyzer, based on principles common to many analyzers used by others, has been designed with a view towards compactness and versatility.⁷²⁻⁷⁵ In a uniform magnetic field, the electron will follow a circular path with the Larmor radius $r_L = p/eB$, where p is the relativistic mechanical momentum, B is the magnetic field, and e is the electronic charge. The kinetic energy T corresponding to the radius r_L is given by:

$$T = [(ecBr_L)^2 + (m_e c^2)^2]^{1/2} - m_e c^2, \quad (3-14)$$

where c is the velocity of light and m is the electron rest mass. Measurement of the Larmor radius is accomplished in the semicircular focusing electron energy analyzer shown in Figure 3-14.

The double slit collimation system in Figure 3-14 limits the acceptance angle and width of the electron beam, i.e., system resolution. The thickness of the material used for the slits in the collimator should be greater than the

range of the most energetic electrons. For example, in copper, the range of 1.5 MeV electrons is approximately 1 gm/cm^2 . At a density of approximately 9 gm/cm^3 , a 1.1 mm thickness of copper is used.

A uniform magnetic field of 0.53 Tesla is produced by a single rare earth cobalt magnet of dimension $2.54 \times 2.54 \times 0.64 \text{ cm}$ with a 0.23 cm separation from a symmetric piece of soft iron. The detectable energy range is 20 KeV-1.5 MeV. The detector used in this spectrometer is an approximately 100 micron thick coating of phosphor P31 deposited on an aluminum substrate. Since the plasma focus is operated with a Torr range pressure in the diode region, it is desirable to provide for the maintenance of vacuum in the energy analyzer in order to avoid an electron beam-filling gas interaction which could interfere with measurements. A fast gate valve operated by a solenoidal plunger system is ideal for this purpose. See Figure 3-15. The collimator is placed immediately after the gate valve. Upon the opening of the valve, the electron beam is injected through the collimator and travels a semi-circular trajectory to the detector. The results of each shot are recorded on 35 mm black and white film by taking an open shutter photograph of the phosphor during exposure to the electron beam. A microdensitometer scan of the developed film yields information about the energy distribution within the beam. The microdensitometer scans the optical density of the film, which may not necessarily be linear to the phosphor exposure; hence, quantitative information about the energy spectrum is not accurately determined by this method. In obtaining the energy data, it is assumed that the distance from the center of the collimator slit to a point on the phosphor where light is emitted is the radius of the electron orbit in the uniform field. Such an assumption is rigorously true for perfect collimation, a uniform magnetic field configuration, and electron orbits unaffected by space-charge. Under these ideal conditions, we may convert from distance to energy measurement by writing the energy in convenient laboratory units:

$$T = [(0.015Bs)^2 + (0.511)^2]^{1/2} - 0.511 \quad (\text{MeV}) , \quad (3-15)$$

where B is the magnetic field in kG and s is the diameter of the orbit in mm. The resolution of this spectrometer is discussed in Appendix A.

Figures 3-16 and 3-17 show results for a typical series of Ar filling gas shots. Table 3-1 summarizes peak energies obtained for argon and nitrogen gas series as determined by the sensitivity of the detection system, i.e., amount of phosphor light, f-stop of camera, and film sensitivity. These were done on a different day than the results shown in Figures 3-16 and 3-17. An obvious notable characteristic is the irreproducibility of the beam energy output of the device. In fact it was observed that in many instances, nitrogen, gas did not show any result. This was even more pronounced in the cases of helium and hydrogen.

TABLE 3-1. COMPARISON OF Ar AND N₂ SERIES

GAS	TORR	PF CURRENT(KA)	PEAK ENERGY OF BEAM(KEV)
Ar	0.2	55	114
Ar	0.5	127	123
Ar	0.8	144	217
Ar	1.6	137	123
Ar	2.0	137	118
N ₂	0.3	130	85
N ₂	0.5	137	121
N ₂	1.0	144	none

ELECTRON BEAM EMITTANCE

Beam quality measurements are often described in terms of emittance which is defined as the area occupied by the beam in transverse trace space (coordinates = $x, y, dx/dz, dy/dz$), $\int dx dy dx' dy'$ irregardless of the density distribution $f_4(x, y, x', y')$. In many cases the actual density distribution may be defined by a Gaussian function which does not have finite limits; hence, the emittance would be infinite. In addition, emittance is an invariant quantity in

systems without space-charge interactions⁷⁵ (Liouville's theorem); therefore, erosion of beam quality due to filamentation would not be represented. In order to account for these aspects of beam quality, root-mean-square (rms) emittance has been defined as:⁷⁵⁻⁷⁸

$$\epsilon_{\text{rms}} = 4[\langle x^2 \rangle \langle x'^2 \rangle - \langle xx' \rangle^2]^{1/2}, \quad (3-16)$$

where $\langle \phi \rangle$ represents the value defined by:

$$\langle \phi \rangle = \frac{1}{N} \int \phi f_4(x, y, x', y') dx dy dx' dy', \quad (3-17)$$

where $N = \int f_4 dx dy dx' dy'$.

It has been pointed out by Lawson⁷⁹ that the rms emittance of a beam is closely related to its entropy.

Experimental determination of $f_4(x, y, x', y')$ or $f_2(x, x') = \int f_4(x, y, x', y') dy dy'$ may be accomplished in a number of ways. The most simplistic may be two analyzers each having an aperture through which a portion of the beam may pass. Emittance meters of this double aperture type may be classified into one of four varieties depending on the types of apertures in the two analyzers, i.e., hole-hole, hole-slit, slit-hole, or slit-slit. Let us consider, for example, a hole-hole emittance meter. The upstream analyzer selects a certain x, y position within the beam allowing only a small beamlet to pass through it. Then as the downstream analyzer is moved about, only the beamlet particles with slopes x', y' determined by the relative positions of the two analyzers may pass through. The intensity distribution f_4 may be monitored by a current collector placed immediately behind the downstream analyzer. A drawback to this technique is that one requires a continuous beam or one that is continuously reproducible, over many shots, which is often not the case in the plasma focus device. In order to characterize the beam in a plasma focus device, we require an emittance meter capable of obtaining single shot data. A single shot emittance meter^{80,81} has been designed for use on Febetron and an IREB device. The meter used here employs a radiachromic film detector⁸² placed 4.32 mm downstream from a series of 400 μm wide parallel slits placed 5.5 mm apart. See Figure 3-18. The film

darkens subsequent to exposure to the electron beam; its optical density is proportional to exposure up to an optical density of approximately 1.0. The film may be scanned with an optical densitometer to determine emittance. This emittance meter may be classified as a slit-hole emittance meter, since the film is scanned through the pinhole of the microdensitometer. It should be pointed out that of the above mentioned four varieties of emittance meters, only the slit-hole meter is somewhat less straightforward to analyze. In order to facilitate analysis, certain assumptions are made which allow us to require only the scan along the central y-axis of the exposed film. The measured intensity pattern is proportional to⁸³ $\int f_4(x, Ly', x', y') dy'$. If f_4 is a slowly varying function of y within a range $\Delta y = \pm L\sigma$ where σ is the rms value of y' , then the measured intensity pattern is approximately equal to the one obtained by the hole-slit meter,

$$f_3(x, y, x') = \int f_4(x, y, x', y') dy' . \quad (3-18)$$

This condition is easily met in beams with a small transverse temperature or meters with a small slit-detector distance, L. In addition, our analysis will consider only axisymmetric beams, i.e., all measurable quantities are functions of $r = \sqrt{x'^2 + y'^2}$ only. Also, zero beam rotation is assumed with a thermal (Maxwellian) distribution in $x' = dx/dz$ and $y' = dy/dz$ space. These may be quite reasonable assumptions for a real beam in the absence of external magnetic field. Under these assumptions, the overall trace space distribution function f_4 may be given by:

$$f_4(x, y, x', y') = g(x, y) \exp\left\{-\left[(x' - \bar{x}')^2 + (y' - \bar{y}')^2\right]/2\sigma^2(x, y)\right\} , \quad (3-19)$$

here $g(x, y) = g(r)$ is the x-y spatial dependence of the distribution function, $\sigma(x, y) = \sigma(r)$ is the rms value of the angle (velocity) in $x'-y'$ space given by:

$$\sqrt{\left\{\int [(x' - \bar{x}')^2 + (y' - \bar{y}')^2] f_4 dx' dy' / \int f_4 dx' dy'\right\}} , \quad (3-20)$$

and $\bar{x}'(r)$ and $\bar{y}'(r)$ are the mean angles in $x'-y'$ space given by:

$$\int (x' \text{ or } y') f_4 dx' dy' / \int f_4 dx' dy' , \quad (3-21)$$

which are typically due to overall beam divergence or convergence. We have written x, y explicitly in the above equations to point out the fact that the film is scanned along the $y=0$ axis (actually, we assume the film's $y=0$ axis is the same as the upstream analyzer's $y=0$ axis) and cylindrical symmetry determines the parameters $g(x, y)$, $\sigma(x, y)$, $\bar{x}'(x, y)$, and $\bar{y}'(x, y)$ in full $x-y$ space.

An analytical method of analyzing experimental data produced by a slit-hole emittance meter shall be presented.⁸³ The slits at x_i on the upstream analyzer produce sheet beamlets which impact on the detector revealing their individual angular distributions by the amount of spread as shown in Figure 3-19. This is measured quantitatively with the microdensitometer which shows typically a gaussian profile with peak height β_i , rms width σ_i and displacement \bar{x}'_i . Continuous functions, $\beta(x)$, $\sigma(x)$, and $\bar{x}'(x)$, may be constructed from the discrete sets of data. In fact, a computer program has been written which will fit β/σ to a gaussian, σ to a second order polynomial, and $\alpha = \bar{x}'(x) r/x$ to a linear function. Since all quantities are assumed to be measured along $y=0$, we find due to symmetry that $\beta(r)=\beta(x)$, $\sigma(r)=\sigma(x)$, and $\alpha(r)=\alpha(x)$. It has been shown that by utilizing a transformation of the type:⁸³

$$\int_0^\infty R(r) dy = \int_x^\infty \frac{R(r) r dr}{\sqrt{(r^2 - x^2)}} , \quad (3-22)$$

the quantities needed for emittance may be found as:

$$\langle x^2 \rangle = \frac{4\sqrt{2\pi}}{N} \int_0^\infty x^2 \int_x^\infty \frac{\beta \sigma r dr}{\sqrt{(r^2 - x^2)}} dx , \quad (3-23)$$

$$\langle x'^2 \rangle = \frac{4\sqrt{2\pi}}{N} \int_0^\infty \left[\int_x^\infty \frac{\beta \sigma^3 r dr}{\sqrt{(r^2 - x^2)}} + x^2 \int_x^\infty \frac{\alpha^2 \beta \sigma dr}{r \sqrt{(r^2 - x^2)}} \right] dx , \quad (3-24)$$

$$\langle xx' \rangle = \frac{4\sqrt{2\pi}}{N} \int_0^\infty x^2 \int_x^\infty \frac{\alpha \beta \sigma dr}{\sqrt{(r^2 - x^2)}} dx , \quad (3-25)$$

where,

$$N = 4\sqrt{2\pi} \int_0^\infty \int_x^\infty \frac{\beta \sigma r \, dr}{\sqrt{(r^2 - x^2)}} \, dx . \quad (3-26)$$

Figure 3-20 shows a microdensitometer scan of a radiachromic film which was exposed at the end of the center electrode as it leads into the 10 cm diameter drift tube. The shot was a 750 mTorr Ar gas shot with a plasma current of 150 kA at focus. For this shot, the radiachromic film was covered with a 0.00025-inch thick aluminum foil to prevent ultraviolet or low energy electrons from exposing the film. Only three slits across the meter were exposed since the hollow center electrode diameter is 14.4 mm and the slit separation is 5.5 mm. It should be emphasized here that this measurement was performed at the center electrode beam port since the beam emittance may vary as the beam propagates further downstream due to scattering, space charge, etc. The σ value at the center of the beam is 630 mrad and at $x = 5.5$ mm, the value is 550 mrad. The value of α fit to a straight line is 0.021r, and the overall spatial distribution is approximately a flat top. From Equations (3-23) through (3-25) we find the rms emittance for a flat top spatial distribution with a Gaussian transverse velocity profile to be given by:

$$2b\sigma_0 , \quad (3-27)$$

where b is the radius of the flat top distribution and σ_0 is the peak of the rms width function σ . Plugging in the values $b=7.2$ mm, $\sigma_0=560$ mrad, we get 8060 mm-mrad. A computer program has been written (Won Namkung) which enables us to numerically integrate the equations for the rms values. The program results show a rms emittance of 8040 mm-mrad. A two-dimensional contour plot of $f_2(x,x')$ is shown in Figure 3-21.

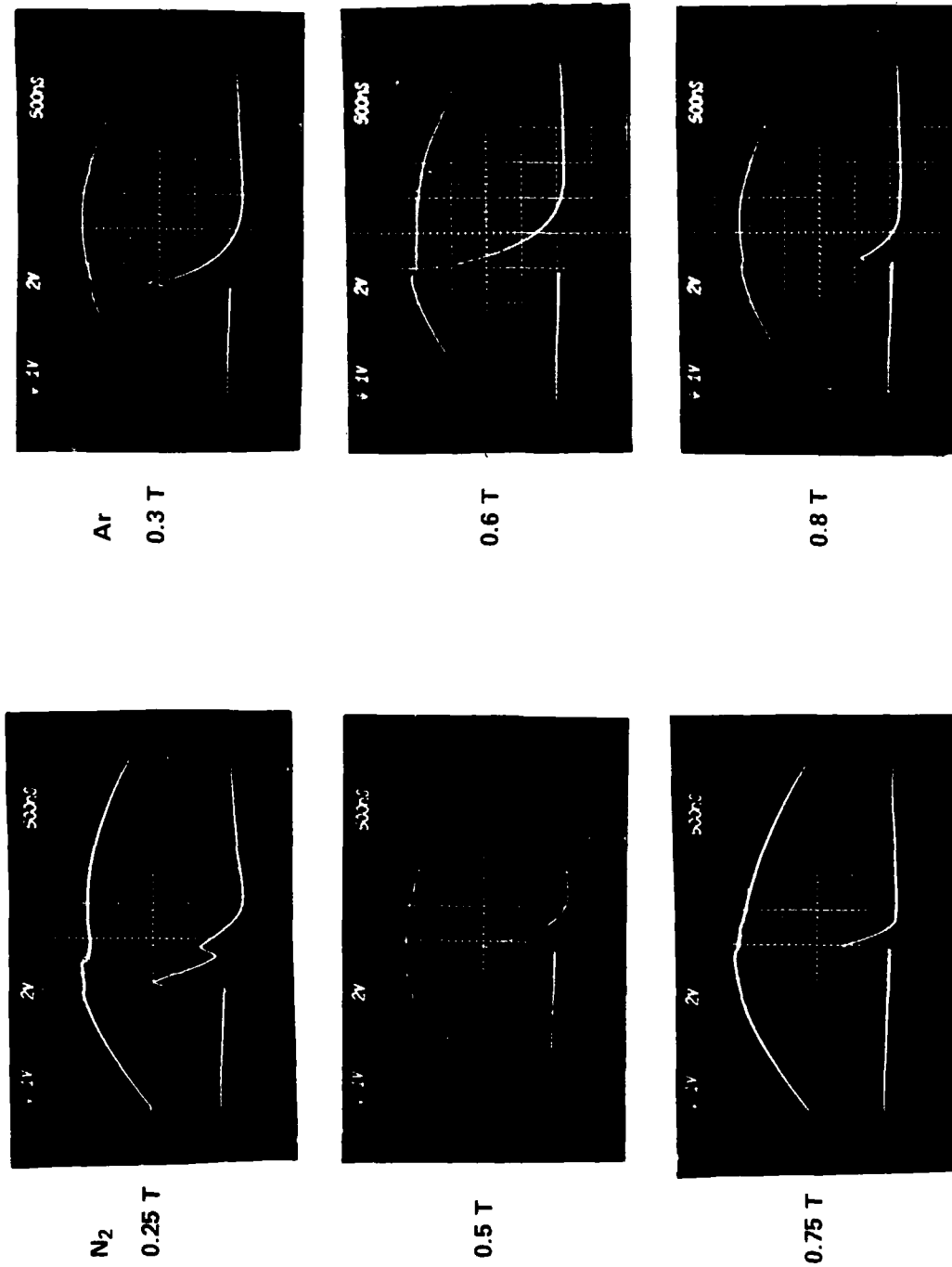


FIGURE 3-1. E-BEAM ROGOWSKI COIL TRACES (INTEGRATED) 1.42 kA/div

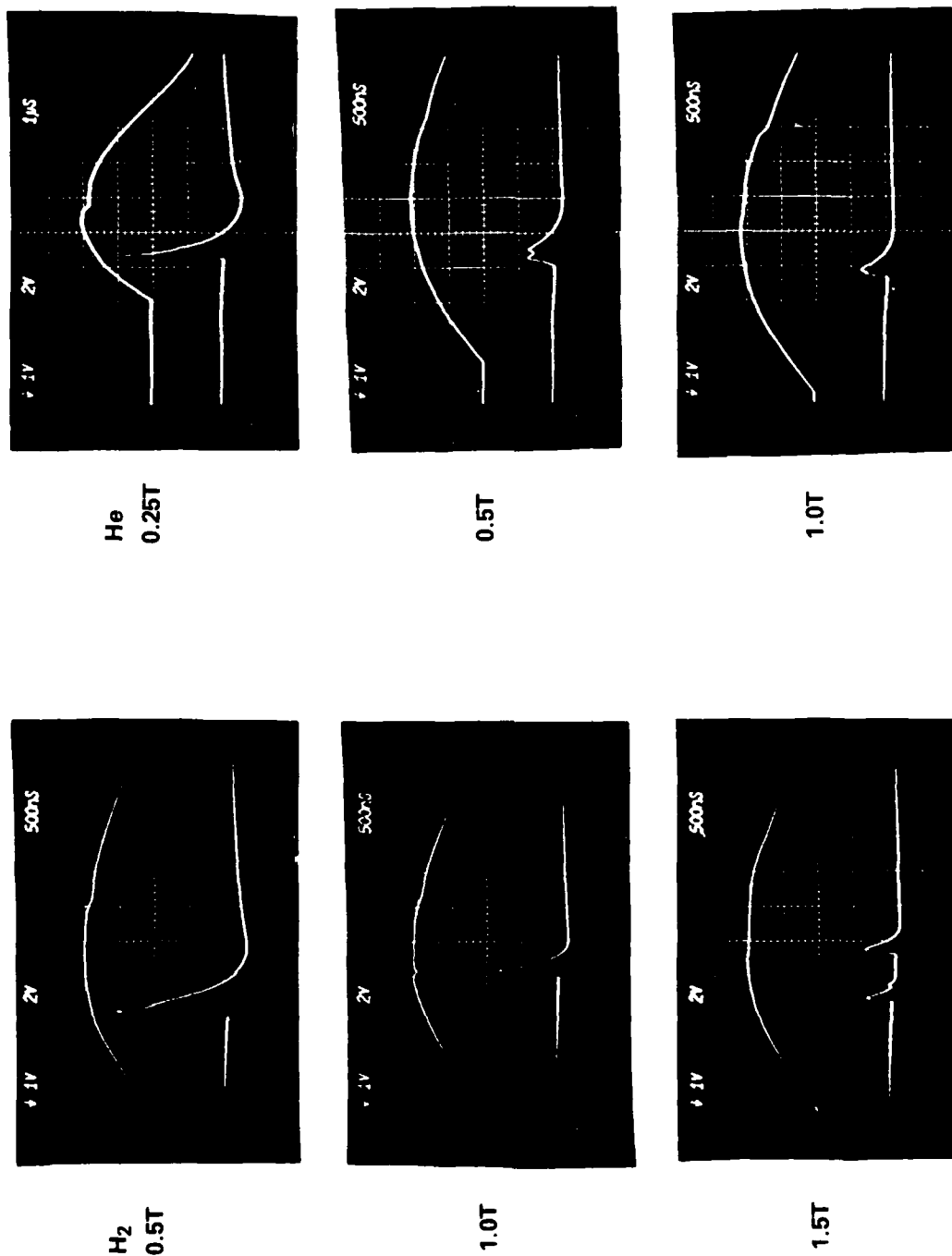


FIGURE 3-1. (CONT.) E-BEAM ROGOWSKI COIL TRACES (INTEGRATED)
1.42 kA/div.

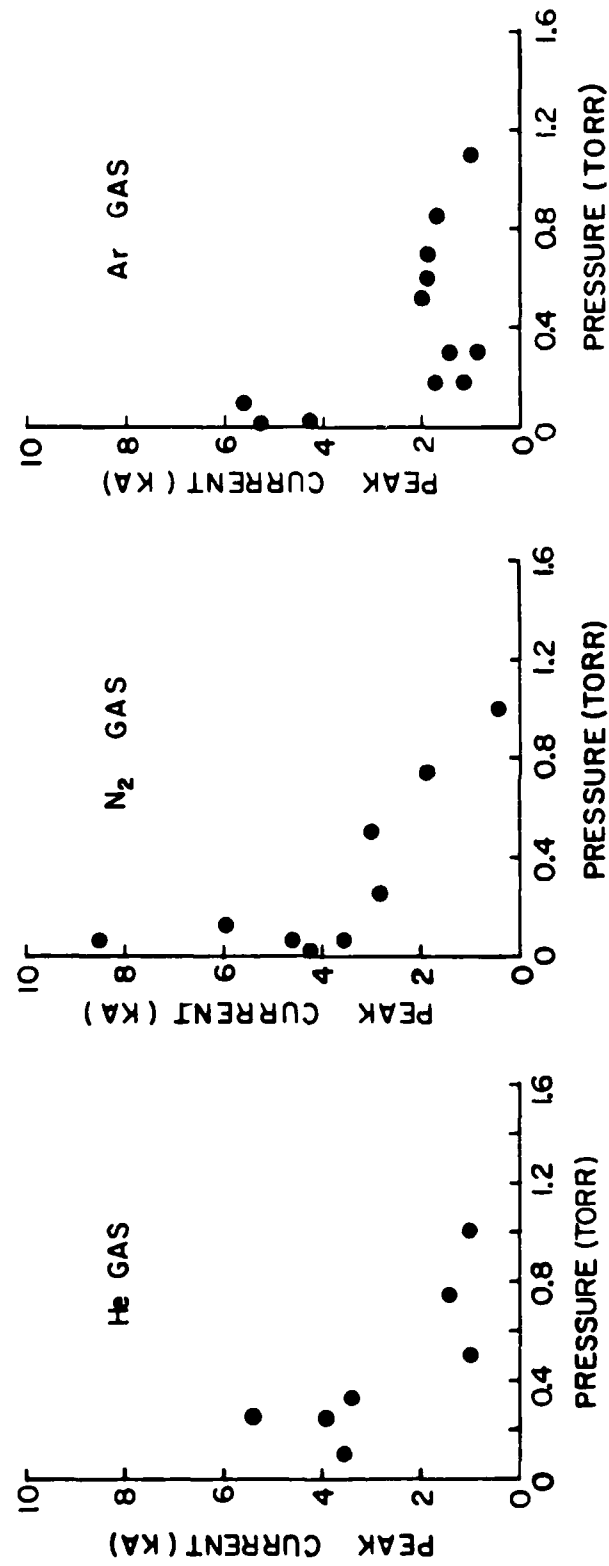


FIGURE 3-2. PLOT OF PEAK ELECTRON BEAM CURRENT AS A FUNCTION OF PRESSURE FOR A VARIETY OF FILLING GAS

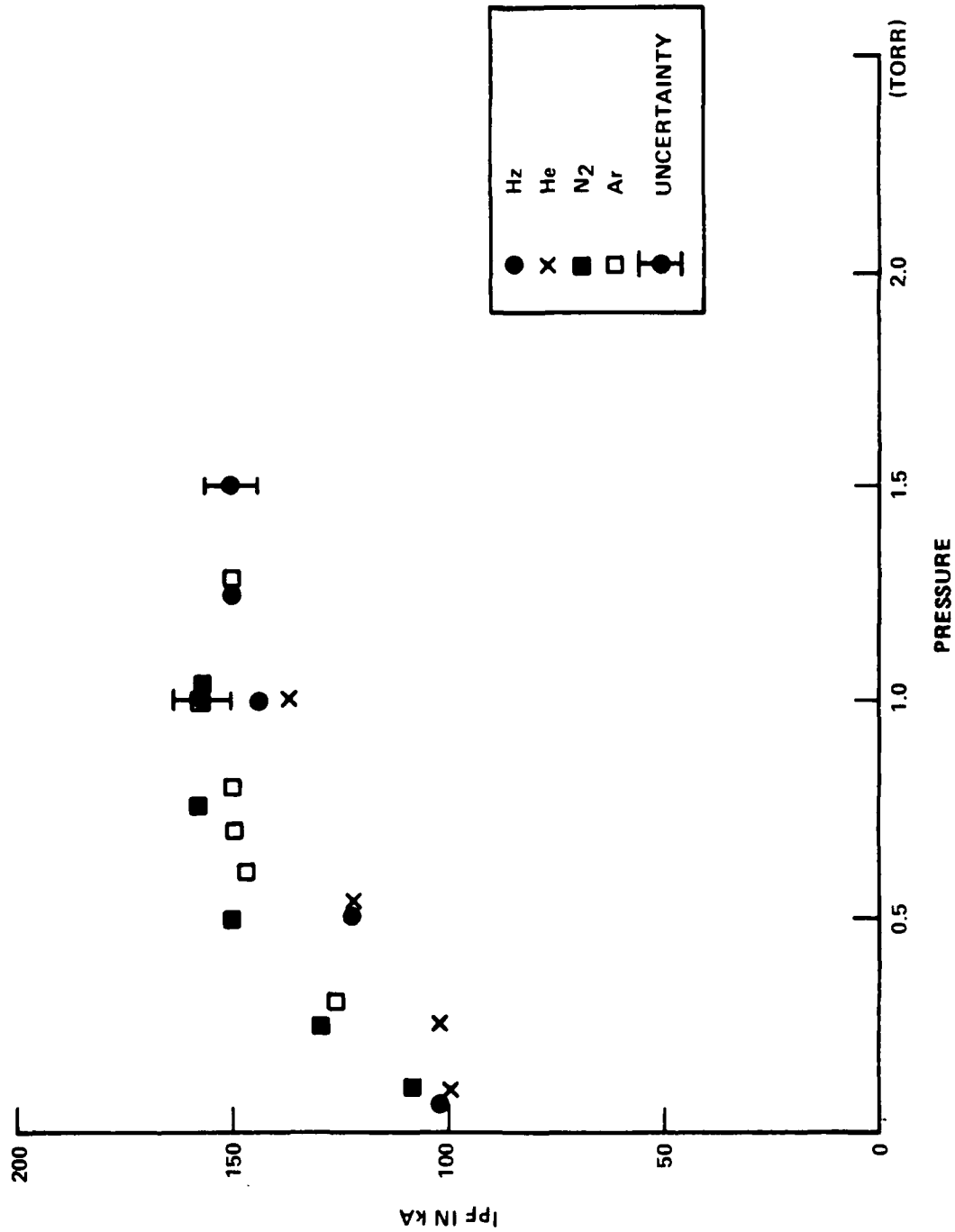


FIGURE 3-3. PLOT OF BANK CURRENT AT FOCUS I_{pf} VERSUS PRESSURE FOR A VARIETY OF FILLING GAS

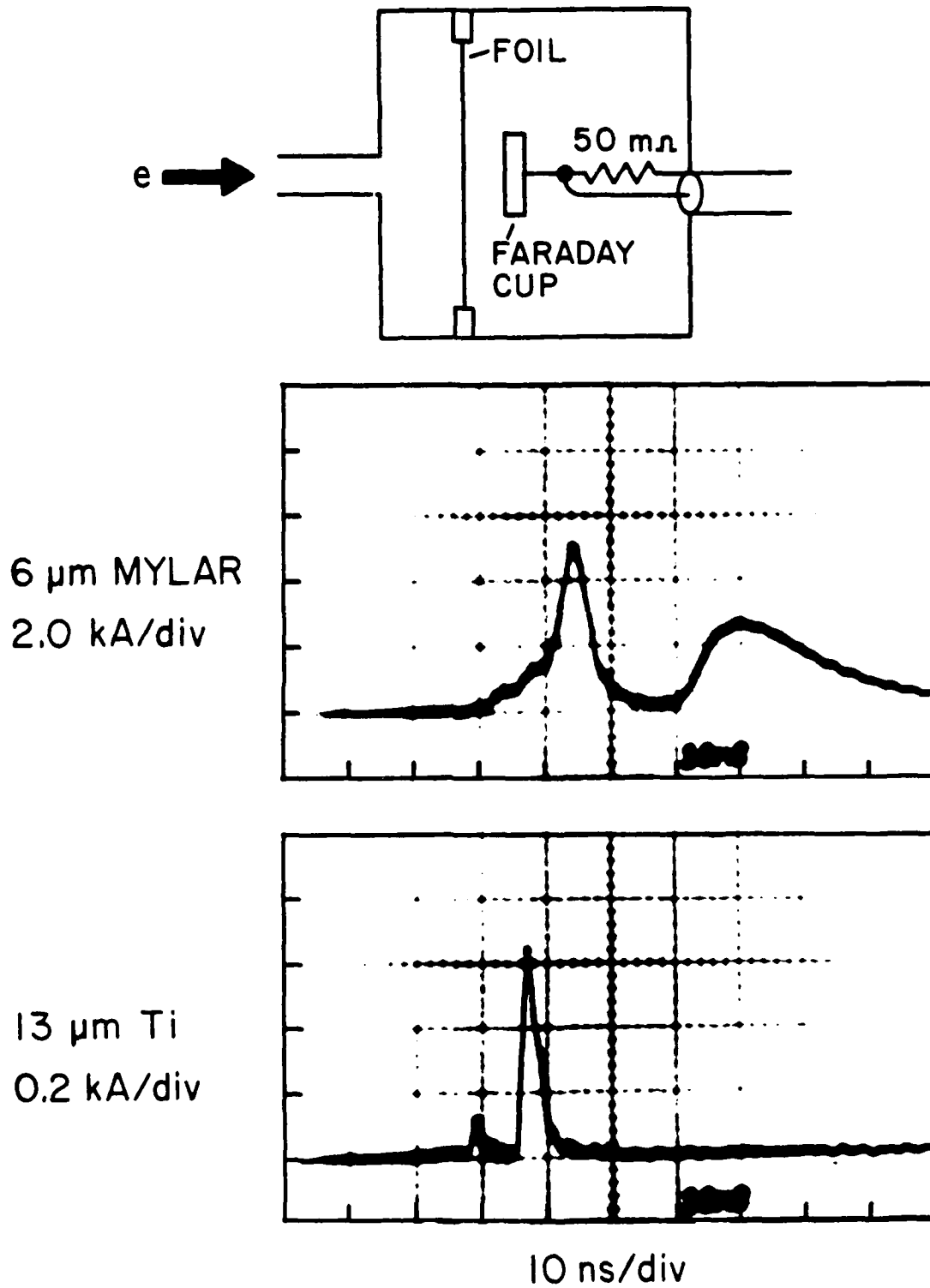


FIGURE 3-4. FARADAY CUP DIAGNOSTIC WITH CURRENT SIGNALS

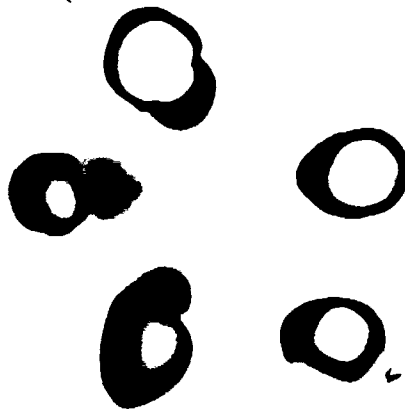


FIGURE 3-5. WITNESS FILM FOR ELECTRON BEAM (FIVE EXPOSURES ON A WITNESS FILM FOR E-BEAM IN 0.5 TORR Ar)



FIGURE 3-6. OPEN SHUTTER PHOTO OF E-BEAM. OPEN SHUTTER PHOTOGRAPH OF BEAM PASSING THROUGH 0.32 TORR Ar. IN THE CENTER OF THE PHOTO IS A GRAPHITE BLOCK CONNECTED TO 1/2-INCH Al ROD FOR FARADAY CUP MEASUREMENTS.

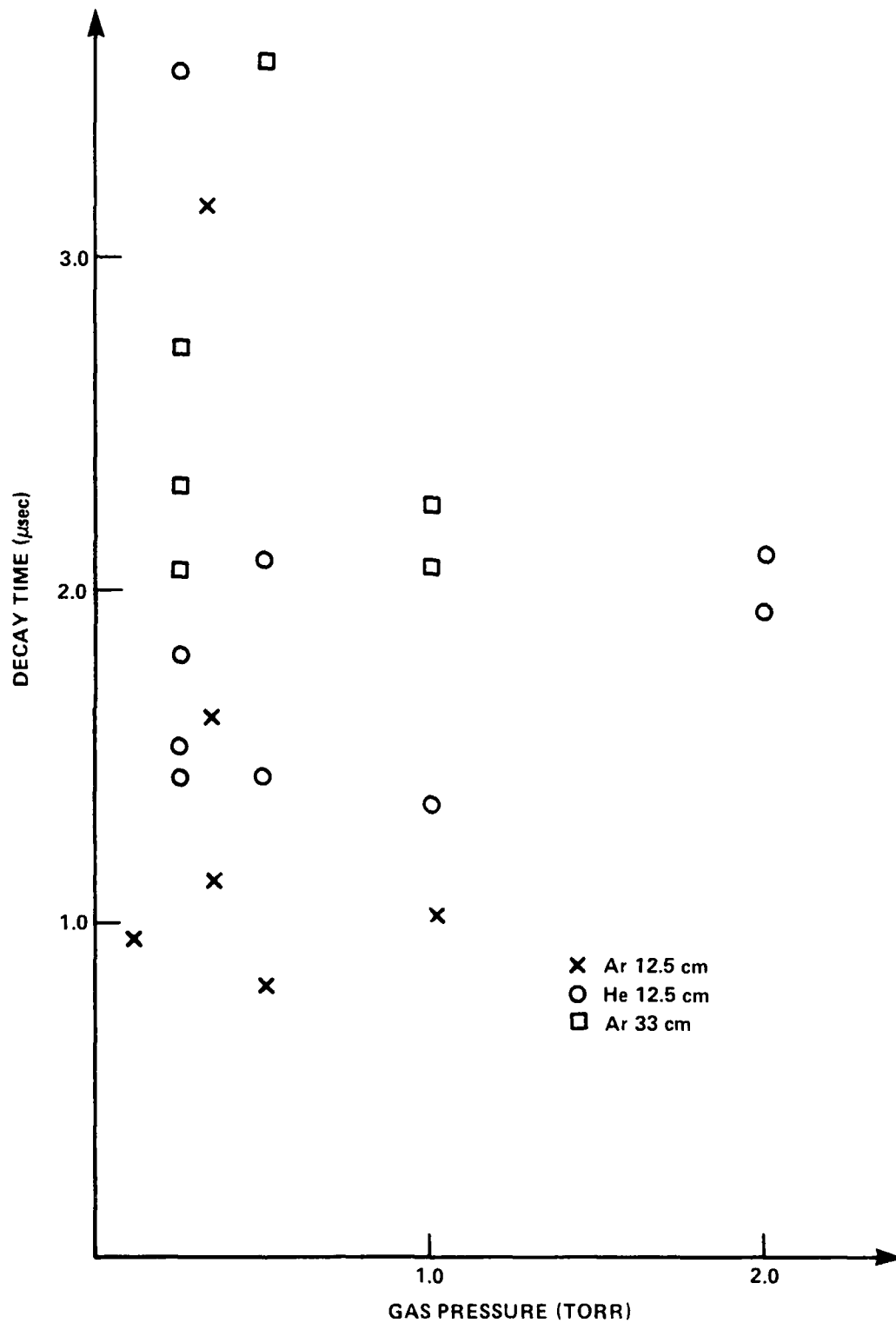


FIGURE 3-7. PLOT OF ELECTRON BEAM INDUCED PLASMA CURRENT DECAY TIME AS A FUNCTION OF GAS PRESSURE AND DISTANCE WHERE THE FARADAY CUP IS 12.5 AND 33 cm FROM THE BEAM PORT

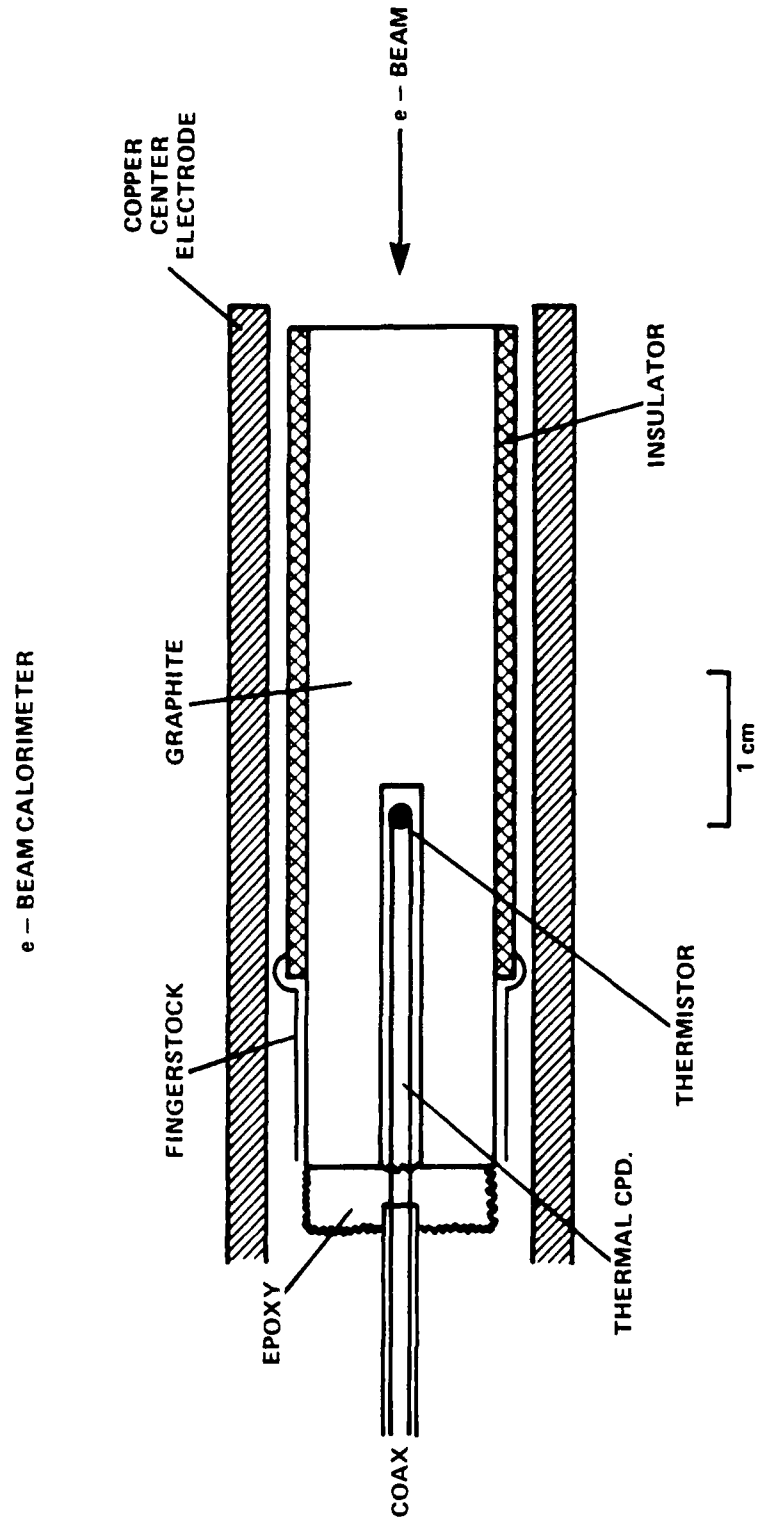


FIGURE 3-8. E-BEAM CALORIMETER

CALORIMETER BRIDGE

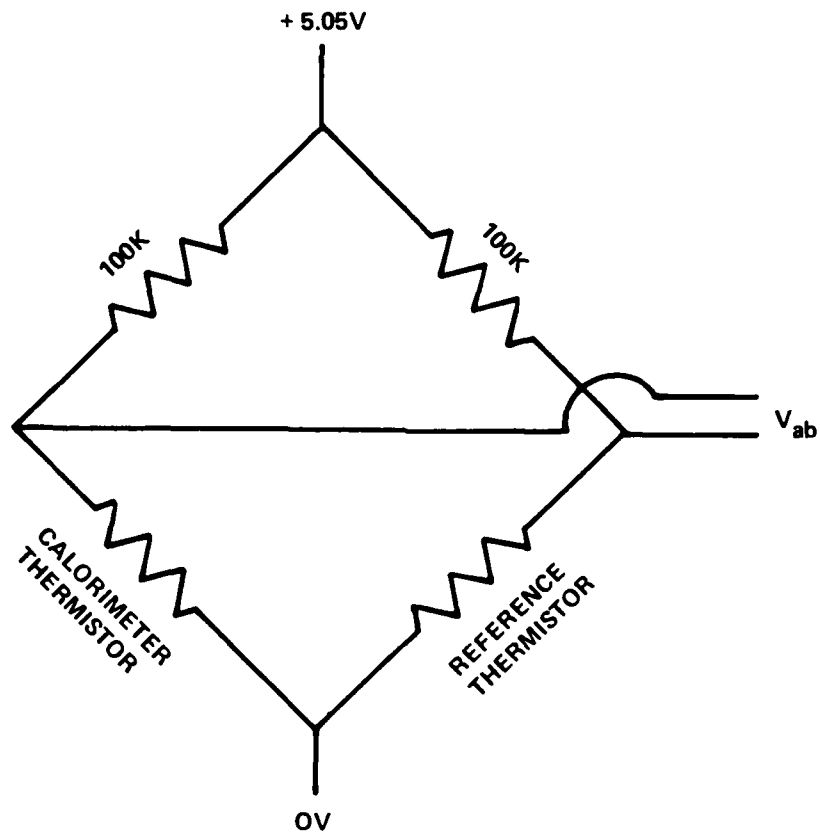


FIGURE 3-9. CALORIMETER BRIDGE CIRCUIT. THE CHART RECORDER MEASURES V_{ab} .

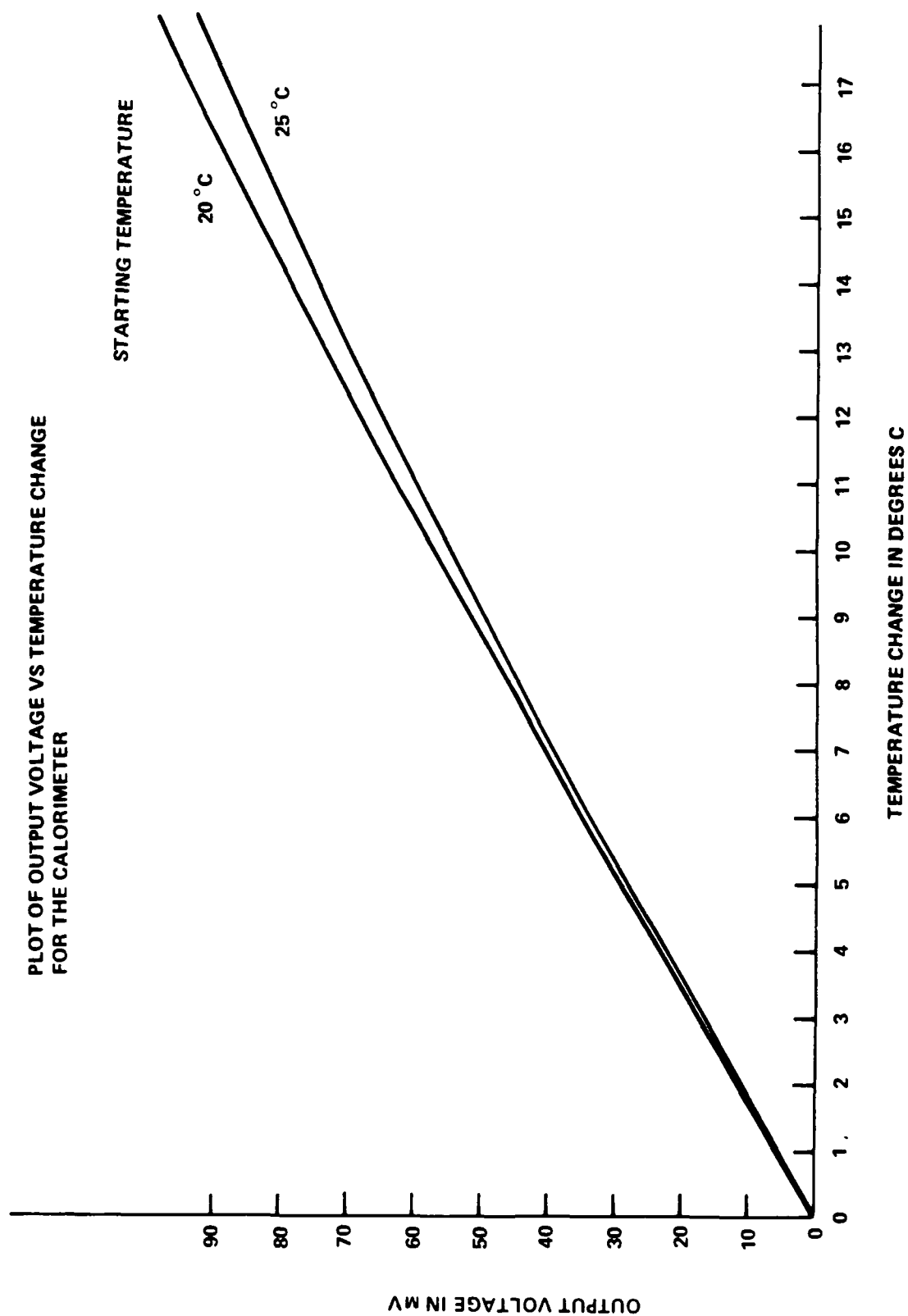


FIGURE 3-10. OUTPUT VOLTAGE OF BRIDGE AS A FUNCTION OF THERMISTOR CHANGE
IN TEMPERATURE FOR THE APPLIED VOLTAGE 5.05 V

CALORIMETER RESPONSE

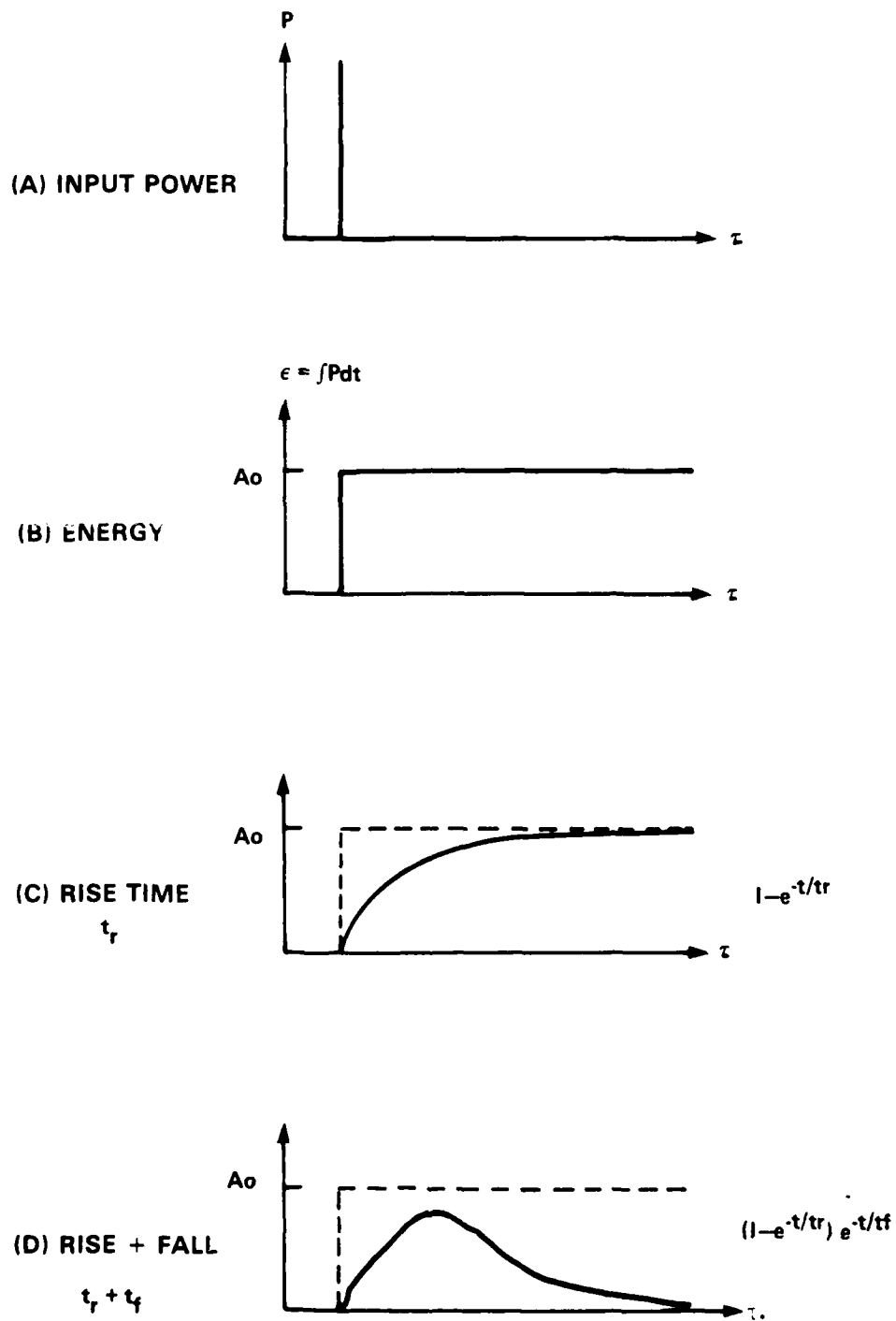


FIGURE 3-11. ANALYSIS OF CALORIMETER RESPONSE

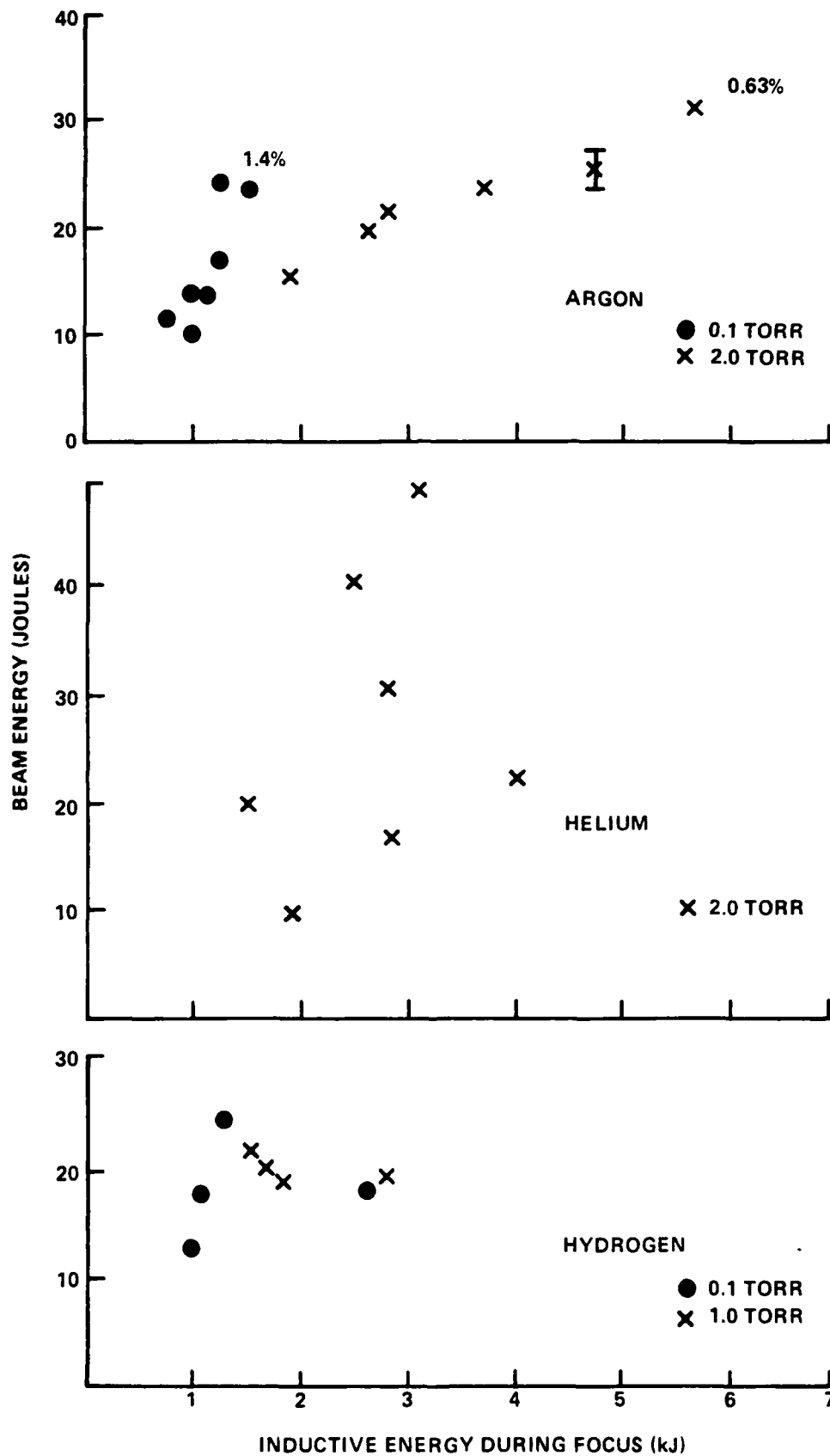


FIGURE 3-12. PLOT OF TOTAL BEAM ENERGY AS A FUNCTION OF TOTAL INDUCTIVE ENERGY DURING FOCUS FOR CONVERSION EFFICIENCY

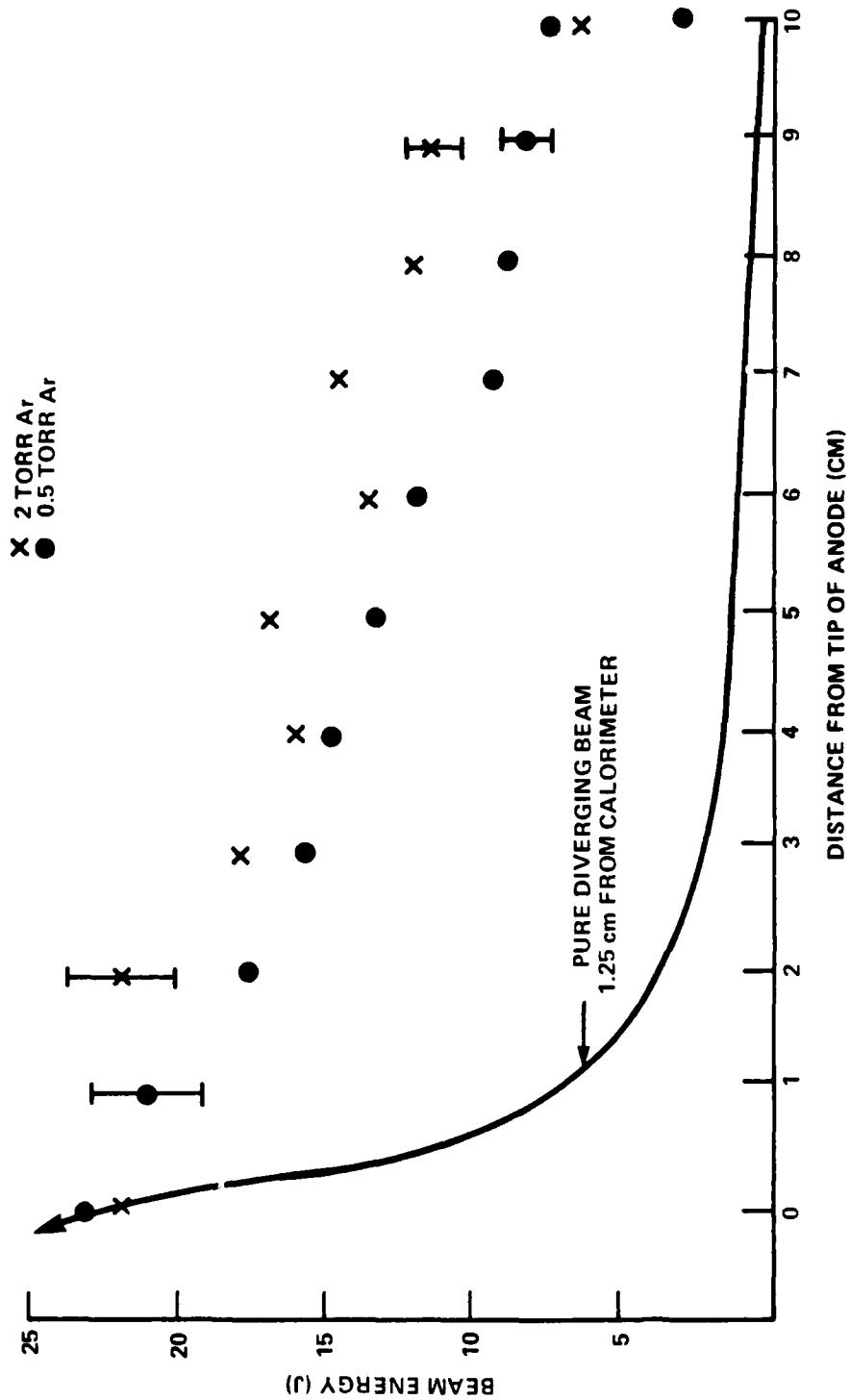


FIGURE 3-13. PLOT OF TOTAL BEAM ENERGY AS A FUNCTION OF DISTANCE DOWN THE HOLLOW CENTER ELECTRODE

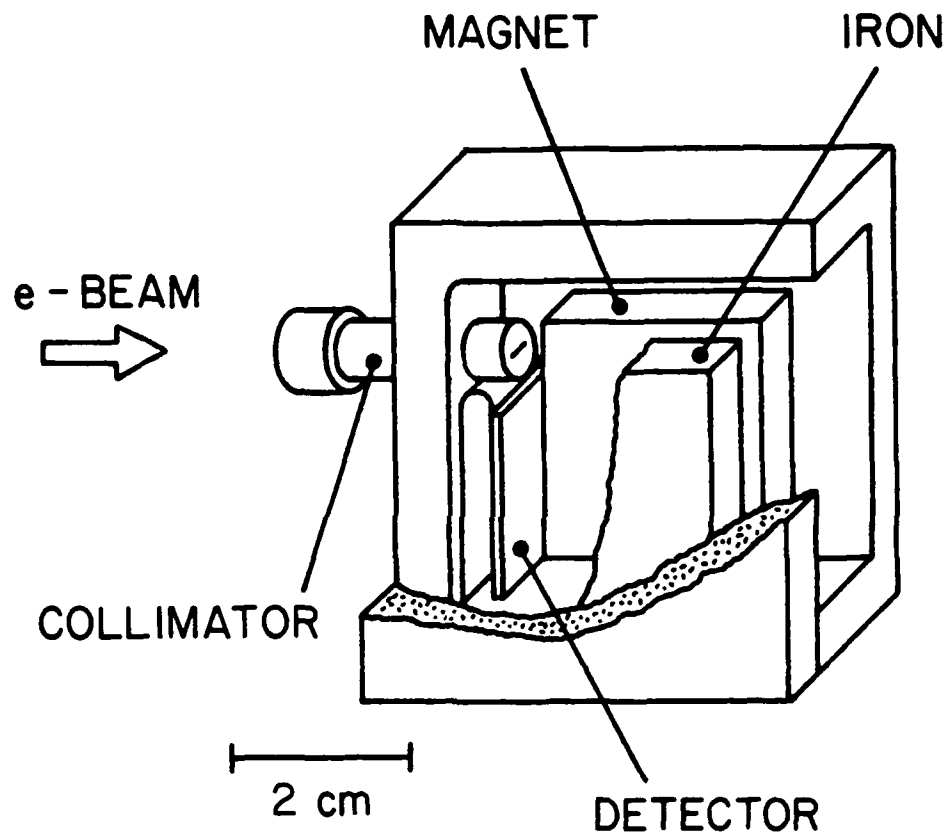


FIGURE 3-14. MAGNETIC ELECTRON ENERGY ANALYZER

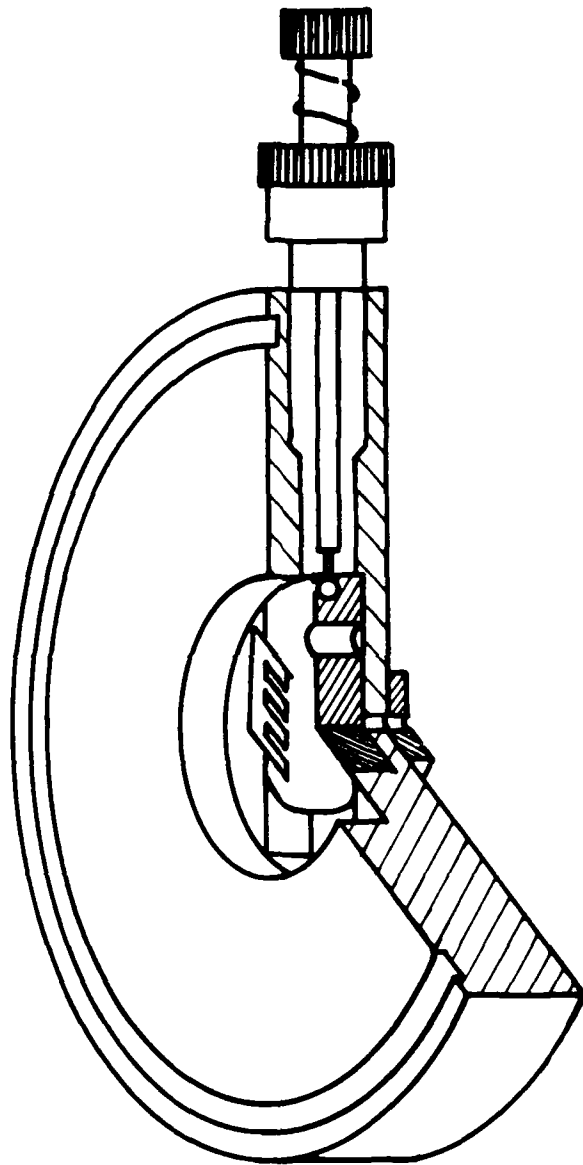


FIGURE 3-15. A SOLENOID ACTIVATED GATE VALVE

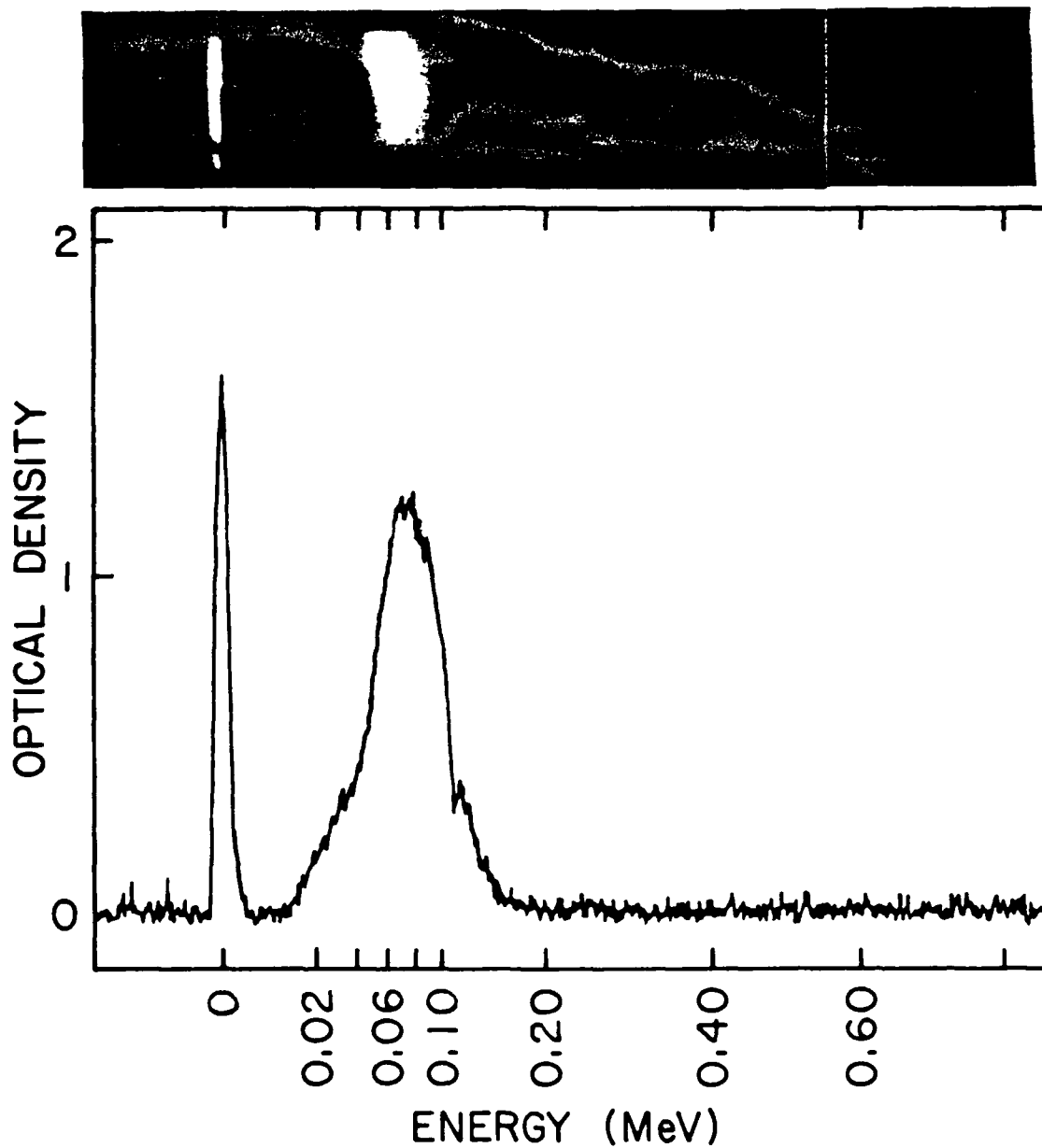


FIGURE 3-16. MICRODENSITOMETER SCAN OF PHOTOGRAPHIC FILM SHOWING THE ELECTRON ENERGY DISTRIBUTION

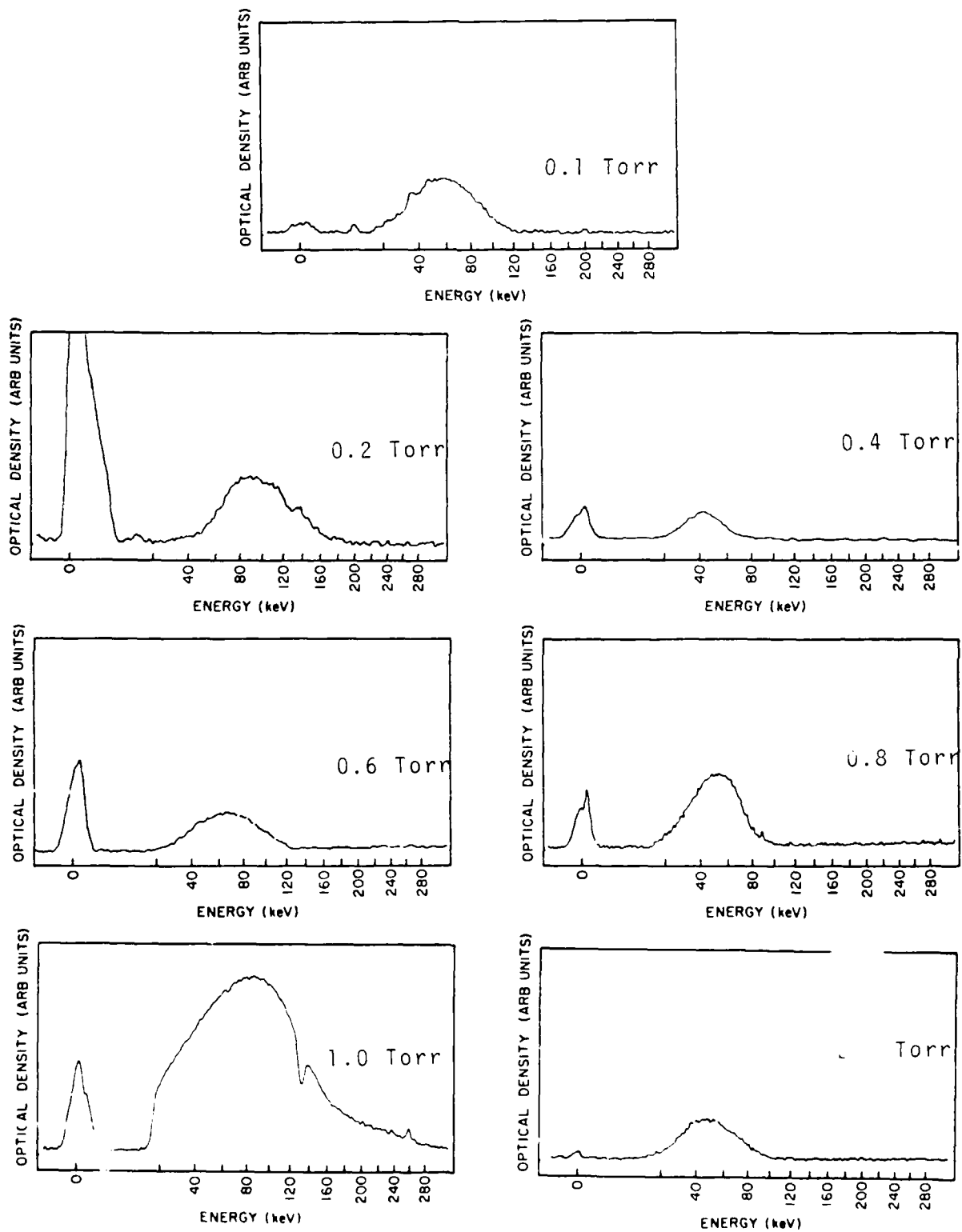


FIGURE 3-17. MICRODENSITOMETER SCAN OF PHOTOGRAPHIC FILM FOR ENERGY DISTRIBUTION OF A SERIES OF Ar SHOTS

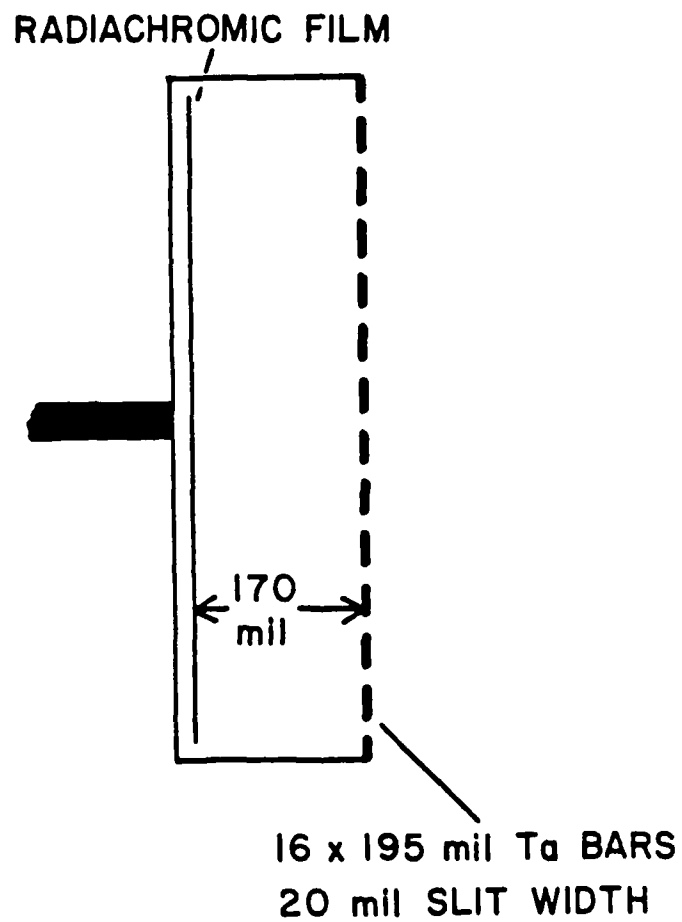


FIGURE 3-18. CROSS-SECTIONAL VIEW OF THE SLIT-PINHOLE EMITTANCE METER

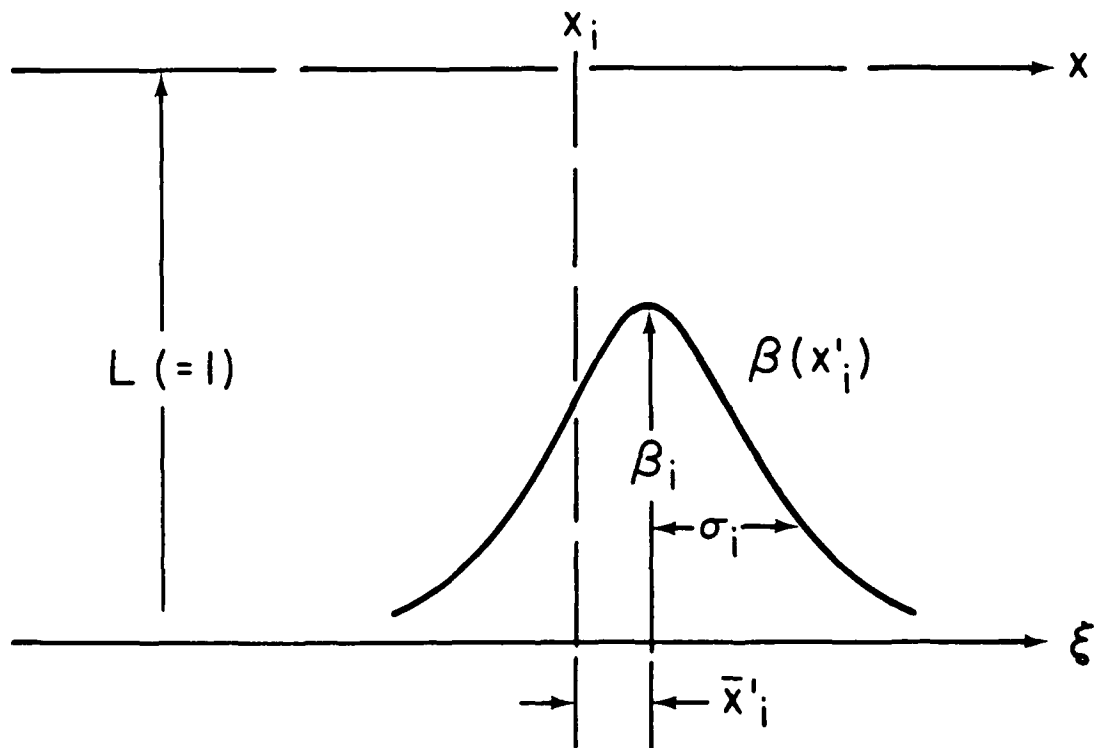
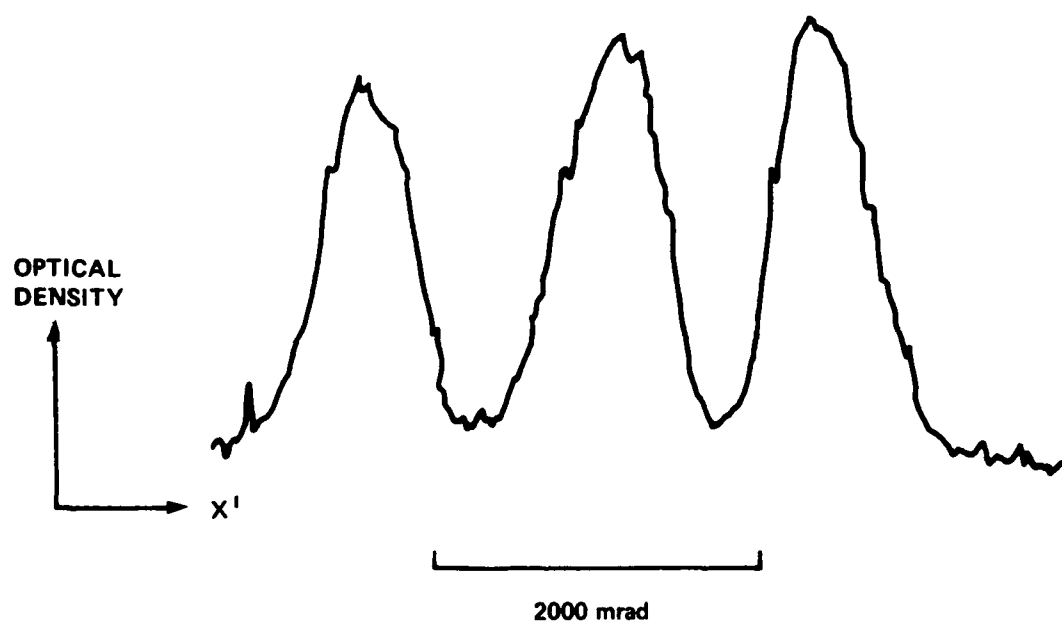


FIGURE 3-19. A TYPICAL GAUSSIAN INTENSITY PROFILE $\beta(x'_i)$ CREATED BY THE ANALYZER SLIT AT x_i . FOR $L=1$, THE MEAN DIVERGENCE ANGLE \bar{x}'_i , rms WIDTH σ_i , AND HEIGHT β_i ARE SHOWN.

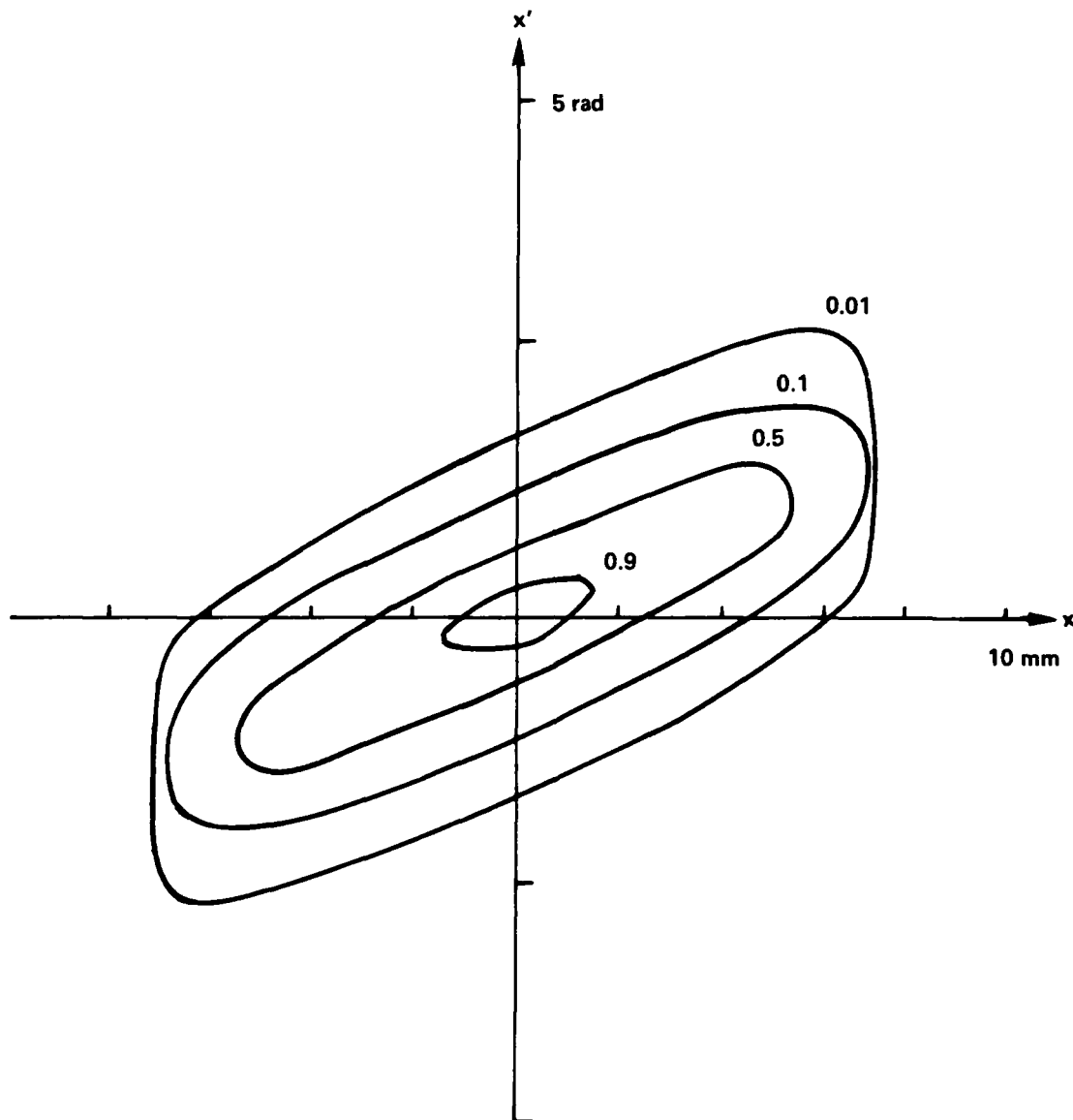
MICRODENSITOMETER SCAN OF
EMITTANCE METER RESULT



6.35 MICRON Al FOIL
750 mTORR Ar GAS
DISTANCE = 0cm FROM BEAM PORT

FIGURE 3-20. MICRODENSITOMETER SCAN OF RADIACHROMIC FILM FOR EMITTANCE ANALYSIS

CONTOURS OF CONSTANT $f_2(x, x')$



$$\epsilon_{\text{RMS}} = 8 \times 10^{-3} \text{ m} \cdot \text{rad}$$

FIGURE 3-21. $f_2(x, x')$ CONTOUR PLOT SHOWING 0.01, 0.1, 0.5, AND 0.9 CONTOURS

CHAPTER 4

ION BEAM STUDIES

ION BEAM FLUX MEASUREMENTS

The ion beam flux is measured⁸⁴ using CR-39 nuclear track detector.⁸⁵ CR-39 plastic is damaged by the passage of energetic ions as they enter the plastic. The damaged area is then typically etched out of the plastic leaving a visible track. The etching of the track progresses as shown in Figure 4-1.⁸⁶ The damaged area etches at a velocity v_d , which is more rapid than the etch rate of the undamaged plastic, v_g . The sensitivity of this detector is quite high. Protons of energies down to several keV have produced tracks in etched CR-39. Lighter ions, such as protons, tend to produce tracks with a very small damage radius whereas heavier ions will produce a larger radius of damage due to their higher atomic number, but a shallower track due to their shorter range in the plastic. This phenomenon is observed quite frequently in Thomson spectrograms which will be discussed later in this chapter.

In order to measure the flux, a copper mask is made with small holes along a radius every 7 mm. The CR-39 detector is placed immediately behind this mask and exposed to the plasma focus discharge. The CR-39 may be rotated enabling up to 12 exposures without opening the system to vacuum. After the CR-39 is exposed to the focus, it is etched in 6.25 N solution of NaOH at 70°C for 30 minutes. At this time, the damage caused by the passage of the ions through the plastic has been etched sufficiently to be barely visible. The resulting track density is much too high to enable a measurement of density under a light microscope. A Formvar replica of the track plate is taken so that scanning electron microscopy may be used.⁸⁷ The Formvar is in a 2 percent solution of ethylene dichloride so that it may be dropped onto the track plate with a dropper. The evaporation of the solvent leaves only a thin layer of Formvar covering the CR-39 and filling the etched track pits. When this layer is peeled

from the CR-39, a negative image of the tracks has been formed. These track spikes are much easier to observe under the scanning electron microscope than the corresponding track pits and enable us to count the track density very simply.

The number of ions per unit solid angle is obtained by counting the tracks per unit area on the picture, n_0 , and putting into the equation:

$$\frac{dN}{d\Omega} = n_0 M^2 (L^2 + R^2) / \cos\theta \cos\sigma_t, \quad (4-1)$$

where M = picture magnification, L = distance from focus to pinhole plate, R = radius from axis of system to pinhole, $\theta = \tan^{-1}(r/L)$, and σ_t = tilt angle of sample on scanning electron microscope stage. The flux, $\frac{dN}{d\Omega}$ is found from the above equation and plotted as a function of polar angle in Figure 4-2 for a 250 mTorr N_2 shot and a 250 mTorr H_2 shot. On this shot we differentiated between proton tracks and heavier ion impurity tracks such as nitrogen by the shape of the etched track pit. Impurities in the focus are important constituents of the ion beam especially at larger angles. This is consistent with the hypothesis that the heavier impurities because of their greater mass/charge ratio will be on the outside of the sheath as it collapses.⁸⁸ Because of larger larmor orbits, these ions may be preferentially accelerated at larger polar angles.⁴²

Integration of the $dN/d\Omega$ may be approximated by a summation (assuming axial symmetry) to estimate the total number of ions accelerated within the range tested.

$$\sum 2\pi \frac{dN}{d\Omega} \sin\theta \Delta\theta, \quad (4-2)$$

gives 1.05×10^{11} particles within a 22-degree cone for the nitrogen exposure shown in Figure 4-2.

We attempted to see some filling gas dependence by finding the track density on axis at a distance of 8.3 cm from the tip of the center electrode. 250 mTorr hydrogen, 500 mTorr helium, 250 mTorr nitrogen, and 500 mTorr Ar shots produced 1.26, 1.05, 5.39, and 1.04×10^9 tracks per cm^2 . The plasma currents

for these shots at focus were 135, 140, 145, and 150 kA, respectively. It is apparent that any pressure dependence may be overwhelmed by shot to shot variation of the focus. In addition, hydrogen results at pressures 60, 125, 250, 500, 1000, and 2000 mTorr were 1.45, 2.56, 1.26, 1.80, 0.54, and 2.14 $\times 10^9$ tracks/cm².

ION PINHOLE CAMERA ANALYSIS

A stereoscopic pinhole camera⁸⁹ is constructed in order to observe the spatial distribution of the ion source of the plasma focus device. A very important consideration in the design of such a camera is the resolution of the system. The quantities important for resolution analysis are D = pinhole diameter, O = object to pinhole distance, and L = image to pinhole distance. With these definitions, it is a simple geometrical problem to find R_c the pinhole camera resolution spot size, i.e., the distance between two objects which can just be resolved:

$$R_c = D (O/L + 1) , \quad (4-3)$$

See Figure 4-3.

The pinhole camera is constructed from two pinholes of 0.075 mm diameter on a 25 μ m thick copper foil separated by 10 mm (=P). A CR-39 detector is placed 15 mm downstream of the pinholes. When the camera is placed 75 mm from the focus, R_c is 0.3 mm. Figure 4-4 shows several pinhole pictures taken of the plasma focus at 250, 250, and 500 mTorr of Ar filling gas (top to bottom). Left and right exposures correspond to the same shot, and the figure shows the CR-39 as viewed from the exposed side.

Assuming straight trajectories from the source, stereoscopic analysis may be applied to such a double pinhole camera. The geometry is shown in Figure 4-5. For simplicity, suppose two point ion sources shown at different x and z coordinate emit uniformly over the angle subtended by the pinholes. The x -axis is defined by the line passing through both pinholes and the z -axis is defined by the line from the source to the pinhole. The separation between the

two images will, in general, be different at the left and right images, their separations being S_L and S_R , respectively. It is straightforward to find the separation of the sources in z and x coordinates, Δz and Δx ,

$$\Delta z = O^2(S_R - S_L) / LP, \quad (4-4)$$

$$\Delta x = O(S_R + S_L) / 2L. \quad (4-5)$$

We may identify some structures common to both left and right pictures in Figure 4-4 as well as their relative locations. The difficulties in this analysis are the lack of sharp detail in most of the structures identified, which typically leads to an error of +/- several millimeters, hence this stereoscopic technique may be of limited use in determining the three-dimensional ion source; however, the two-dimensional information is quite reliable.

Some interesting features of the pictures are the up to four concentric circle structures at effective source radii of 1.47, 0.92, 0.60, and 0.24 cm. In addition, at least one point source appears within the smallest radius circle. Similar structure has been observed at other laboratories⁹⁰ with no apparent explanation. It must be remembered that this is a time integrated diagnostic. The point-like source at the center may be comparable in size to the final diameter (sub-millimeter) of the pinch observed in streak or framing photographs. The larger concentric circles may be indicative of earlier ion acceleration as the cylindrically symmetric sheath is collapsing toward the axis.

THOMSON SPECTROMETER ION DIAGNOSTIC

A compact Thomson spectrometer designed by M. J. Rhee⁹¹ is used to analyze the ion beam for charge state resolved energy spectra. The Thomson spectrometer is a charge-to-mass ratio and energy analyzer based on particle deflection in parallel electric and magnetic fields. Reference 91 is a complete description

of the spectrometer and particle deflection analysis. A short synopsis will be given in this work for the sake of completeness.

The spectrometer is based on two high induction permanent magnets. A copper foil covering the magnet surface allows it to be biased to a high voltage. See Figure 4-6. In the electric field, charged particles will follow a parabolic trajectory with a net deflection angle:

$$\theta_e = \frac{Ze \int E dl}{2T}, \quad (4-6)$$

where Ze is the net charge, $\int E dl$ is the path integral of the electric field along a particle trajectory, and T is the energy. In the magnetic field, they will follow a circular trajectory with a net deflection angle which is perpendicular to the electric deflection:

$$\theta_m = \frac{Ze \int B dl}{p}, \quad (4-7)$$

where p is the ion momentum, $\int B dl$ is the integral of the magnetic field, and Au is the product of ion mass number and unit nucleon mass. The resultant pattern recorded on CR-39 nuclear track detector is a set of parabolas corresponding to each charge-to-mass ratio swept out by energy spread in the ion beam described by the well known parabola equation:

$$\theta_m^2 = \frac{Ze (\int B dl)^2 \theta_e}{Au \int E dl}, \quad (4-8)$$

The collimation for the system is provided by two pinholes. The first upstream pinhole with 1.5 mm diameter ($=D_1$) is placed 50 cm ($=L_1$) upstream of the spectrometer in a fast (ms) gate valve which maintains vacuum in the spectrometer region. The second pinhole of 10 μ m micrometer diameter ($=D_2$) is just downstream of the field region. The CR-39 detector is placed 5 mm ($=L_2$) downstream of the second pinhole. The resolution of such a system, and Thomson spectrometers in general, is described in Appendix B.

The calibration of the magnetic field integral is done with an Am^{241} alpha particle source. The collimated beam is passed through a collimation system with and without the magnetic field. The value of $\int B dl$ is found to be 6.06×10^{-3} T-m. Direct measurements with a Hall probe agree to within 1.5 percent. The integral of electric field is found by reduction from Thomson spectrograms of known ion species, $\int E dl = 1.25 \text{ EL}$, where EL is the electric field times the length for the ideal parallel plate capacitor.

A typical spectrogram is shown in Figure 4-7. For this spectrogram $\int E dl = 22.4 \text{ kV}$. Some interesting features to note are the reference B- axis which is made by exposing the spectrometer without applying an electric field. In addition, there always exists a spot at the origin of the Thomson spectrometer coordinates. This is due to the undeflected passage of particles through both pinholes as would be expected of neutrals.

Also note that due to the polepieces, there is a finite acceptance angle which is determined by the aspect ratio of the gap, 0.270 rad. The identification of ion species depends on the assumption that all charge states below the one in question exist and extend to a constant velocity line. The charge state is found simply by counting the equally space intersections of parabolas with this constant velocity line. The mass is found from known charge and charge-to-mass ratio.

The energy spectrum may be obtained by directly counting the particle tracks in CR-39. Each parabola may be divided into small segments $\Delta\theta_i$ of constant electric deflection angle which correspond to a certain ΔE_i . The number of tracks in each segment, $\Delta N_i / \Delta\theta_i$, are counted and the spectrum is found from the equation:

$$\frac{dN}{dE} = \frac{\Delta N_i}{\Delta\theta_i} \frac{\Delta\theta_i}{\Delta E_i} \quad (4-9)$$

The energy spectra of the ion species obtained are shown in Figures 4-8 through 4-12. The energy uncertainty is discussed in Appendix B.

One major disadvantage of the Thomson spectrometer system is that the collimation system by its double pinhole nature selects only a small solid angle of the ion beam. For example, one could imagine the second downstream pinhole selects only a portion of the image formed by the upstream pinhole. However in all cases measured, we have taken the best spectrogram from a sample of 10 or more. Another disadvantage of the Thomson spectrometer is that it is not sensitive to the high-energy tail observed at many laboratories.

NEUTRAL PARTICLES

The presence of neutral particles is investigated. This study⁹² was motivated by the observation that more than 10^8 particles travel through the hollow center electrode in the electron beam geometry. A piece of CR-39 was placed several cm from the beam port, and while the electron beam proved very unstable and often missed the piece of CR-39, there was a consistent production of tracks on the CR-39 in a sharp disc as if the beam was well collimated. As a matter of fact, the tracks behaved as if the beam was collimated by the acceptance of the hollow center electrode. Preliminary evidence by magnetic deflection indicates that the ions have a greater proportion of neutrals than the forward ions, a phenomena observed by the Stevens group also.⁹³ Typically in the forward direction there are 20-30 percent neutrals.

EMITTANCE OF ION BEAM

A slit-pinhole emittance meter is used to determine the rms emittance of the plasma focus produced ion beam. The meter is similar to the one used for the electron beam emittance. In this case, six slits are $20\mu\text{m}$ in width, constructed from stainless razor edge blades. The separation between slits is $9.50\text{ mm} \pm 0.05\text{ mm}$. A CR-39 nuclear track detector is placed 8.36 mm downstream of the slits. The emittance meter is placed 50 cm downstream of the focus. Due to the wide ion beam dispersion, we define a useful beam solid angle by placing a 1.74 cm diameter diaphragm 22.5 cm downstream of the focus which defines a solid angle $\int 2\pi \sin\theta d\theta = 0.0047\text{ sr}$ (or a 2.2-degree cone). Subsequent to exposure of the meter to the beam produced by a 1 Torr Ar gas shot with plasma current of 190 kA, the CR-39 is etched for 1 hour in 6.25 N NaOH at

70°C. The sample is then placed on a microscope stage with an attached dial gauge for measurements to 0.01 mm precision. A 50x50 sq. μm area on the trackplate defines the pinhole size. The number of particle tracks within this area (pinhole) are counted and plotted as a function of tsi in Figure 4-13. These six individual peaks are fit to a Gaussian function to find their mean widths. It was found that to within a very slight variation, the widths (σ) are constant as would be expected from a cold beam with a source of finite spatial extent. The peak values of the distribution are fit to a Gaussian function to find the mean overall beam width, and the beam divergence is found as explained in Chapter 3. The empirical values are $\sigma_0 = 69.7$ mrad, $b = 19.9$ mm, and $\alpha = r/0.217$. Figure 4-14 is a two-dimensional contour plot of f_2 . The rms emittance is calculated from Equations (3-23) through (3-25) and found to be $4b\sigma_0$ for a distribution described by the equations:

$$\alpha(r) = r/a, \beta(r) = \beta_0 e^{-r^2/2b^2}, \sigma(r) = \sigma_0. \quad (4-10)$$

Hence the rms emittance is found to be 5546 mm-mrad.

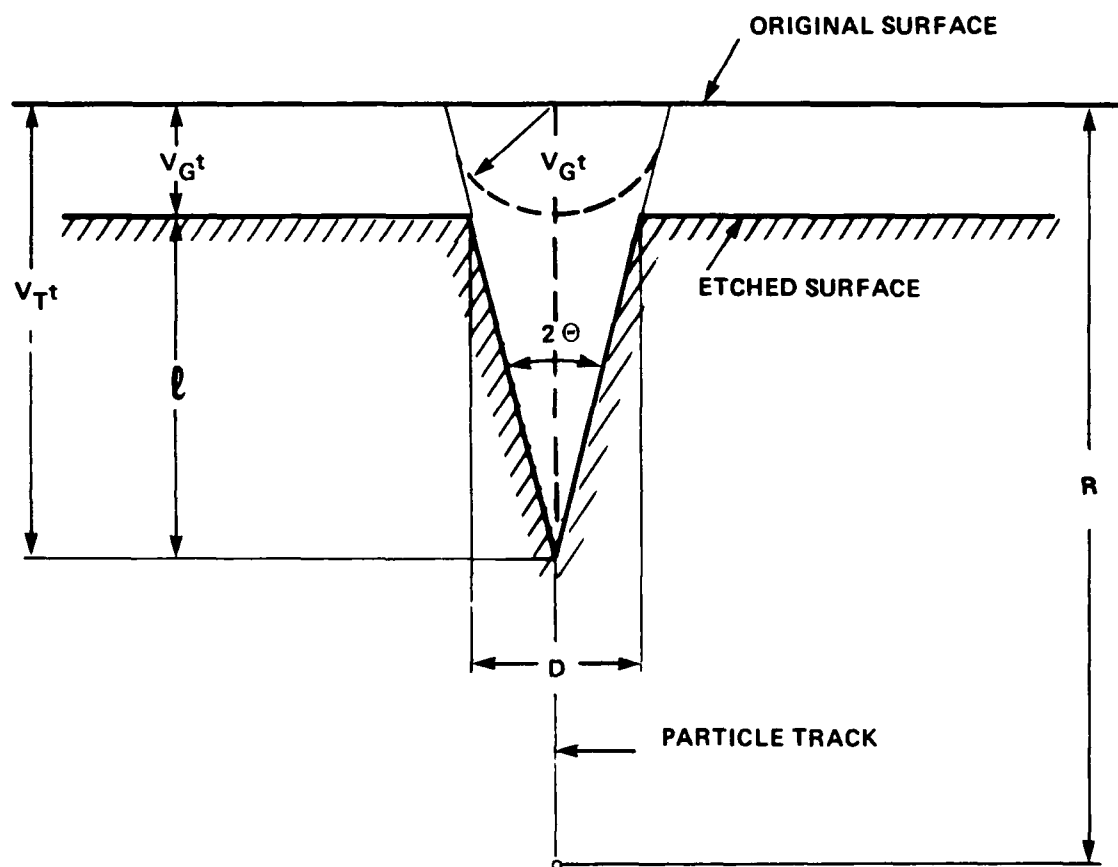


FIGURE 4-1. TRACK PIT ETCHING. PATHS OF ION THROUGH THE PLASTIC WILL ETCH AT A LARGER VELOCITY, v_T , THAN BULK ETCH, v_G .

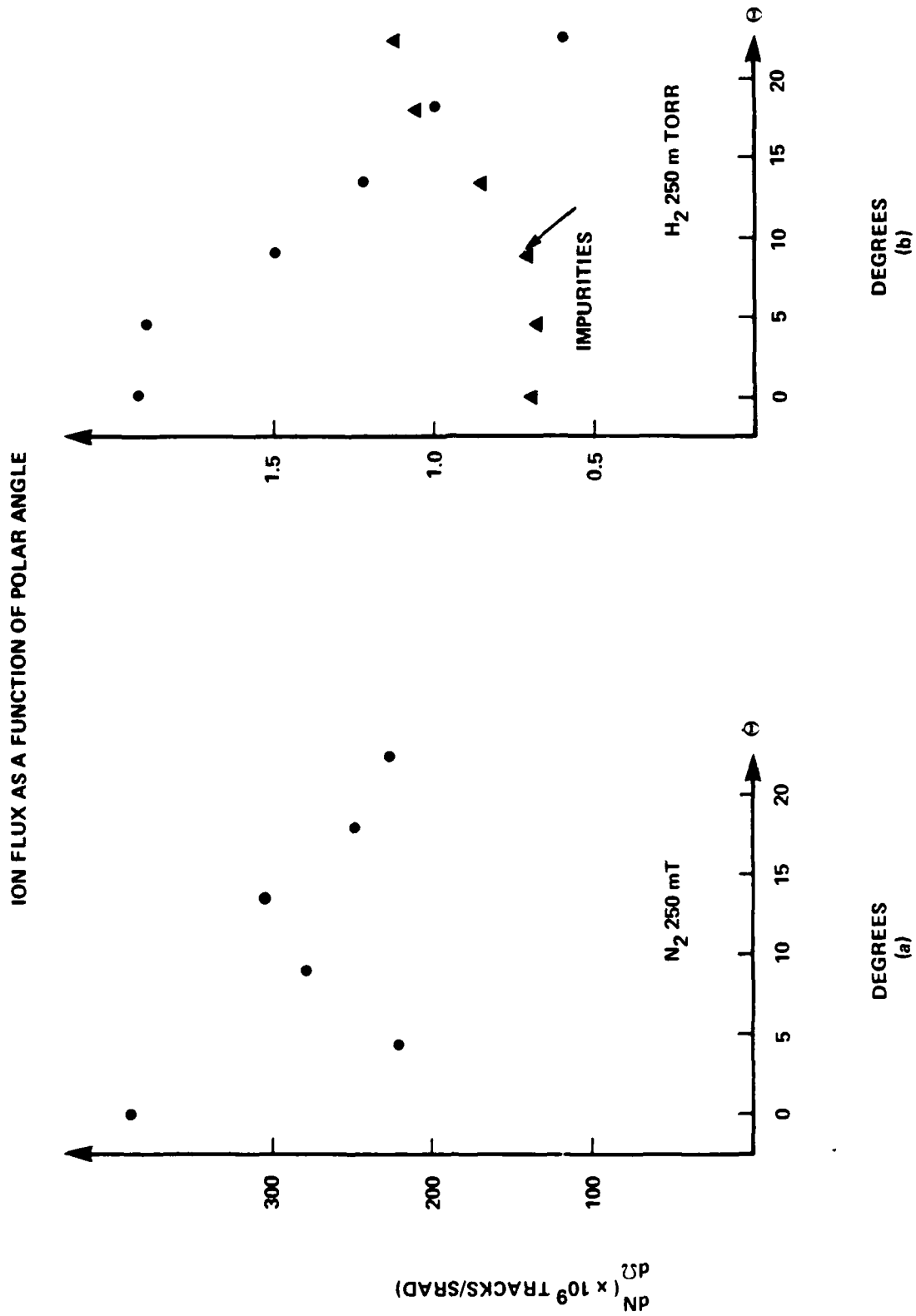


FIGURE 4-2. ION FLUX DISTRIBUTION AS A FUNCTION OF POLAR ANGLE

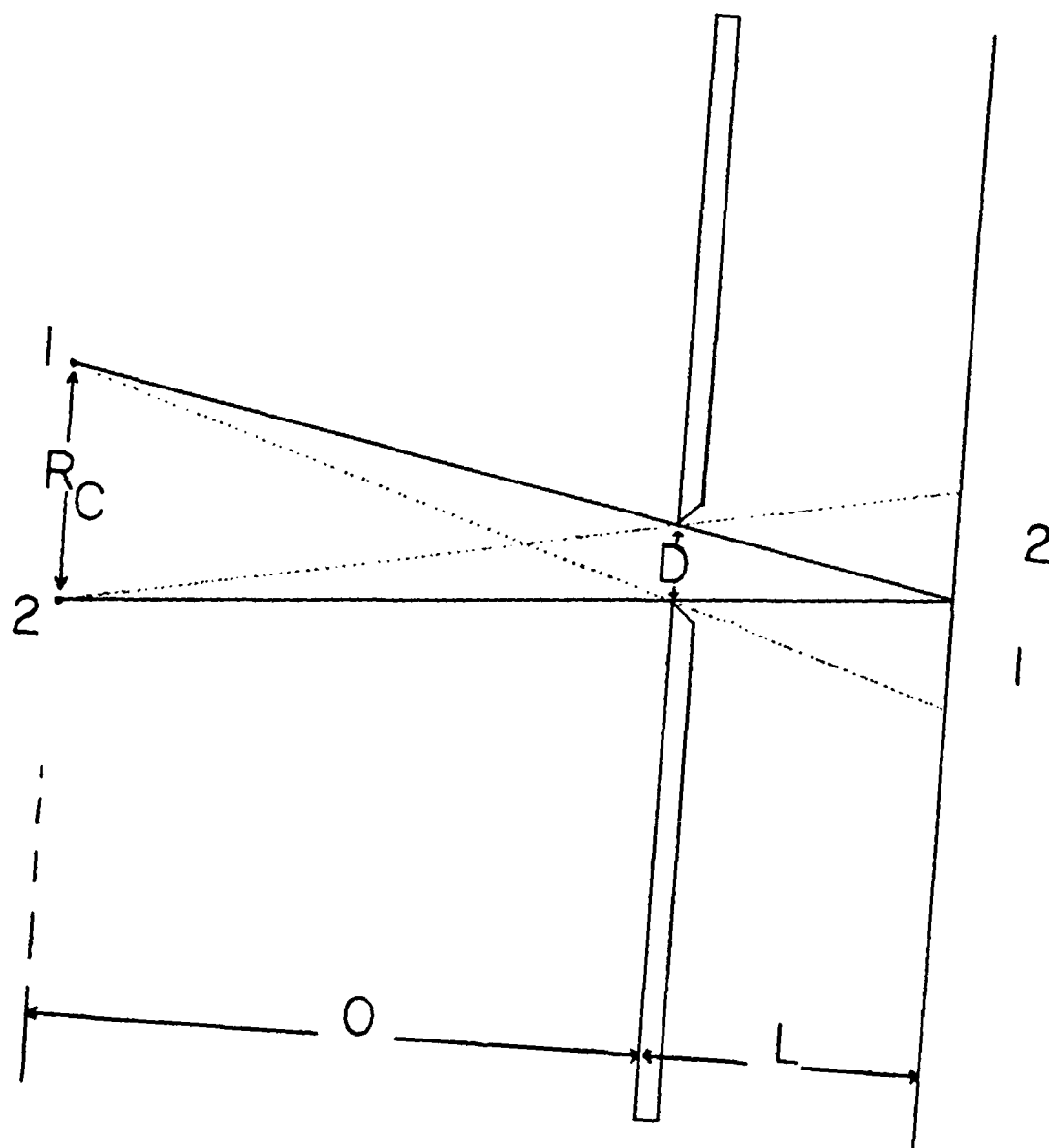


FIGURE 4-3. RESOLUTION OF THE PINHOLE CAMERA. R_C IS THE SEPARATION OF TWO OBJECTS WHICH CAN JUST BE RESOLVED ON THE DETECTOR.

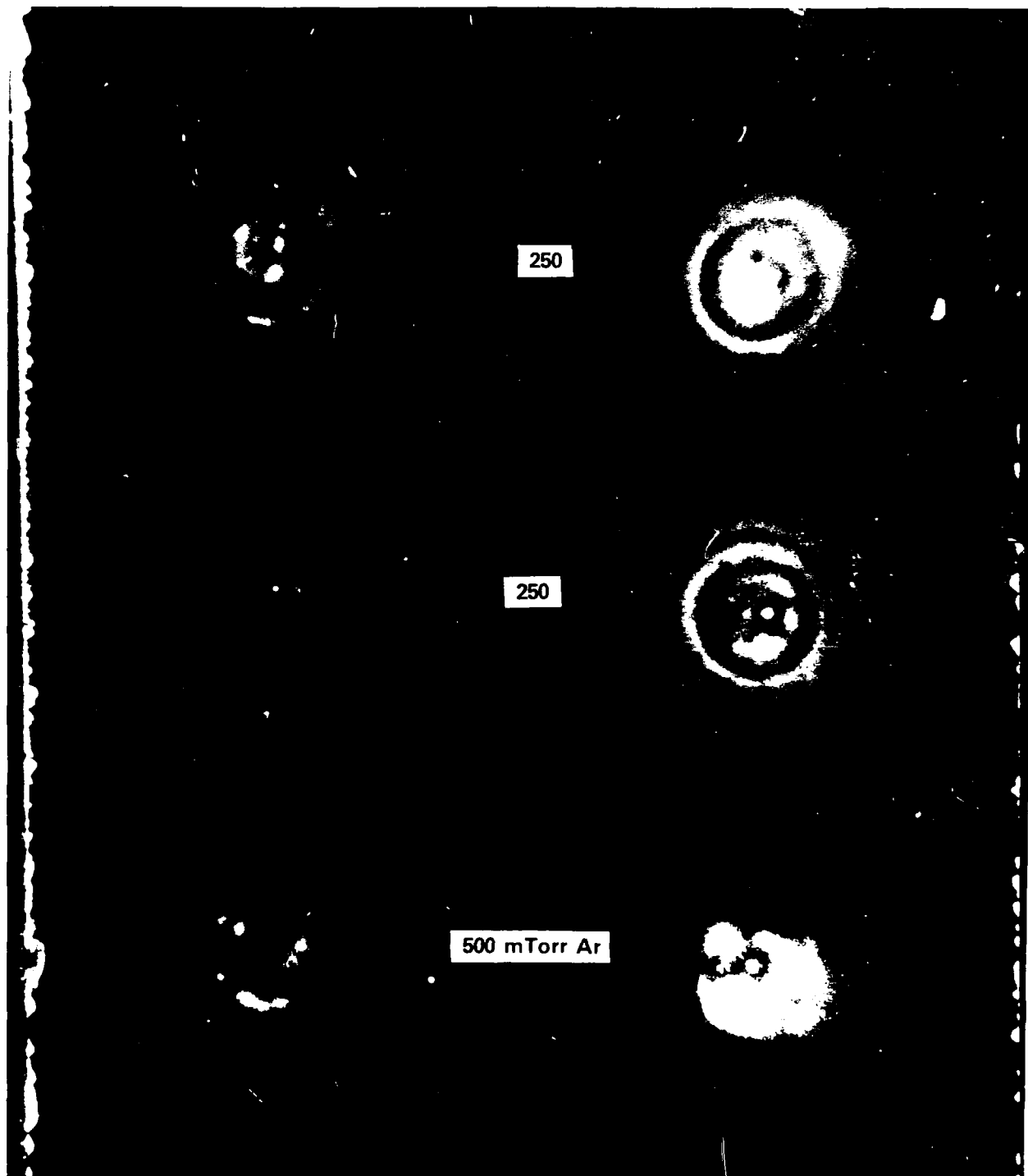


FIGURE 4-4. PINHOLE PICTURES OF 250, 250, AND 500 mTorr Ar SHOTS

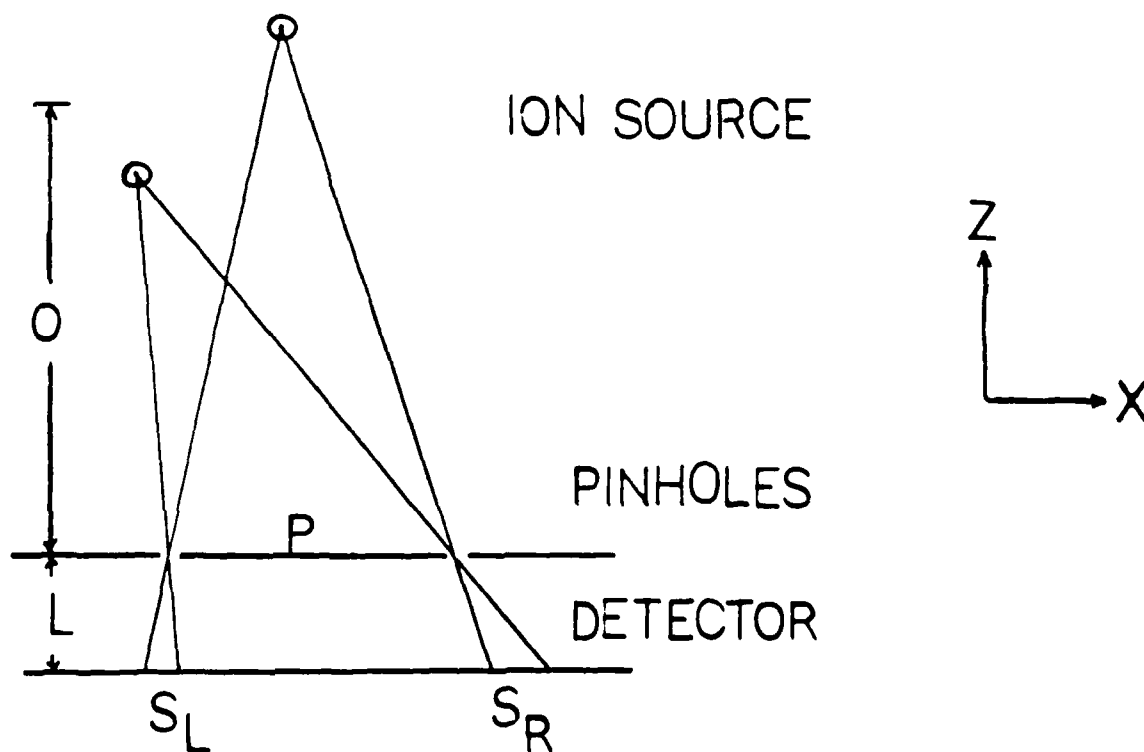


FIGURE 4-5. STEREOSCOPIC ANALYSIS OF TWO ION SOURCES. THEIR SEPARATIONS IN X AND Z COORDINATES DEPEND ON THE SEPARATIONS S_R AND S_L .

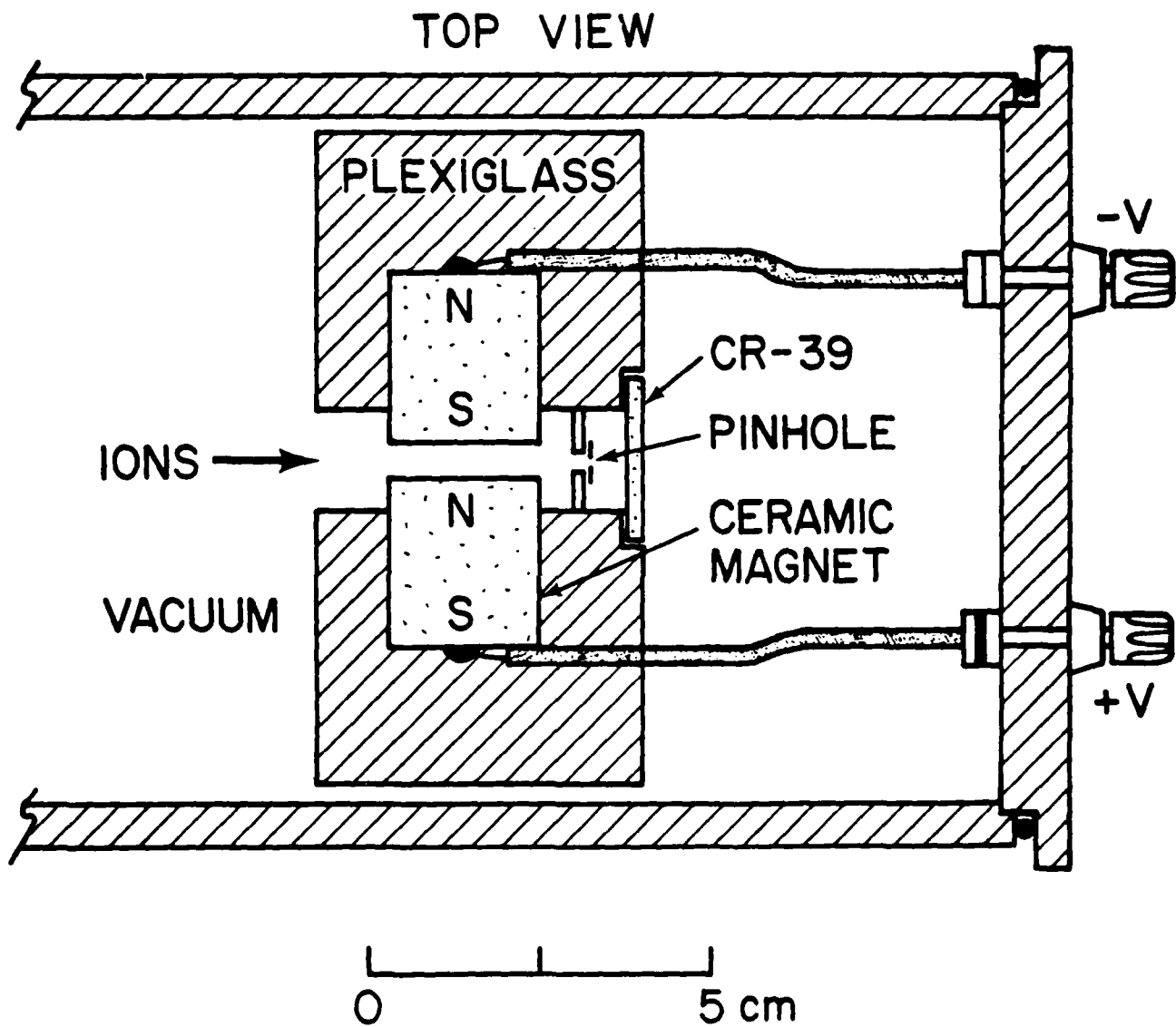
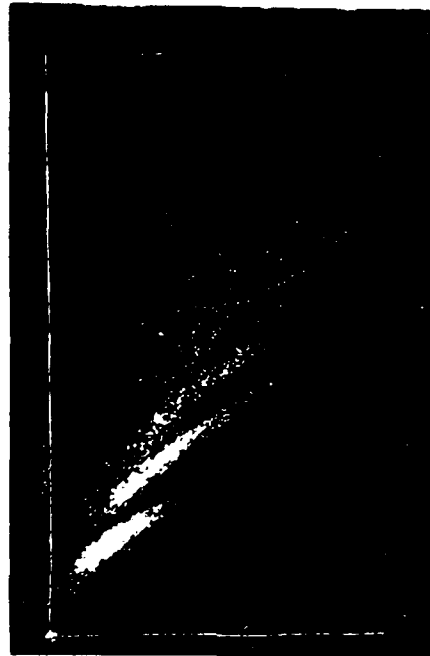


FIGURE 4-6. THE COMPACT THOMSON SPECTROMETER

THOMSON SPECTROGRAM OF
ARGON SHOT

MAGNETIC DEFLECTION



Ar⁺⁺⁺

Ar⁺⁺

Ar⁺

ELECTRIC DEFLECTION



0mm
0mrad

0.5mm
100 mrad

FIGURE 4-7. AN EXAMPLE OF A TYPICAL Ar RESULT FROM THE SPECTROMETER

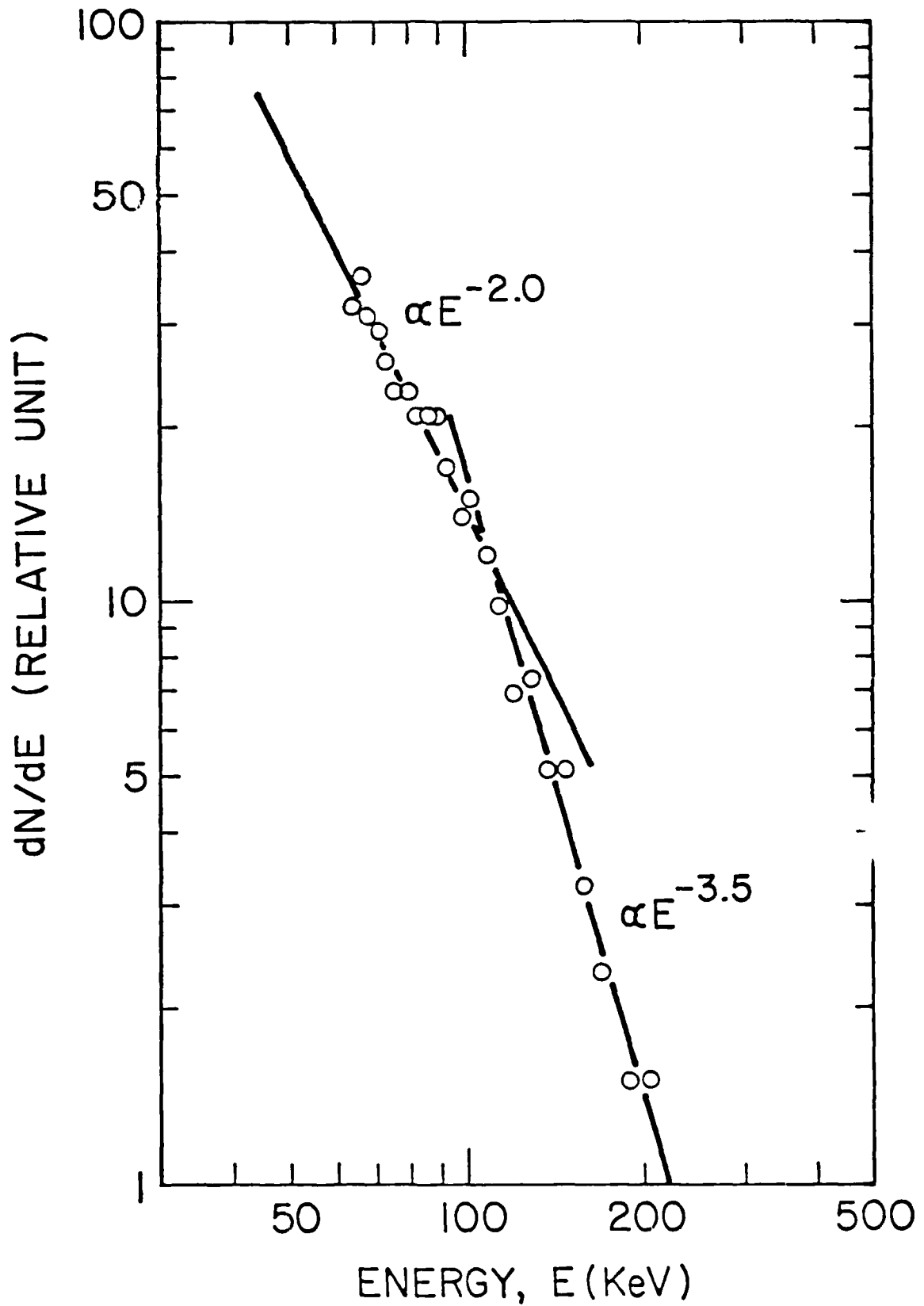


FIGURE 4-8. ENERGY SPECTRA FOR H IONS

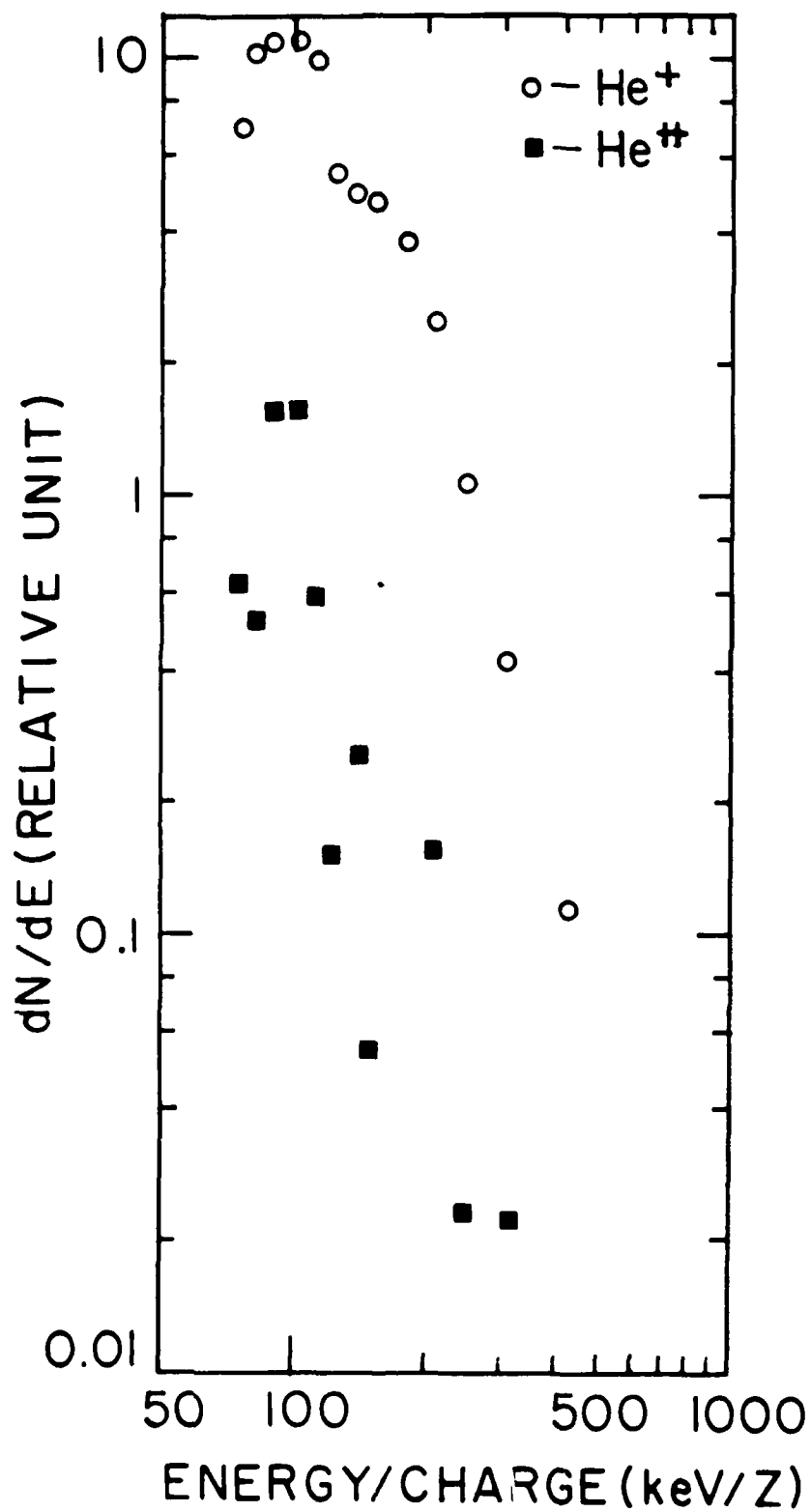


FIGURE 4-9. ENERGY SPECTRA FOR He IONS

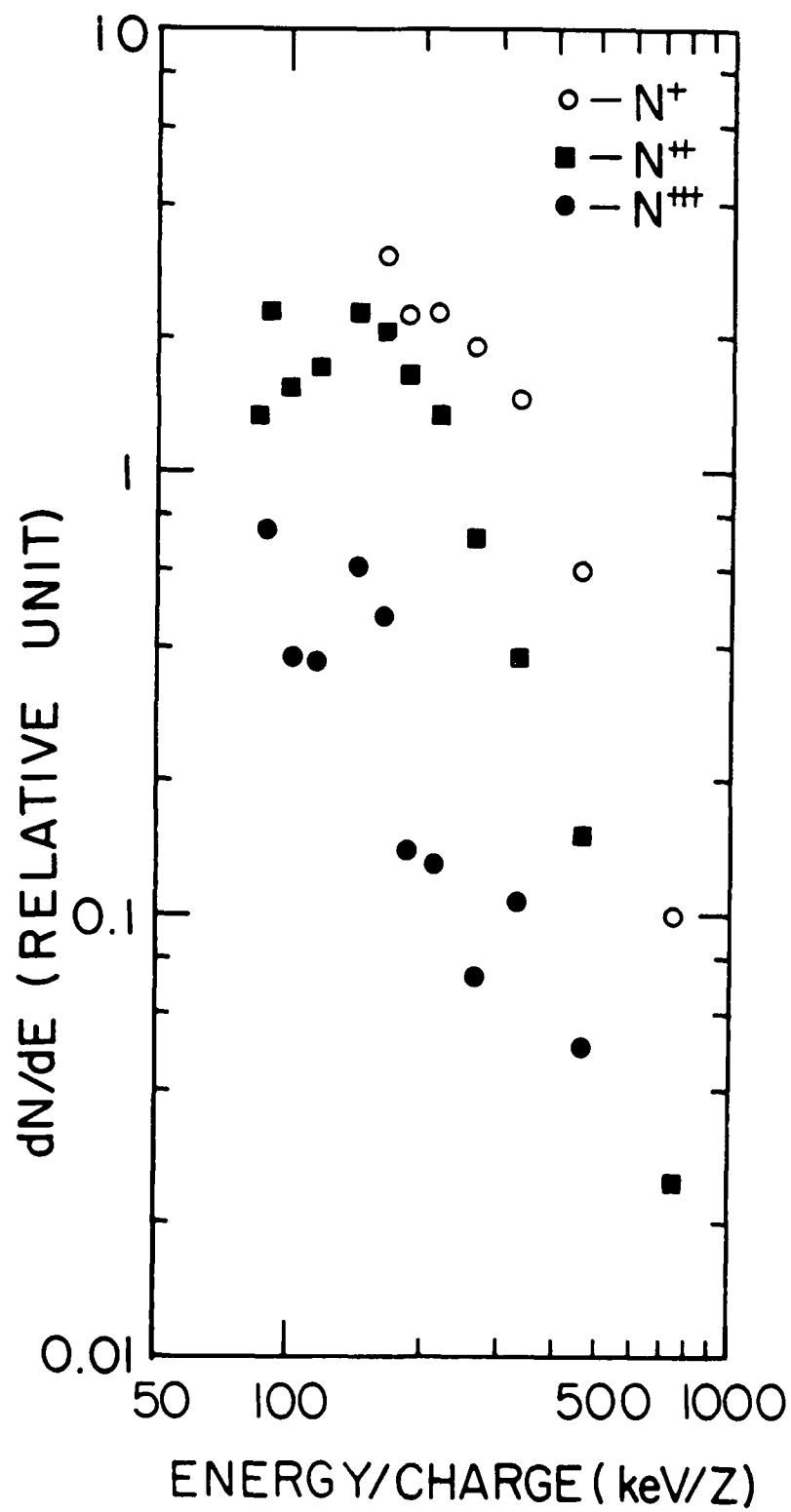


FIGURE 4-10. ENERGY SPECTRA FOR N IONS

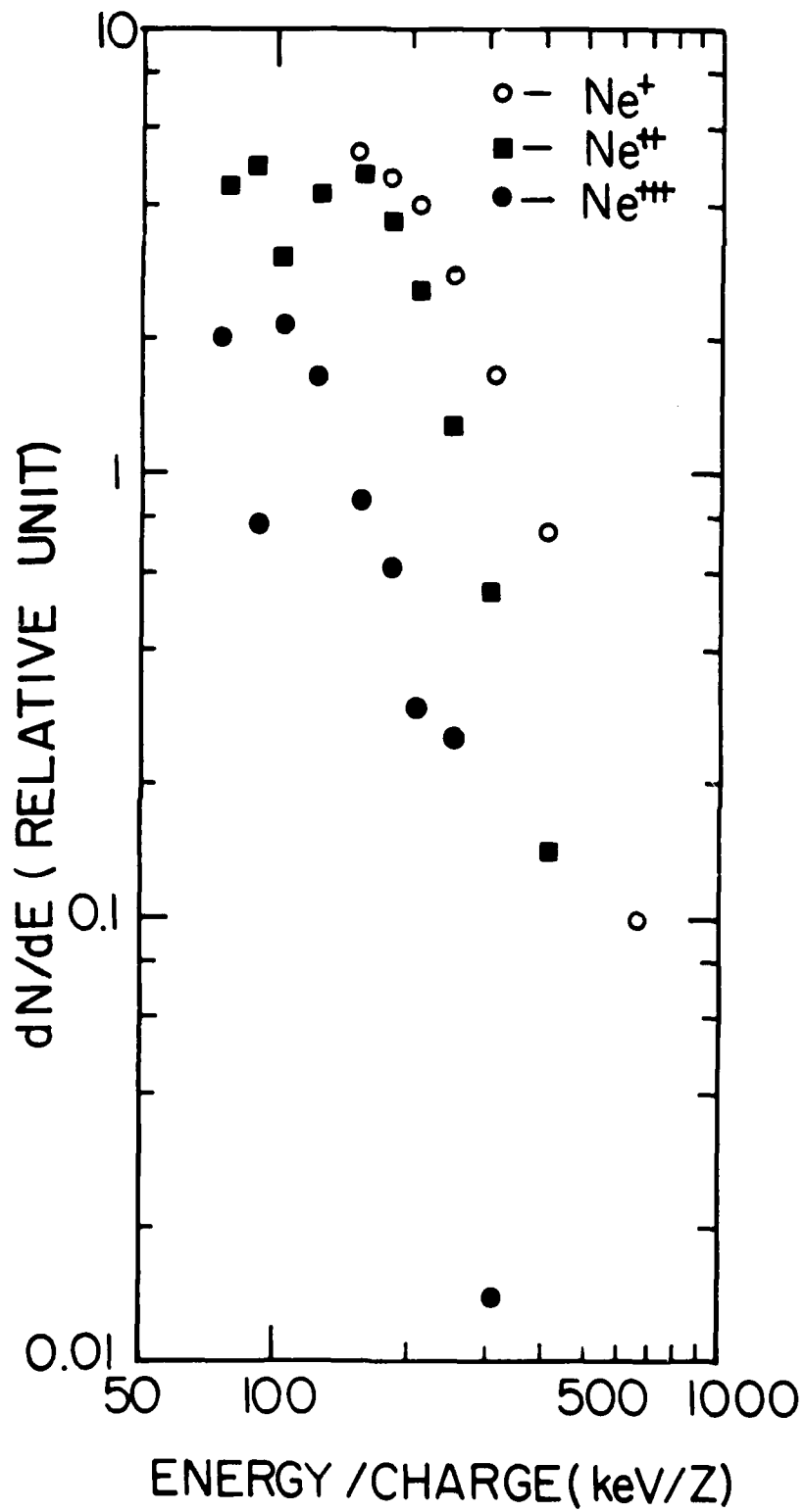


FIGURE 4-11. ENERGY SPECTRA FOR Ne IONS

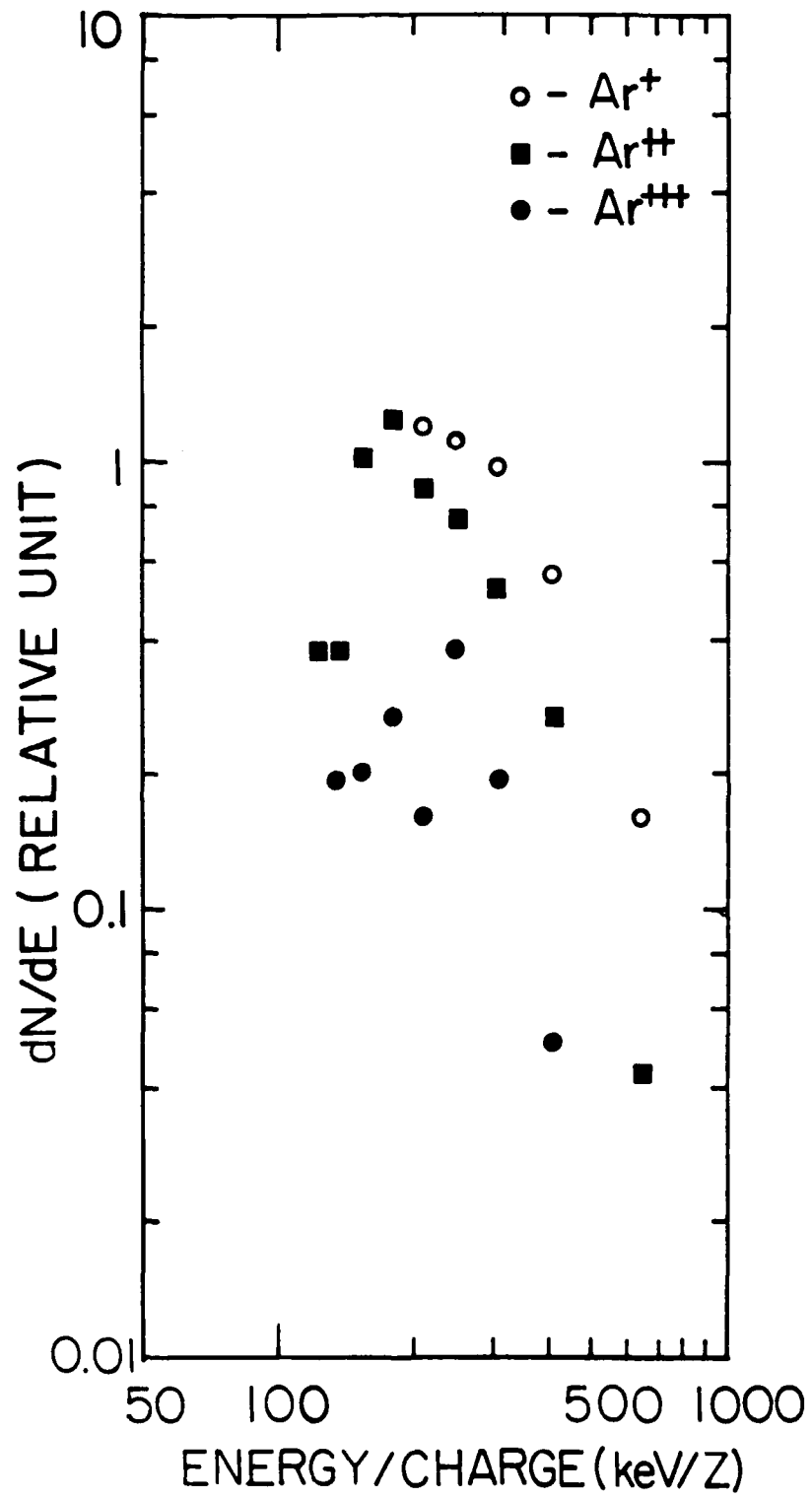


FIGURE 4-12. ENERGY SPECTRA FOR Ar IONS

ION BEAM EMITTANCE DATA

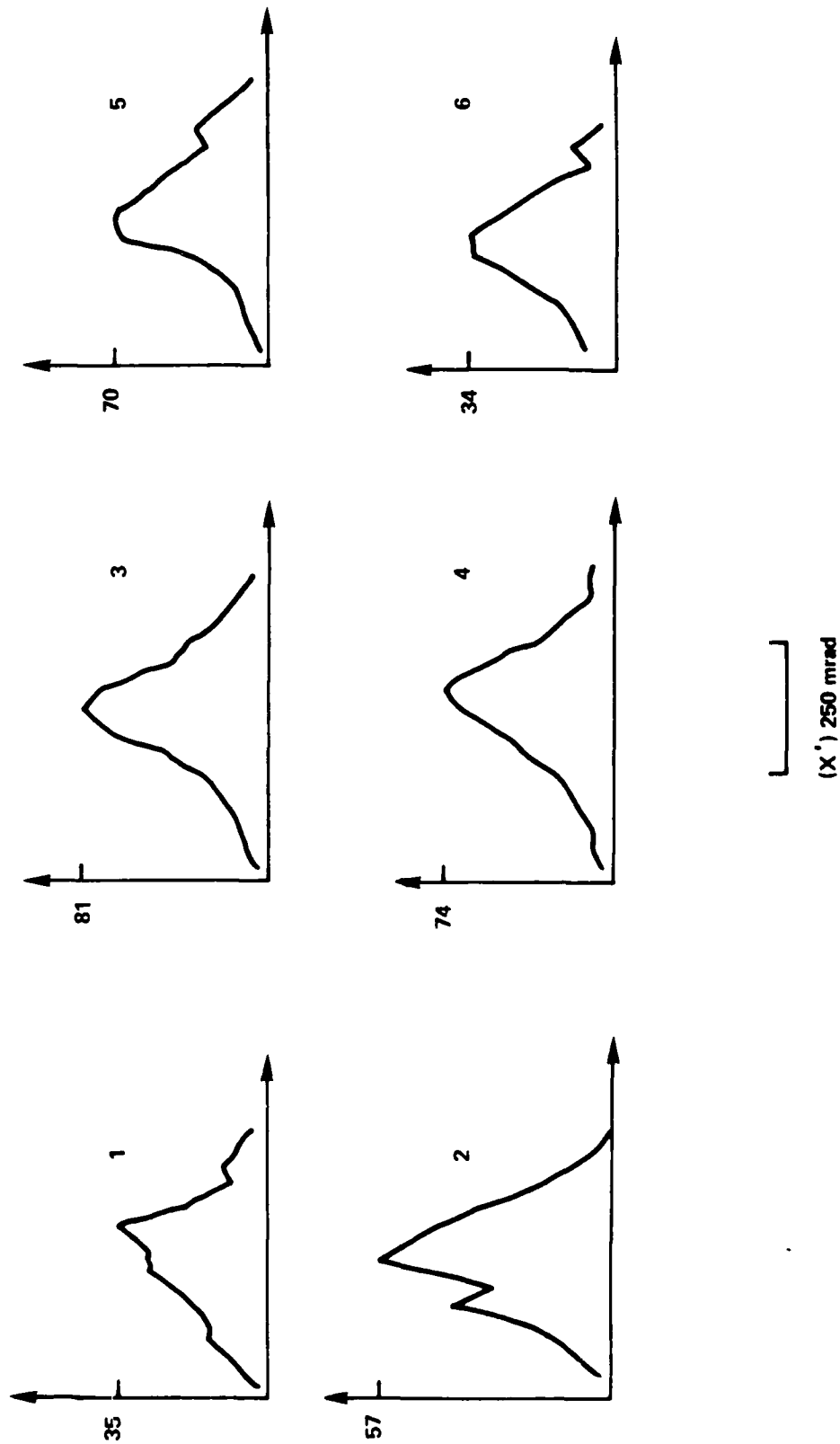


FIGURE 4-13. ION TRACK DISTRIBUTIONS FOR EMITTANCE ANALYSIS

CONTOURS OF CONSTANT $F_2(x, x')$

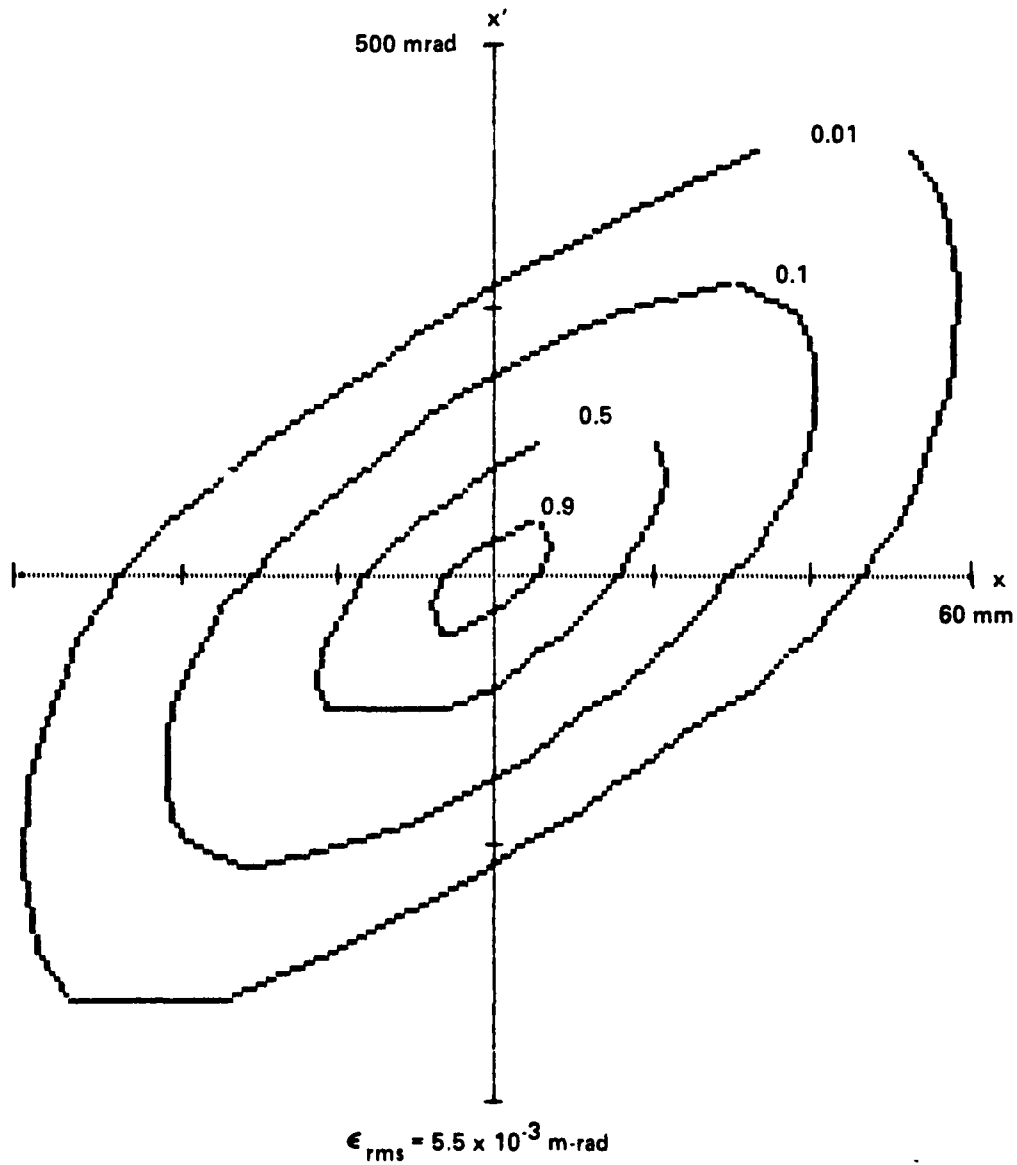


FIGURE 4-14. $f_2(x, x')$ CONTOUR PLOT SHOWING 0.01, 0.1, 0.5, AND 0.9 CONTOURS

CHAPTER 5

ANALYSIS OF EXPERIMENTAL RESULTS

NONREPRODUCIBILITY

The nonreproducibility of the plasma focus device is a common problem with most pulsed power systems. The performance of the plasma diode depends on the performance of a plasma instability which may, by its nature, be very sensitive to system parameters such as: impurity gases which have leaked into the system; electrode contamination with pump oil; asymmetries in the electrodes and/or insulators; etc., which may vary randomly on a shot-to-shot basis. These considerations constrained us to use single shot diagnostics which showed a wide variation of results.

The electron beam current measured by the Rogowski coil showed wide variations of approximately 2 kA at lower pressures (less than 0.2 Torr) of the filling gas. At the higher pressures the results were more consistently lower. The Faraday cup measurements after the foil were somewhat erratic with many shots (60 percent) showing null result. This was apparently due to the poor beam propagation in the short 2 cm length of 10 cm diameter drift tube before the foil. In fact, in many experiments the beam damaged the brass plate which separated the electron beam gun from the 10 cm tube indicating the beam made a 180-degree turn. It may be of use to note that the steady state space charge limiting current for a 100 keV electron beam in an infinite tube of this diameter is:

$$17 (\gamma^{2/3} - 1)^{3/2} / [(1 + 2 \ln(r_w/r_b))(1 - f_e)] \text{ (kA)} \quad (5-1)$$

Where r_b is the beam radius, r_w is the drift tube radius and f_e is the fractional charge neutralization. This value is less than 0.2 kA for our geometry and beam energy when f_e is 0. The electron spectrometer results showed

at least as wide a variation since, in addition to the short length of 10 cm tube, only a small fraction of the electron beam was selected by a 1/16-inch diameter pinhole. Many shots showed no phosphor light while some showed quite good results for the same parameters. In addition, the collimator slits became clogged with graphite over a period of time which required cleaning.

The Thomson spectrometer diagnostic also showed a wide range of results. This was explained in Chapter 4 as being due to the nature of the two slit collimation system which selects out only a small portion of the ion beam. It should also be mentioned that there were series of shots that showed no current drop or voltage signal with no explanation readily apparent. This would quite often fix itself the next day or when a new insulator was placed in the device. This was characteristic of the ion geometry more often than the electron gun geometry. This behavior may be attributed to the conditioning of the insulator or electrodes as discussed in Chapter 2 and is different from the shot to shot variation.

ANALYSIS

From a nitrogen parabola and the ion flux measurement, an estimate of the total ion current can be made. In the parabola analyzed, there are 1436 N^+ , 870 N^{++} , and 216 N^{+3} ions. This gives an average charge of 1.52 neglecting neutrals. It should be emphasized that this may lead to an underestimate of the total current since ions have undergone charge exchange or recombination as they pass through a dense plasma and a neutral gas after acceleration. Current is approximated by (total number of ions) times (average charge per ion) times e divided by (the pulse width). If the pulse width is estimated to be the same as the electron beam width 4 ns, the net ion current is 6.4 amps, whereas a typical electron current for this pressure range in N_2 is 2 kA. It is readily apparent that the ion/electron current ratio is approximately $\sqrt{(m_e/M_i)}$ and that ion current is not enhanced appreciably in this diode. However, if the charge exchange or recombination processes are included in the above estimate, it may be found that the ion current is enhanced.

Many Thomson spectrograms, similar to the one shown in Figure 5-1, reveal a constant peak electric deflection angle for two or more parabolas.⁹⁴ This is attributed to the diode like accelerating electric field which results in a constant peak energy per charge or electric deflection as is readily apparent from Equation (4-6). Unfortunately, this fact is not clear in most spectrograms which seem to show a constant peak velocity. This constant velocity line, however, may be attributed to the phenomena of charge exchange or recombination which may occur as the ions traverse a high density plasma and a neutral gas. The manner in which this occurs is illustrated in the schematic spectrogram shown in Figure 5-2. All of the ions may be initially accelerated to a constant energy per charge indicated by the vertical line. As the charge of the peak energy ions is lowered by some process, they will be recorded on the next lower parabola with the charge reduced by one but with the same mass, along a constant velocity line. In this way ions which are accelerated while they are in a higher charge state by the diode accelerating voltage may obtain a higher energy per charge by the time they reach the spectrometer. This is probably the source of the Mev per charge ions recorded on some spectrograms. Note that in Figure 4-8, the peak proton energy is about 200 keV which is comparable to the peak electron energy and also the transmission line voltage probe peak voltage.

COMPARISONS

Table 5-1 shows results of experiments done at other laboratories in the past 15 years on the charged particle beams produced by a plasma focus. Also Figure 5-3 (due to Stygar²¹) shows the scaling law for electron beam current versus bank current for plasma focus devices along with the result from this experiment. In the case of Reference 21, the diagnostic was similar to the one in this work. The lack of agreement is perhaps an indication of the fact that the experiments performed in this work involve a different filling gas pressure regime which may be more favorable to beam production.

TABLE 5-1. COMPARISON OF MAJOR CHARGED PARTICLE BEAM RESULTS

LAB	DEVICE	PARTICLE	DIAGNOSTIC	ENERGY (keV)	NUMBER
Livermore	900kA, 2TorrD	d	nucl.act.	>330	10^{17}
	800kA 1TorrD	e	x-ray	ave=150	1.2kJ
Darmstadt	220kA 4TorrD	d	magn.spect.	80-400	?
	220kA 8TorrH	e	x-ray	100	?
Stutt.	520kA 1-10TD/Ar	d,C,N,O	Thomson	>350	?
Illinois	560kA 3TorrD	d	TOF/F.Cup	25-1k	10^{17}
		e	Rogowski magn.defl.	10-400	17kA
Stevens	5-800kA 3-5T D	d	TOF/damage	300	10^{16}
		e	Rog./dendrites	300	5kA
NASA	1MA 5TorrD	e	x-ray F.cup	<500	10kA
This Work	200kA .1-2T	p,C,N, He,Ar	Thomson	20-2k	10^{11}
		e	F.cup/Rog. magn.spect.	20-300	0.5-8 kA

CONCLUSIONS

A physical model for the plasma focus device was investigated. The diode model, or stationary electric field model of the plasma focus, has been supported to the greatest extent by the Thomson spectrometer diagnostic. More support for the diode model arises from the fact that the transmission line voltage probe is in agreement with both the electron spectrometer and Thomson spectrometer peak energies. These diagnostics, however, are relatively insensitive to the high energy tail of both electron and ion beams which is observed at many laboratories. The yield of this tail is several orders of magnitude below the yield in the range investigated here. It is possible that the origin of these particles may be different.

Several new diagnostics were created for this experiment. A compact magnetic electron energy analyzer was used to determine the energy of the electron beam in the plasma focus device. The resolution and trajectory analysis for this diagnostic was performed showing the resolution to be better than 2 percent at the lowest energy range. The observed electronic energies ranged up to and above 200 keV in a device with charging voltages of 10 to 20 kV, a better than 10:1 stepup. In addition, the total e-beam energy was measured and found to be a few tens of Joules with an efficiency of approximately 1 percent. The quality of the plasma focus produced electron beam was investigated for the first time in this work. The electron beam rms emittance is found at the exit of the center electrode drift tube. This may be the place where the beam may be extracted for any application.

The Thomson spectrometer was used to obtain the energy spectra of five different filling gas ions. In addition, the Thomson spectrometer was discussed and the resolution analysis performed. It is hypothesized that charge exchange and/or recombination is responsible for the presence of neutral particles appearing at the origin of the Thomson parabola, as well as the presence of a constant velocity line at the peak energies in many parabolas. The ion beam flux is measured with a CR-39 nuclear track detector and found to be much lower than observed by other researchers in devices of slightly higher currents. An estimate of the flux was also made with the results of the ion emittance meter

and was found to be consistent with the result of the fluxmeter. The ion beam rms emittance is investigated.

This work is a comprehensive evaluation of the beam behavior of the plasma focus produced particle beams. In the future, emphasis should be placed on the use of time resolved diagnostics which may yield much more information about the nature of particle acceleration. In particular, time resolved energy measurements of the electron and ion beams should be possible through the use of new, highly sensitive, streak camera systems.⁹⁵ In conjunction with a memory video camera, this system may have a large impact on data acquisition.

The instabilities that occur in the plasma focus subsequent to the $m=0$ are not yet understood. The presence of microinstabilities is not yet well documented. Future investigations should be placed on the understanding and controlling of the rapid rise in plasma resistivity which leads to the diode-like nature of the plasma focus observed in this work. Investigation into insulator properties may also be quite important since, even if there is a large induced voltage in the focus, there should be no current restrike across the insulator to short this voltage. An ideal insulator would provide a uniform current sheath initiation and then prevent restrike during the focus. Future efforts should concentrate on making the device more reproducible; an ultra high vacuum⁹⁶ may improve reproducibility by the absence of impurities in the plasma focus chamber.

Plasma focus research in the past 15 years has, for the most part, been concerned with the phenomenon of neutron production and x-ray production in order to utilize the plasma focus as a pulsed source of these radiations. In conjunction with these experiments, it was discovered that much of the phenomena associated with the plasma focus may be attributed to the intense charged particle beams. Much progress has been made in the processes involving the beams; however, the physical mechanism for beam production is still a mystery. It is hoped that this research will aid in the understanding of this subject.

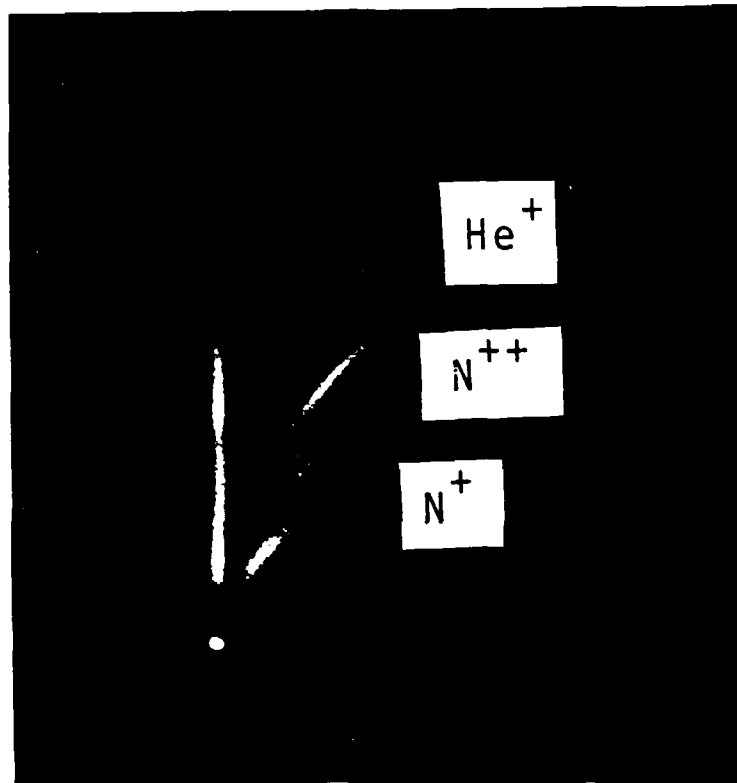


FIGURE 5-1. A THOMSON SPECTROGRAM WITH A CONSTANT ELECTRIC DEFLECTION SAME VALUES AS FIGURE 4-7

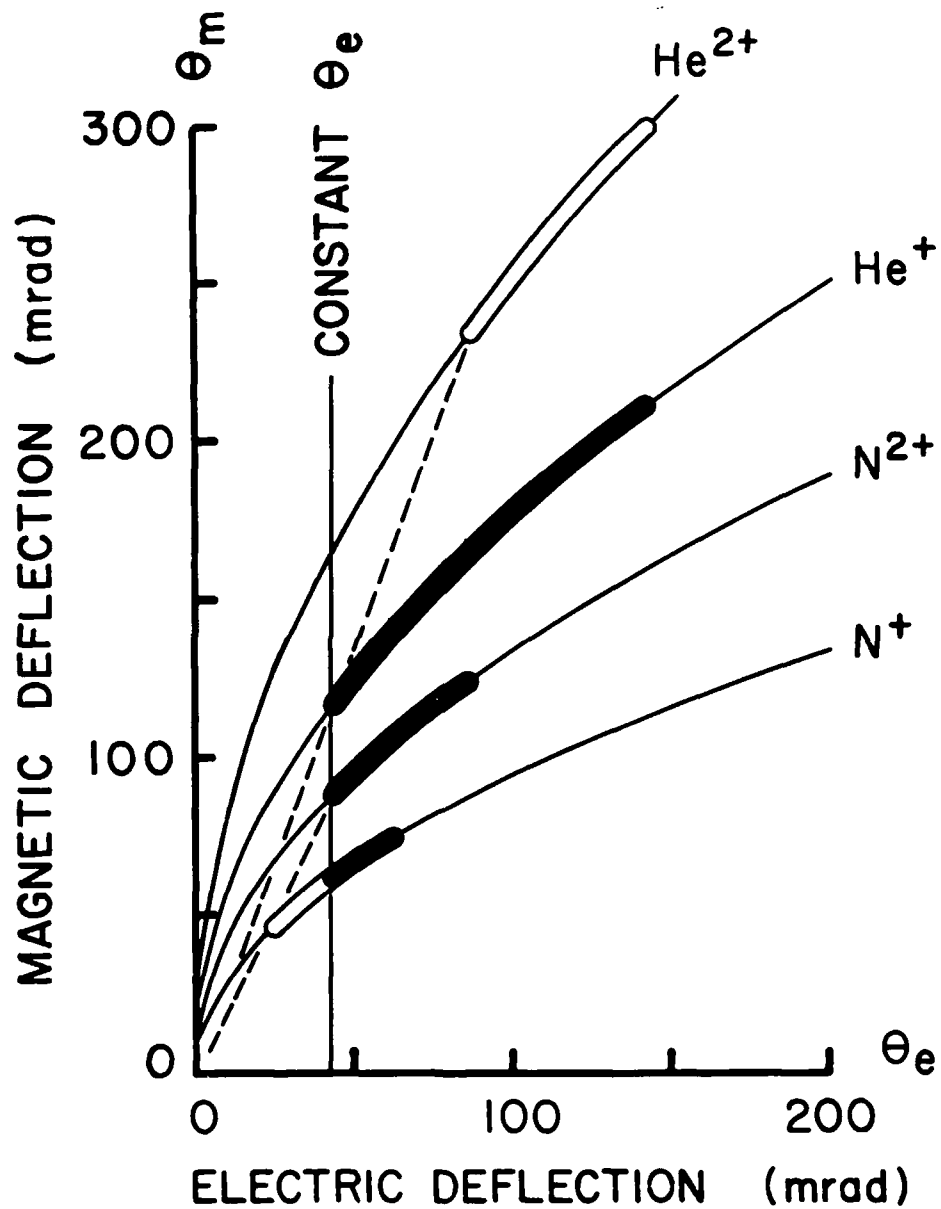


FIGURE 5-2. ANALYSIS OF FIGURE 5-1

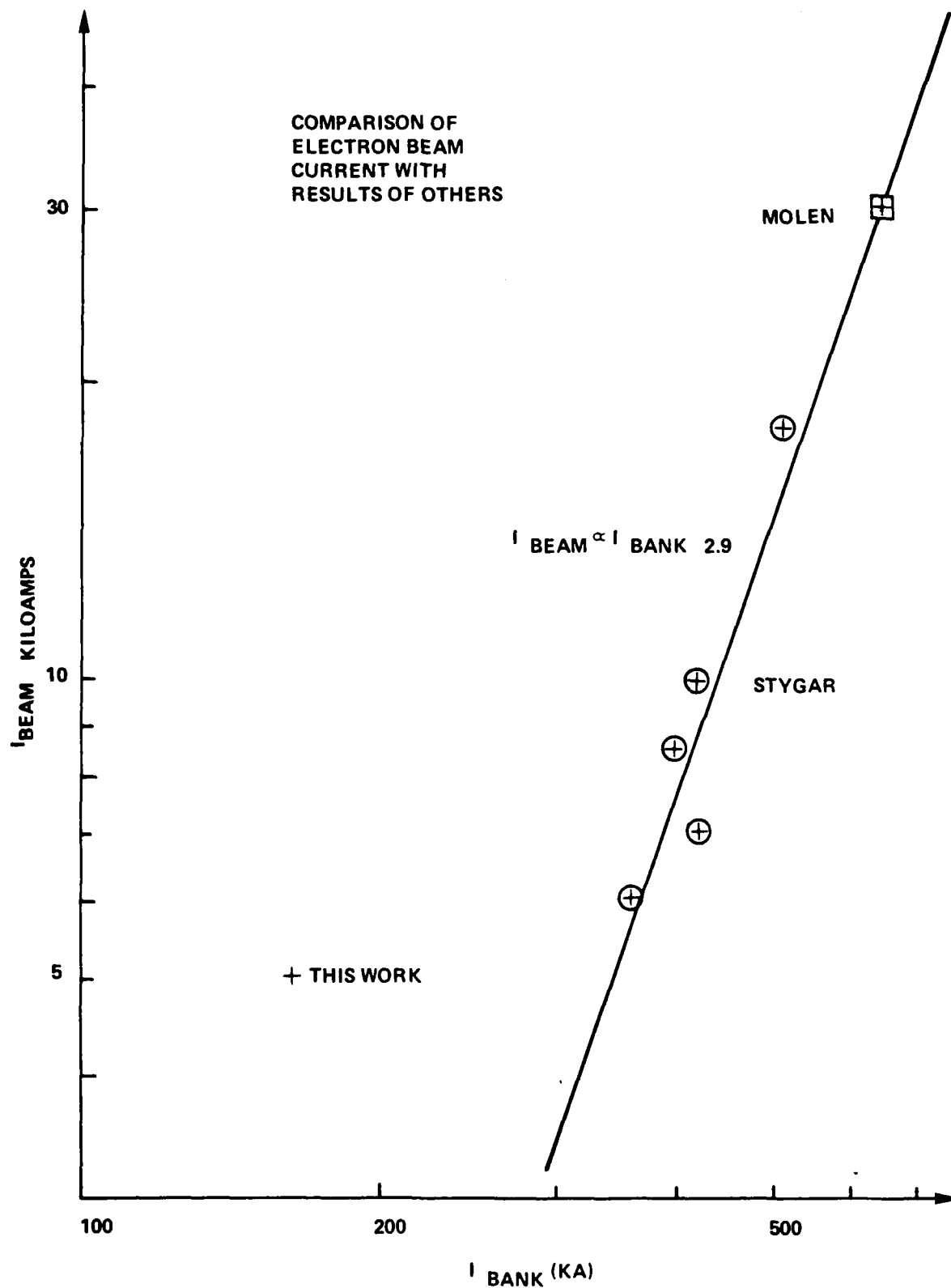


FIGURE 5-3. THE ELECTRON BEAM SCALING LAW $I_{\text{beam}} \propto I_{\text{bank}}^{2.9}$ PREDICTED IN REFERENCE 21 AND THE RESULT IN THIS WORK

REFERENCES

1. Filippov, N. V., Filippova, T. I. and Vinogradov, V. P., Nucl. Fusion Suppl. Pt. 2, 1962, p. 577.
2. Mather, J. W., Phys. Fluids 8, 1965, p. 366.
3. Bertalot, L., Deutsch, R., Herold, H., Jaeger, U., Kaeppler, H., Mozer, A., Oppenlaender, T., Rueckle, B., Sadowski, M., Schilling, P. and Schmidt, H., Proc. 8th Int. Conf. on Plasma Physics and Controlled Nucl. Fusion Research 1980, IAEA, Vienna, 1981, p. 177.
4. Peacock, N. J., Wilcock, P. D., Speer, R. J. and Morgan, P. D., Proceedings of the 3rd Int. Conf. on Plasma Physics and Controlled Nucl. Fusion Research, IAEA, Vienna, 1968.
5. Yokoyama, M., Kitagawa, Y., Yamada, Y., Yamanaka, C., and Hirano, K., Proc. 8th Int. Conf. on Plasma Physics and Controlled Nucl. Fusion Research 1980, IAEA, Vienna, 1981, p. 187.
6. Decker, G., et al., Pulsed High Beta Plasmas: 3rd Topical Conference 1975, Pergamon, New York, 1976, p. 401.
7. Bostick, W. H., Nardi, V., Prior, W. and Cortese, C., Pulsed High Beta Plasmas: 3rd Topical Conference 1975, Pergamon, New York, 1976, p. 407.
8. Krompholz, H., Neff, W., Schoenback, K. and Herziger, G., Phys. Lett. 76A, 1980, p. 388.
9. Tanis, M., Gerdin, G. and Venneri, F., Bull. Am. Phys. Soc. 29, 1984, p. 1266.
10. Fanning, J. J. and Kim, K. K., IEEE Conf. Record Abstracts, 1984 IEEE Int. Conf. on Plasma Sci., 1984, p. 106.
11. Kuyel, B., SPIE 275, 1981, p. 44.
12. Harries, W. L., Lee, J. H. and McFarland, D. R., Plasma Phys. 20, 1978, p. 95.
13. Lee, J. H., Hohl, F. and McFarland, D. R., Bull. Am. Phys. Soc. 24, 1979, p. 1079.
14. Herziger, G., Krompholz, H., Michel, L., Schlieferboeck, D., and Schoenback, K., Phys. Lett. 69A, 1978, p. 37.

REFERENCES (Cont.)

15. Banuelos, A., Bruzzone, H., Delellis, R., Gratton, J., Gratton, R., Kelly, H., Milanese, M., Pouzo, J. and Rodriguez-Trelles, F., Proc. 7th Int. Conf. on Plasma Physics and Controlled Nucl. Fusion Research 1978, IAEA, Vienna, 1978, p. 173.
16. Ivanov, V. D., Veretennikov, V. A., et al., Proc. 8th Int. Conf. on Plasma Physics and Controlled Nucl. Fusion Research 1980, IAEA, Vienna, 1981, p. 161.
17. Gullickson R. L. and Barlett, R. H., Adv. X-Ray Anal. 18, 1975, p. 184.
18. Krompholz, H., Michel, L., Schoenback, K. H. and Fischer, H., Appl. Phys. 13, 1977, p. 29.
19. Nardi, V., Bostick, W. H., Feugeas, J., Prior, W. and Cortese, C., Proc. 7th Int. Conf. on Plasma Physics and Controlled Nucl. Fusion Research 1978, IAEA, Vienna, 1978, p.143.
20. Neff, W., Krompholz, H., Ruhl, F., Schoenback, K. and Herziger, G., Phys. Lett. 79A, 1980, p. 165.
21. Stygar, W., Gerdin, G., Venneri, F. and Mandrekas, J., Nucl. Fusion 22, 1982, p. 1161.
22. Smith, J. R., Luo, C. M., Rhee, M. J. and Schneider, R. F., Proc. of 3rd Int. Wkshp. on Plasma Focus Res., 1983, p. 51.
23. Smith, J. R., Luo, C. M., Rhee, M. J. and Schneider, R. F., IEEE Conf. Rec. Abstracts, 1984 IEEE Int. Conf. on Plasma Sci., 1984, p. 105.
24. Schneider, R. F., Rhee, M. J. and Smith, J. R., IEEE Trans. Nucl.Sci. NS-32, Oct 1985.
25. Conrads, H., Cloth, P., Demmeler, M. and Hecker, R., Phys Fluids 15, 1972, p. 209.
26. Gullickson, R. L. and Sahlin, H. L., J. Appl. Phys. 49, 1978, p. 1099.
27. Krompholz, H., Grimm, E., Ruhl, F., Schoenback, K. and Herziger, G., Phys. Lett. 76A, 1980, p. 255.
28. Bertalot, L., Deutsch, R., Herold, H., Jaeger, U., Mozer, A., Sadowski, M., and Schmidt, H., Proc. 10th Eur. Conf. on Controlled Fusion and Plasma Physics, Moscow, 1981.
29. Gerdin, G., Stygar, W. and Venneri, F., J. Appl. Phys. 52, 1981, p. 3269.
30. Mozer, A., Sadowski, M., Herold, H. and Schmidt, H., J. Appl. Phys. 53, 1982, p. 2959.

REFERENCES (Cont.)

31. Gullickson, R. L., Luce, J. S. and Sahlin, H. L., J. Appl. Phys. 48, 1977, p. 37718.
32. Rager, J. P., et. al., Proc. 8th Int. Conf. on Plasma Physics and Controlled Nucl. Fusion Research 1980, IAEA, Vienna, 1981, p. 209.
33. Rhee, M. J., Luo, C. M., Schneider, R. F. and Smith, J. R., Proc. 3rd Int. Wkshp. on Plasma Focus Res., 1983, p. 47.
34. Rhee, M. J., Luo, C. M., Schneider, R. F. and Smith, J. R., Bull. Am. Phys. Soc. 28, 1983, p. 1171.
35. Cebanu, A., et. al., Proc. 8th Int. Conf. on Plasma Physics and Controlled Nucl. Fusion Research 1980, IAEA, Vienna, 1981, p. 197.
36. Marshall, J., Phys. Fluids 3, 1960, p. 134.
37. Woodall D. M. and Len, L. K., J. Appl. Phys. 57, 1985, p. 961.
38. Borowiecki, M., Czekaj, S., Koziarkiewicz, W., Skrzeczanowski, W., Socha, R., Tomaszewski, K. and Zadrozny, M., Proc. 11th Int. Symp. on Discharges and Electrical Insulation in Vacuum, p. 4.109.
39. Krompholz, H., Neff, W., Ruhl, F., Schoenback, K. and Herziger, G., Phys. Lett. 77A, 1980, p. 246.
40. Comisar, G. G., Phys. Fluids 12, 1969, p. 1000.
41. Bernstein, M. J. and Comisar, G. G., Phys. Fluids 15, 1972, p. 700.
42. Hohl, F. and Gary, S. P., Phys. Fluids 20, 1977, p. 683.
43. Gary, S. P., Phys. Fluids 17, 1974, p. 2135.
44. Kondoh, Y. and Hirano, K., Phys. Fluids 21, 1978, p. 1617.
45. Deutsch, R., "Ion Acceleration in the Plasma Focus," Internal Report IPF-82-6, Inst. f. Plasmaforschung der U. Stutt., 1982.
46. Kirk, R. E., Forrest, M. J., Muir, D. G. and Peacock, N. J., IEEE Conf. Rec. Abstracts, 1984 IEEE Int. Conf. on Plasma Sci., 1984, p. 105.
47. Krompholz, H. and Herziger, G., "Phenomena of Selforganization in Dense Plasma Focus," Internal Report, Institut f. Angewandte Physik, der Technische Hochschule Darmstadt.
48. Gerdin, G., Venneri, F. and Tanis, M., IEEE Conf. Record Abstracts, 1985 IEEE Int. Conf. on Plasma Science, 1985, p. 76.
49. Eltgroth, P. G., Phys. Fluids 25, 1982, p. 2408.

REFERENCES (Cont.)

50. Mather, J. W., Methods of Experimental Physics, Lovberg, R. L. and Griem, H. R., Eds., Academic Press, New York, 1971.
51. Rhee, M. J. and Schneider, R. F., IEEE Trans. Nucl. Sci. NS-30, 1983, p. 3192.
52. Miller, R. B., An Introduction to the Physics of Intense Charged Particle Beams, Plenum, New York, 1982.
53. Goldstein, S. A. and Lee, R., Phys. Rev. Lett. 35, 1975, p. 1079.
54. Gullickson, R. L., Proceedings of the Second International Workshop on Plasma Focus, 1981, p. 154.
55. Alston, L. L., Ed., High Voltage Technology, Oxford Univ. Press, Oxford, 1968.
56. Rogowski, W. and Steinhaus, W., Arch. Electrotech. 1, 1912, p. 141.
57. Leonard, S. L., Plasma Diagnostic Techniques, Huddleston, R. H. and Leonard, S. L., Eds., Academic Press, New York, 1965.
58. Nassisi, V. and Luches, A., Rev. Sci. Instrum. 50, 1979, p. 900.
59. Shpilman, A., M. S. Thesis, University of Maryland, 1983.
60. Mather, J. W. and Williams, A. H., Rev. Sci. Instrum. 31, 1960, p. 297.
61. Rhee, M. J., Park, B. S. and Schneider, R. F., IEEE Conf. Rec. Abstracts, 1984 IEEE Int. Conf. on Plasma Sci., 1984, p. 9.
62. Berger, M. J. and Selter, S. M., Stopping Power and Ranges of Electrons and Positrons, U. S. Dept. of Comm., NBS, Washington, DC, 1982.
63. Smith, J. R., Luo, C. M., Rhee, M. J. and Schneider, R. F., Phys. Fluids 28, 1985, p. 2305.
64. Chen, F., Introduction to Plasma Physics, Plenum, New York, 1974.
65. Gilgenbach, R. M., et al., IEEE Conf. Record Abstracts, 1985 IEEE Int. Conf. on Plasma Science, 1985 p. 31.
66. Destler, W. W., O'Shea, P. G. and Reiser, M., Phys. Rev. Lett. 52, 1984, p. 1978.
67. Schneider, R. F., Rhee, M. J. and Smith, J. R., Bull. Am. Phys. Soc. 29, 1984, p. 1266.
68. Lee, J. H., Proceedings of the Second International Workshop on Plasma Focus, 1981, p. 196.

REFERENCES (Cont.)

69. "Precision NTC Thermistors," Sensor Sci. Inc., Catalog 105, 1983, p. 2.
70. Rosenhow, W. M., and Choi, H., Heat, Mass, and Momentum Transfer, Prentice Hall, Englewood Cliffs, NJ, 1961, pp. 87-131.
71. Reif, F., Fundamentals of Statistical and Thermal Physics, McGraw-Hill, New York, 1965, pp. 478-483.
72. Lawson, J. L. and Tyler, A. W., Rev. Sci. Instrum. 11, 1940, p. 6.
73. Siegbahn, K., Alpha-, Beta-, and Gamma-Ray Spectroscopy, North Holland, Amsterdam, 1965.
74. Gosteva, T. S., Zablotskaya, G. R., Ivanov, B. A., Kolyubakin, S. A. and Chernobrovin, V. I., Prib. Tekh. Eksp. 3, 1975, p. 44, [Instrum. Exp. Tech. 18, 1975, p. 711].
75. Lawson, J. D., The Physics of Charged Particle Beams, Clarendon Press, Oxford, 1977, Chap. 4.
76. Lapostolle, P. M., IEEE Trans. Nucl. Sci. NS-18, 1971, p. 1101.
77. Sacherer, F. J., IEEE Trans. Nucl. Sci. NS-18, 1971, p. 1105.
78. Lejeune, C. and Aubert, J., Applied Charged Particle Optics, Septier, A., Ed., Academic Press, New York, 1980, Part A, pp. 159-259.
79. Lawson, J. D., Lapostolle, P. M. and Gluckstern, R. L., Particle Accel. 5, 1973, p. 61.
80. Rhee, M. J., Zorn, G. T., Placious, R. C. and Sparrow, J. H., IEEE Trans. Nucl. Sci. NS-18, 1971, p. 468.
81. Smith, J. R., et al., IEEE Trans. Nucl. Sci. NS-32, Oct. 1985.
82. Humphreys, K. C. and Kantz, A. D., IEEE Trans. Nucl. Sci. NS-26, 1979, p. 1784.
83. Rhee, J. J. and Schneider, R. F., submitted to Part. Accel.
84. Schneider, R. F., Luo, C. M., Rhee, M. J. and Smith, J. R., Bull. Am. Phys. Soc. 28, 1983, p. 1171.
85. Fowler, P. H., Amin, S., Clapham, V. M. and Henshaw, D. L., Solid State Nuclear Track Detectors, Proceedings of the 10th Int. Conf., 1979, Francois, H., Massue, J. P., and Schmitt, R., Eds., Pergamon, Oxford, 1980, p. 239.
86. Fleischer, R. L., Price, P. B. and Walker, R. M., Nuclear Tracks in Solids, University of California, Berkeley, 1975.

REFERENCES (Cont.)

87. Pyle, J., Rhee, M. J. and Shpilman, A., Newsletter of the University of Maryland Electron Microscope Central Facility 11, 1983, p. 8.
88. Rahman, H. U., Amendt, P. and Rostoker, N., Phys. Fluids 28, 1985, p. 1528.
89. Schneider, R. F. and Rhee, M. J., IEEE Conf. Rec. Abstracts, 1985 IEEE Int. Conf. on Plasma Sci., 1985, p. 75.
90. Bertalot, L., et al., Phys. Lett. 79A, 1980, p. 389.
91. Rhee, M. J., Rev. Sci. Instrum. 55, 1984, p. 1229.
92. Schneider, R. F. and Rhee, M. J., IEEE Conf. Rec. Abstracts, 1985 IEEE Int. Conf. on Plasma Sci., 1985, p. 85.
93. Luo, C. M., Nardi, V. and Powell, C., IEEE Conf. Rec. Abstracts, 1985 IEEE Int. Conf. on Plasma Sci., 1985, p. 75.
94. Rhee, M. J. and Schneider, R. F., submitted to Phys. Lett.
95. Hill, R. A., IEEE Conf. Rec. Abstracts, 1985 IEEE Int. Conf. on Plasma Sci., 1985, p. 74.
96. Schiller, N. H., et al., Optical Spectra, Jun 1980.

APPENDIX A

MAGNETIC ELECTRON ENERGY ANALYZER RESOLUTION

Resolution^{A-1} is an important consideration in the design of an energy analyzer. For convenience, we define the relative energy resolution as the uncertainty in the measurement at some energy as a fraction of that energy, $\Delta T/T = R_T$. Under the assumption of uniform magnetic field configuration provided by the iron case and magnet as well as the absence of space charge effects in the analyzer, the resolution is determined by the non-ideal collimation of the two-slit collimator. Figure A-1 shows the idealized two-dimensional geometry required for resolution analysis. Three different particle trajectories with different energies all impacting at the same point on the detector are shown. The detector is placed along the line (detector line) separating the uniform field region from the collimation region. In this case, the downstream collimator slit lies directly on the detector line. For analysis we define new coordinates d and θ , where d is the distance between the point where any arbitrary particle trajectory crosses the detector line and the center of the downstream slit (see Figure A-1). The quantity θ is the angle that the particle trajectory makes with a line normal to the detector line shown in the figure. If the limits on θ are determined by a double slit collimator, then the maximum possible θ is just half the maximum acceptance angle of the collimator. If the upstream and downstream slits of width D_1 and D_2 , respectively, are

^{A-1}Schneider, R. F., Luo, C. M., Rhee, M. J., and Smith, J. R., Rev. Sci. Instrum. 56, Aug. 1985.

separated by a distance L , then θ_{\max} is given by:

$$\theta_{\max} = \tan^{-1} \left(\frac{D_1 + D_2}{2L} \right) . \quad (\text{A-1})$$

Using these quantities and assuming the particles follow circular trajectories upon entering the B field, we find the distance from the center of the entrance slit to the point of impact on the detector as:

$$z = 2\rho(T)\cos\theta + d , \quad (\text{A-2})$$

where:

$$\rho(T) = \frac{(T^2 + 2Tmc^2)^{1/2}}{eB} . \quad (\text{A-3})$$

The equation for z can be expanded in series around $\theta=0$, $d=0$, and $T=T$.

Keeping only the lowest nonvanishing order terms, we arrive at:

$$\Delta z = \frac{\partial z}{\partial T} \Delta T + \frac{1}{2} \frac{\partial^2 z}{\partial \theta^2} (\Delta \theta)^2 + \frac{\partial z}{\partial d} \Delta d . \quad (\text{A-4})$$

Suppose we measure the distance z exactly ($\Delta z=0$). The energy of the electron at that point may be associated with that corresponding to an orbit with radius $z/2$. We need to know the maximum uncertainty introduced into T (i.e., ΔT_{\max}) by $\Delta \theta$ and Δd . If we have finite $\Delta \theta$ and Δd , then ΔT_{\max} will just be the sum of the magnitude of the uncertainties due to $\Delta \theta_{\max}$ and Δd_{\max} . Solving for ΔT and setting $\Delta d_{\max} = D_2/2$ and $\Delta \theta_{\max} = \theta_{\max}$, the resolution function is found to be:

$$R(T) = \frac{ecB(T^2 + 2Tmc^2)^{1/2}}{T(T + mc^2)},$$

(A-5)

$$X\left[\frac{D_2}{4} + \frac{(T^2 + 2Tmc^2)^{1/2}}{2ecB} \theta_{\max}^2\right].$$

Figure A-2 is a plot of this function for the values $D_1 = 125\mu\text{m}$, $D_2 = 25\mu\text{m}$, $L = 35\text{ mm}$, and $B = 0.53\text{ Tesla}$. These are the values used in our experiment.

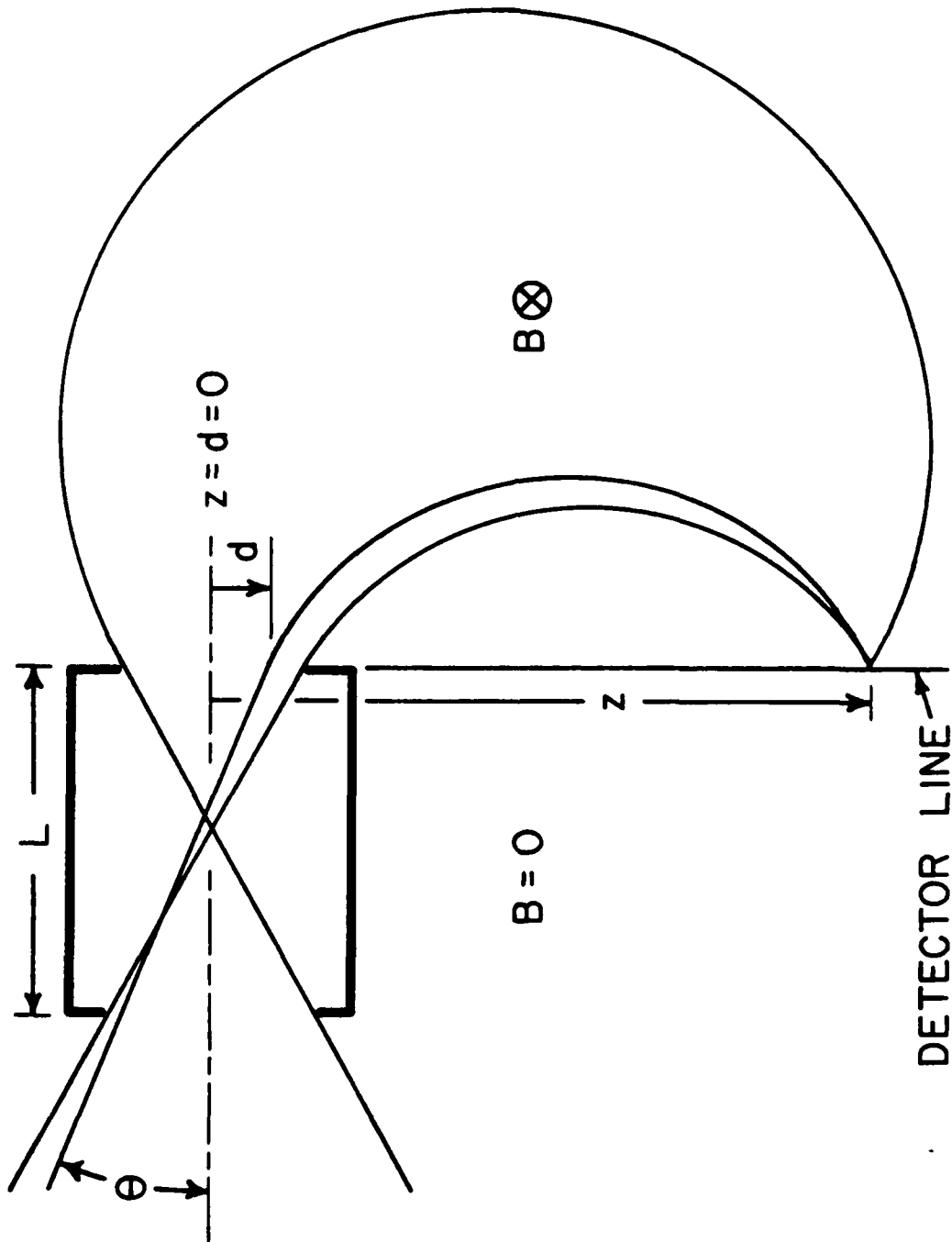


FIGURE A-1. GEOMETRY FOR MAGNETIC ELECTRON ENERGY ANALYZER
RESOLUTION ANALYSIS

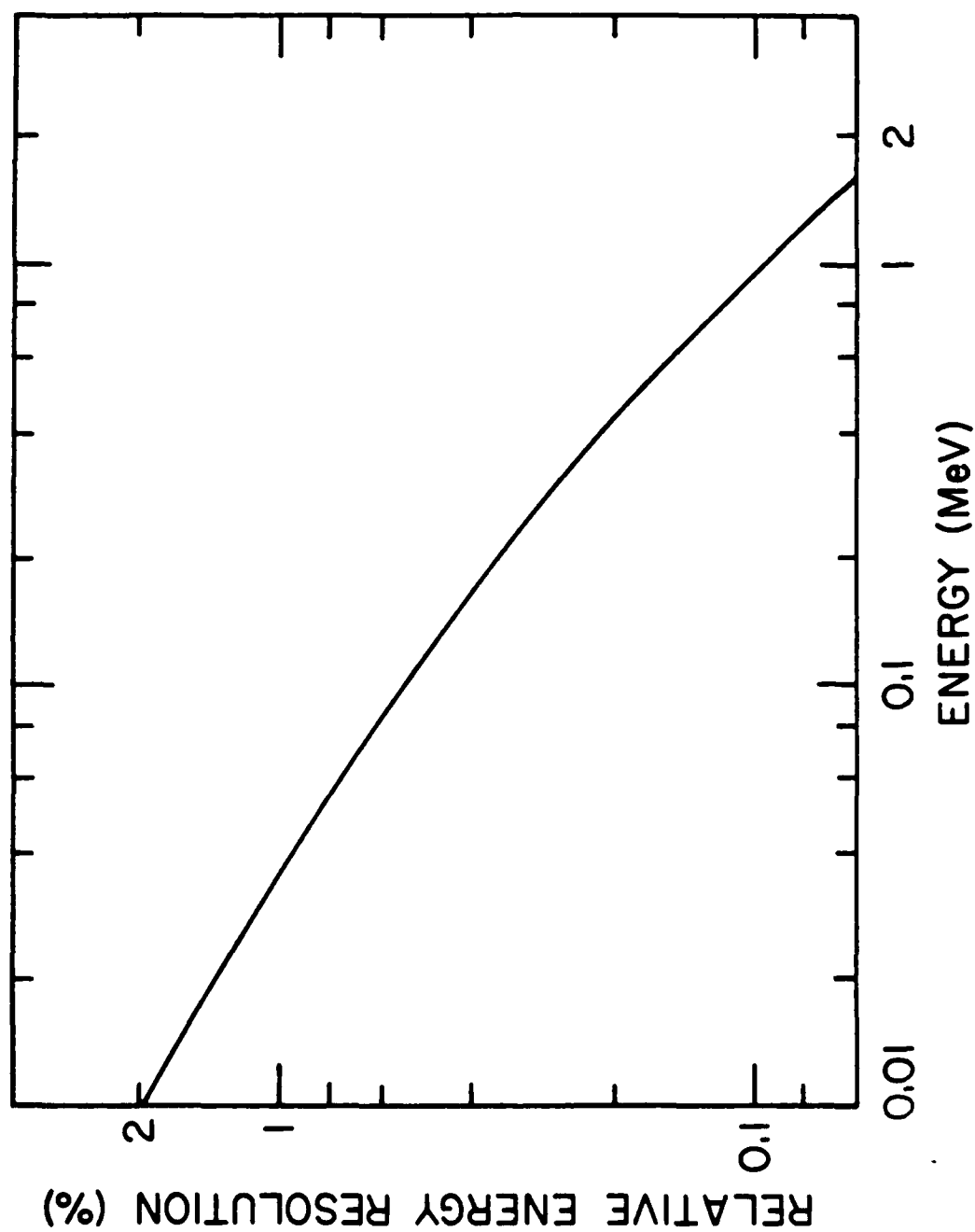


FIGURE A-2. RESOLUTION FUNCTION FOR THE MAGNETIC ANALYZER

APPENDIX B

THOMSON SPECTROMETER RESOLUTION^{B-1}

A major purpose of the Thomson spectrometer is to separate parabolas of different charge-to-mass ratio in order to differentiate ion species and charge state. This in principle happens naturally if the parabola is an infinitely thin line. Practically, however, this can never be done since the collimation procedure utilizes two pinholes which produce an image with finite diameter as displayed in Figure B-1. The resulting widths of the parabolas, which are swept out by the different energies of a given charge-to-mass ratio, leads to overlapping, which reduces the resolution of the spectrometer. From the geometry of Figure B-1, the width of the parabola on the detector is given by:

$$D_3 = \frac{L_2}{L_1} (D_1 + D_2) + D_2 . \quad (B-1)$$

This corresponds to a subtended angle of:

$$\delta = \frac{D_3}{L_2} . \quad (B-2)$$

The overlapping of the parabolas as they near the origin can be calculated, and resolution criterion can be obtained by determining the points where

^{B-1}Schneider, R. F., Luo, C. M., and Rhee, M. J., J. Appl. Phys. 57, 1985, p. 1.

different charge-to-mass ratio parabolas are separated for either constant charge or constant mass. It is interesting to note that these equations arise solely from the pinhole geometry and are independent of the location of the field region so that they are applicable to the conventional Thomson spectrometer. The only difference between compact and conventional spectrometers is the location of the pinholes relative to the fields. In the compact spectrometer, the field region is placed between the first and second pinholes allowing much more control over the pinhole collimation image on the detector. In conventional spectrometers, the pinhole collimation system is entirely upstream of the fields. This implies the distance L_2 in Figure B-1 must be large enough to contain the fields. This limits the minimum obtainable D_3 and, hence, requires a spectrometer which is an order of magnitude larger to obtain the same resolution. There is a slight condition which must be met in the use of this spectrometer, namely the entire spectrometer entrance must be uniformly illuminated by the ion source. This is quite easy to achieve in the plasma focus since the source is of finite spatial dimension and the first pinhole is 40 cm upstream of the spectrometer and 8 cm upstream of the focus allowing a source of less than 0.1 mm to cover the entire entrance to the spectrometer.

To analyze charge resolution, we suppose that we have one ion species with several different charge states. Along what curve can we find points at which neighboring parabolas are separated? To answer, we use the criterion for separation that $\Delta\theta_m$, the separation of the centers of the parabolas along a vertical line, i.e., θ_m direction must be greater than the parabola width along that line:

$$\Delta\theta_m \geq \delta \left(1 + \frac{\theta_m^2}{4\theta_e^2}\right)^{1/2} \text{ and } \Delta\theta_e = 0, \quad (\text{B-3})$$

This is illustrated in Figure B-2. Here we have made use of the fact that the slope of the parabola is given by:

$$\frac{d\theta_m}{d\theta_e} = \frac{\theta_m}{2\theta_e}, \quad (\text{B-4})$$

which is derived from the parabola equation. Assuming small $\Delta\theta_m$, we can substitute the separation condition above into the total differential of the parabola equation with Z , A , θ_e , and θ_m as variables yielding:

$$\frac{dZ}{A} - Z \frac{dA}{A^2} = \frac{u}{e} \frac{\int Edl}{(\int Bd1)^2} \frac{2\theta_m}{\theta_e} \delta \left[1 + \left(\frac{\theta_m}{2\theta_e}\right)^2\right]^{1/2}. \quad (\text{B-5})$$

If $dA = 0$ and $dZ = 1$, we will arrive at the equation describing the line connecting the points of charge resolution for a certain ion species:

$$\theta_m^4 + \theta_m^2 (4\theta_e^2) - \left(\frac{k}{A\delta}\right)^2 \theta_e^4 = 0. \quad (\text{B-6})$$

We have made the definition:

$$k = \frac{e}{u} \frac{(\int Bd1)^2}{\int Edl}. \quad (\text{B-7})$$

The physical solution to the quartic equation is:

$$\theta_m = \left\{ \left[4 + \left(\frac{k}{A\delta}\right)^2 \right]^{1/2} - 2 \right\}^{1/2} \theta_e \quad (\text{B-8})$$

which describes a straight line which intersects the origin. This is illustrated in Figure B-3. Below this line, the parabolas of every charge state of ion mass A are separated. An alternate way of viewing this is to note that such lines are constant velocity lines with velocity:

$$v = \frac{\int E dl}{\int B dl} \left\{ \left[4 + \left(\frac{k}{A\delta} \right)^2 \right]^{1/2} - 2 \right\}^{1/2}. \quad (B-9)$$

Any ions with velocity less than this value will be resolved. Thus, large values of k/δ will yield better charge resolution.

For mass resolution, let $dZ = 0$, $dA = 1$. Using the parabola Equation (4-8) to eliminate A, we obtain:

$$\theta_m^6 - (Zk\delta\theta_m)^2 - 4(Zk\delta\theta_e)^2 = 0, \quad (B-10)$$

which can be solved numerically. An interesting analytical result can be derived when the charge state Z in the equation for mass resolution is eliminated in favor of mass number A through the parabola equation. In this case, we find the curve which connects the resolution points (points of separation) of parabolas with atomic numbers A and A+1 with different charge states:

$$\theta_m = \frac{2A\delta\theta_e}{[\theta_e^2 - (A\delta)^2]^{1/2}}. \quad (B-11)$$

This equation describes a hyperbola with asymptotes $\theta_e = A\delta$ and $\theta_m = 2A\delta$ above which isotopes are resolved as in Figure B-4. This can be generalized to $dA = n$

provided n/A is much less than 1 in order to obtain a resolution curve for elements which differ in mass number by n . This leads to the simple modification in the previous equation that A must be replaced by A/n everywhere it appears.

Energy and momentum resolution is also limited by the subtended angle of the pinhole collimation spot, δ . The spectrogram can be thought of as a superposition of many of these spots infinitely close together along the parabola length. Energy or momentum which is found from either the electric or magnetic deflection angle is, hence, uncertain by the an amount corresponding to the projection of the collimation spot length δ along the parabola onto the electric or magnetic deflection axis of the spectrogram (see Figure B-5). Within our approximation, these quantities are related by the equation:

$$\delta^2 = \left[1 + \left(\frac{\theta}{2\theta_e} \right)^2 \right] (\Delta\theta_e)^2, \quad (\text{B-12})$$

where we have used Equation (B-4). Relative energy and momentum uncertainties $\Delta T/T$ and $\Delta p/p$ can be found from the deflection equations in terms of θ_e as,

$$\alpha_T = \frac{\Delta T}{T} = - \frac{\Delta\theta_e}{\theta_e}, \quad (\text{B-13})$$

$$\alpha_p = \frac{\Delta p}{p} = - \frac{\Delta\theta_e}{2\theta_e}. \quad (\text{B-14})$$

A quantity Q_i representing either T or p can be expressed along with its uncertainty as $Q_i(1 \pm \alpha_i/2)$. It is of interest to find the curves of constant α_i which will give a contour map of relative uncertainty of energy or momentum.

Combining the equations for δ and α yields:

$$\frac{\theta_e^2}{(\delta/\alpha_T)^2} + \frac{\theta_m^2}{(2\delta/\alpha_T)^2} = 1, \quad (B-15)$$

$$\frac{\theta_e^2}{(\delta/2\alpha_p)^2} + \frac{\theta_m^2}{(\delta/\alpha_p)^2} = 1. \quad (B-16)$$

These describe upright ellipse about the origin which are contours of constant relative uncertainty as illustrated in Figure B-6. The relative energy or momentum resolution at a certain point on the parabola corresponds to the α_T or α_p value of the ellipse that intersects that point. In terms of spectrometer parameters, we may find α_T by combining the deflection Equations (4-6) and (4-7) with Equation (B-16).

$$\alpha_T = \frac{\delta}{\theta_e} \left[1 + \frac{Z}{A} \left(\frac{k}{4\theta_e} \right) \right]^{-1/2}. \quad (B-17)$$

The resolution function is plotted in Figure B-7 for the spectrometer parameters used for the energy spectrum measurements.

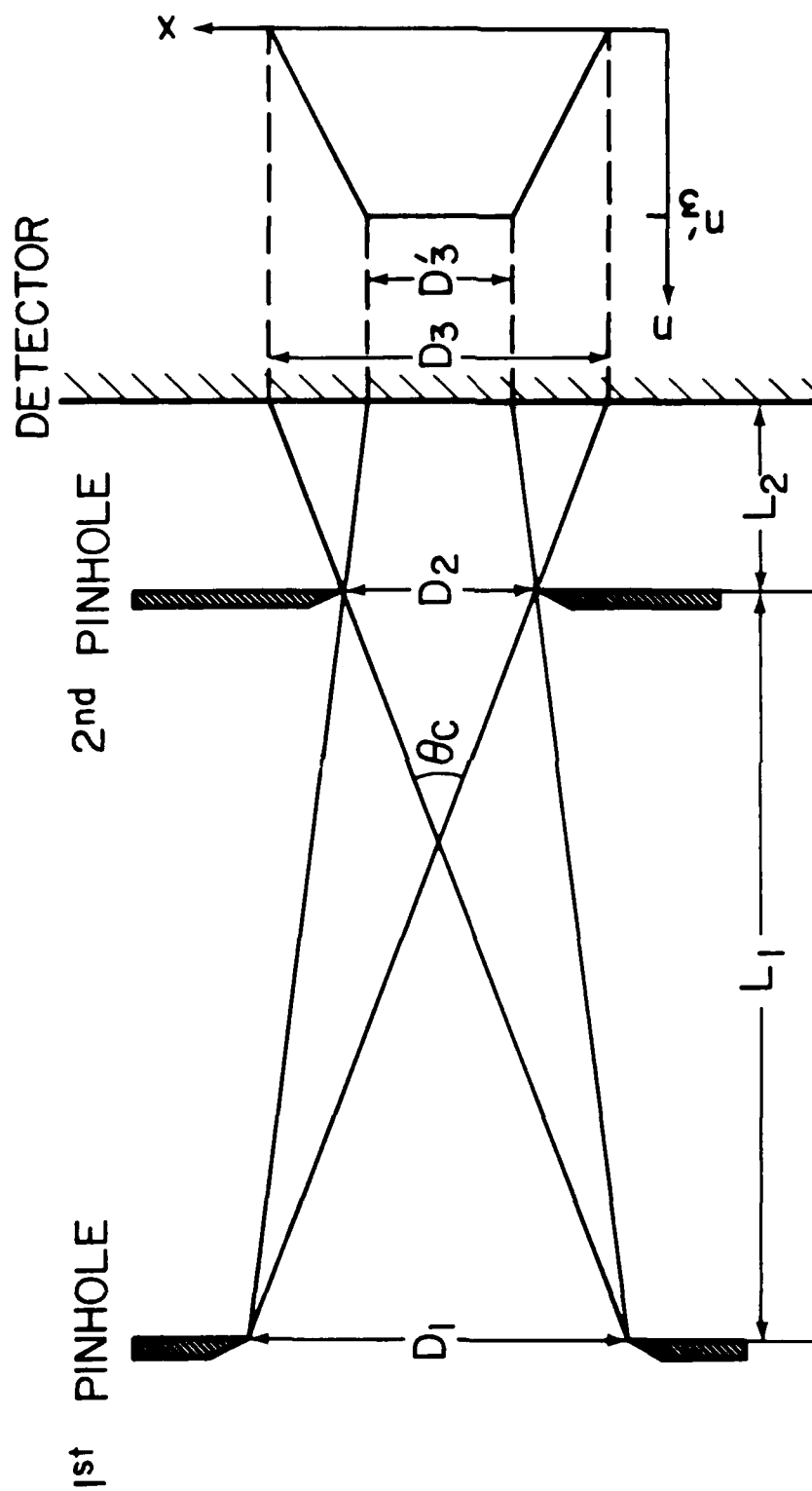


FIGURE B-1. PINHOLE IMAGE GEOMETRY FOR THOMSON SPECTROMETER COLLICATOR

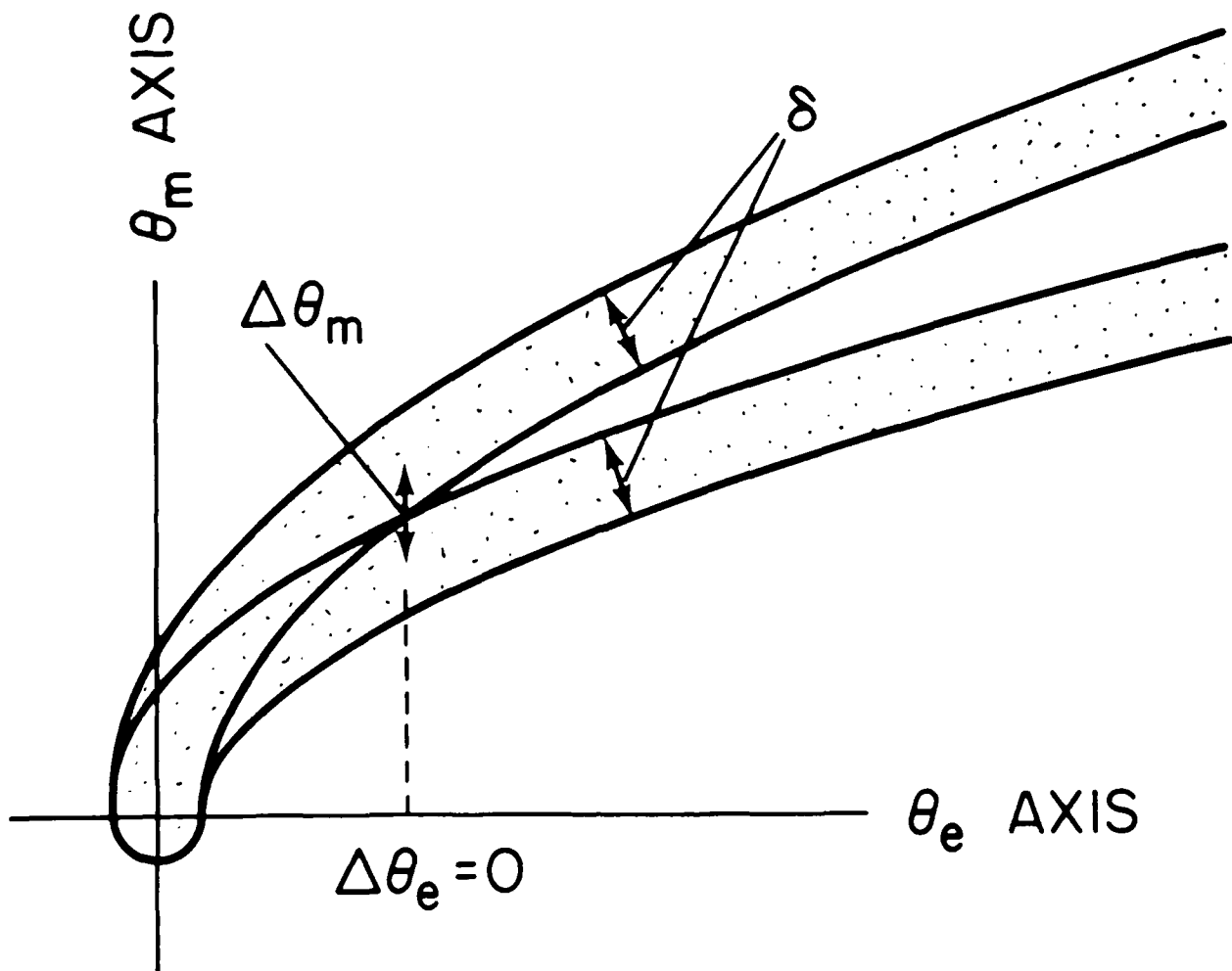


FIGURE B-2. SEPARATION OF PARABOLAS FOR CHARGE RESOLUTION ANALYSIS

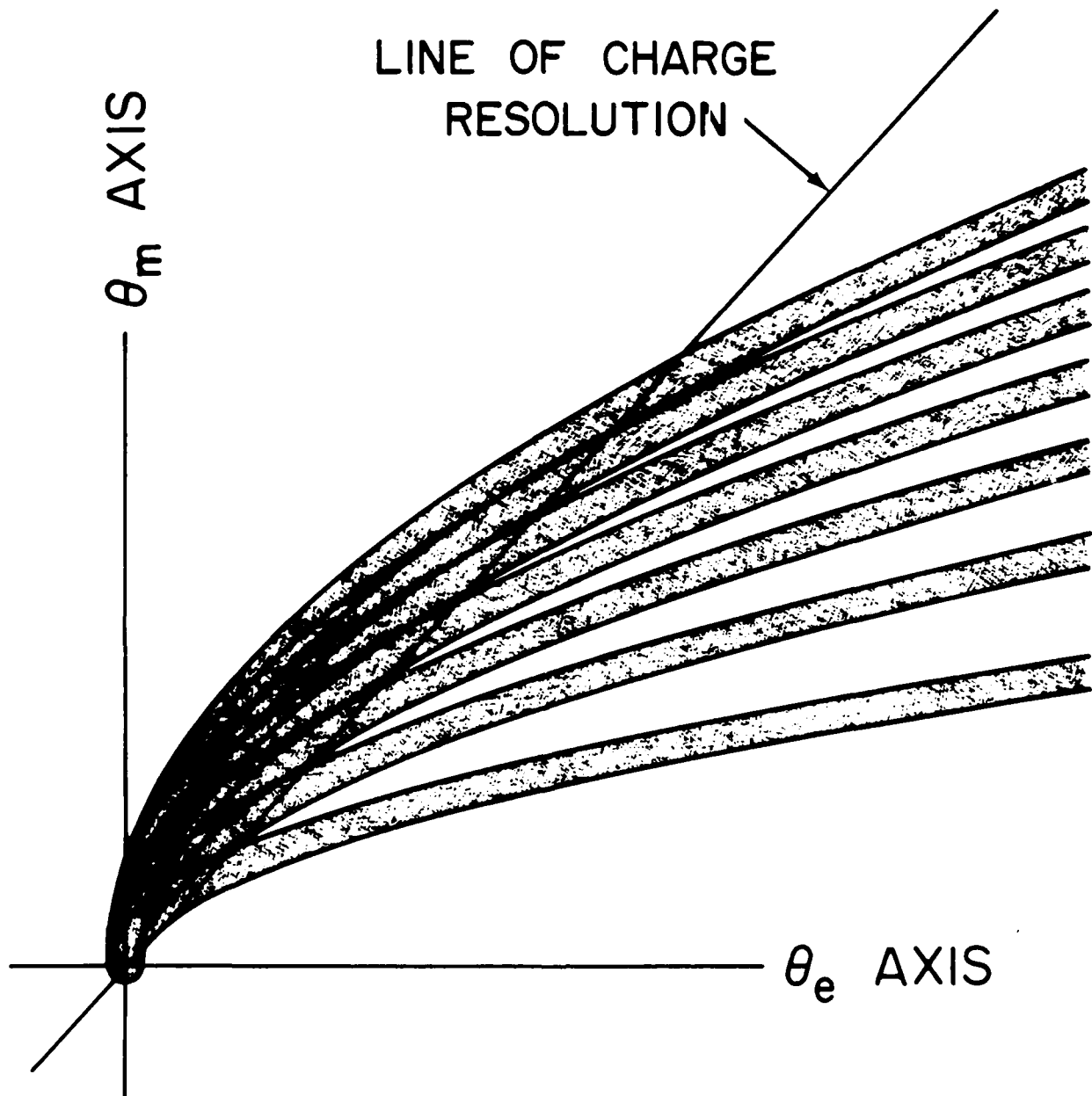


FIGURE B-3. CHARGE STATE RESOLUTION OF THE THOMSON SPECTROMETER. THE LINE SEPARATES THE REGIONS WHERE CHARGE IS RESOLVED FROM REGIONS WHERE IT IS UNRESOLVED.

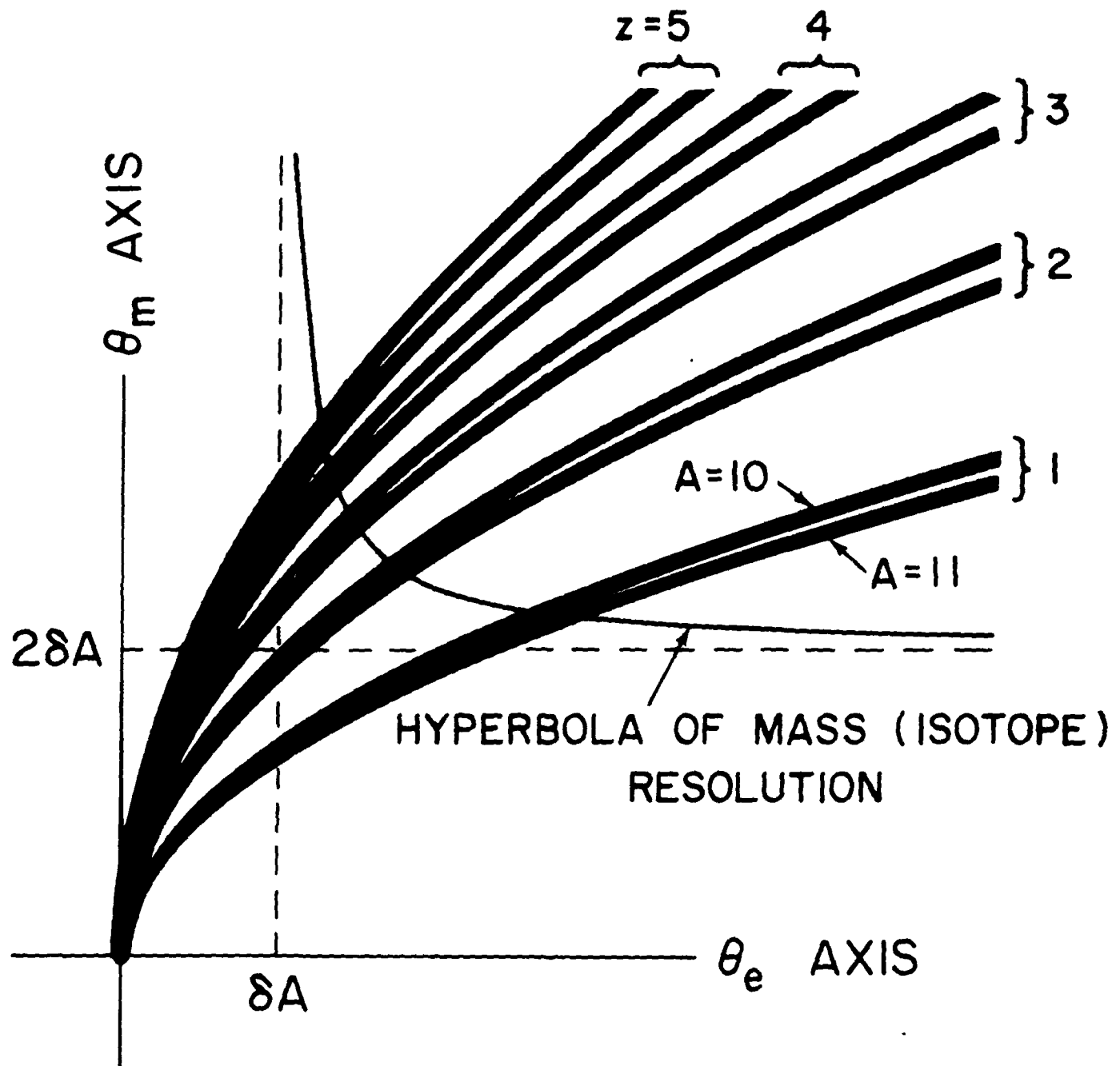


FIGURE B-4. ISOTOPE RESOLUTION HYPERBOLA

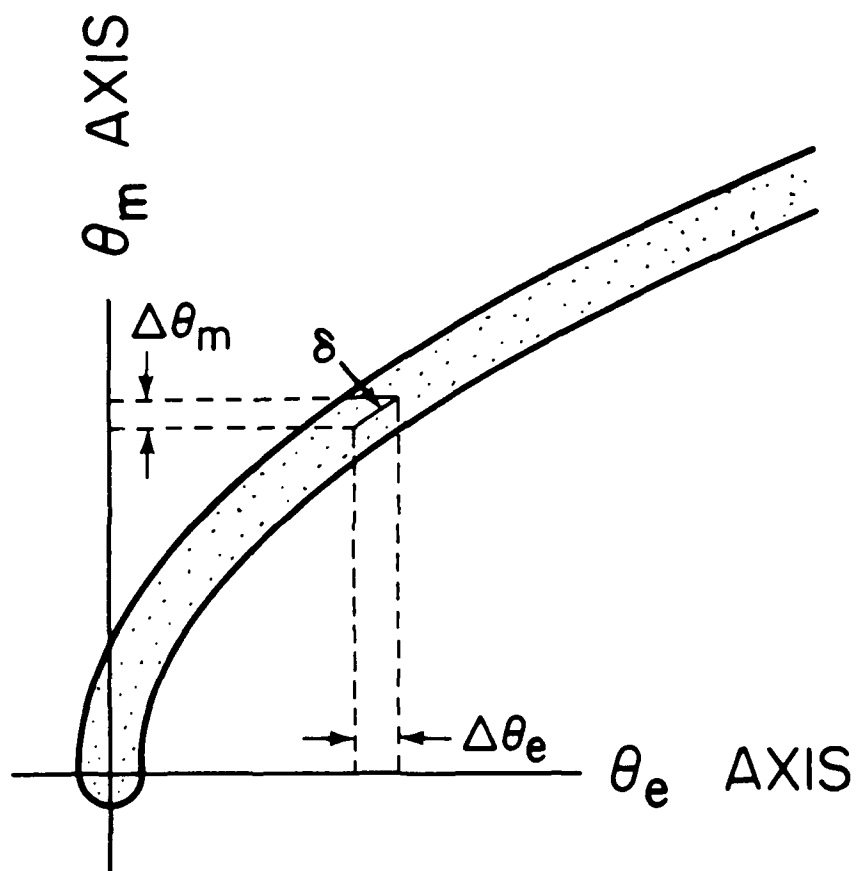


FIGURE B-5. GEOMETRY FOR ENERGY RESOLUTION

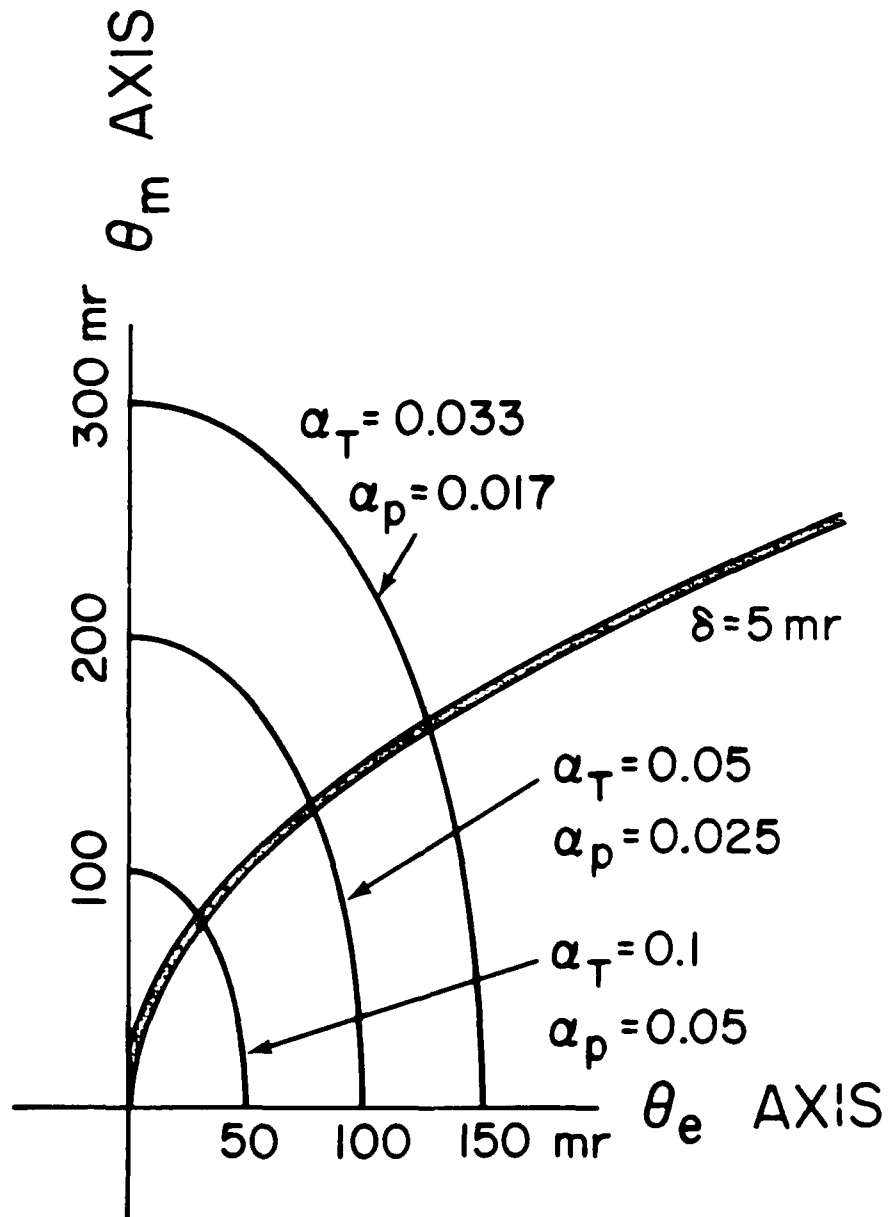


FIGURE B-6. CONTOURS OF CONSTANT RELATIVE ENERGY OR MOMENTUM UNCERTAINTY WHICH ARE ELLIPSES

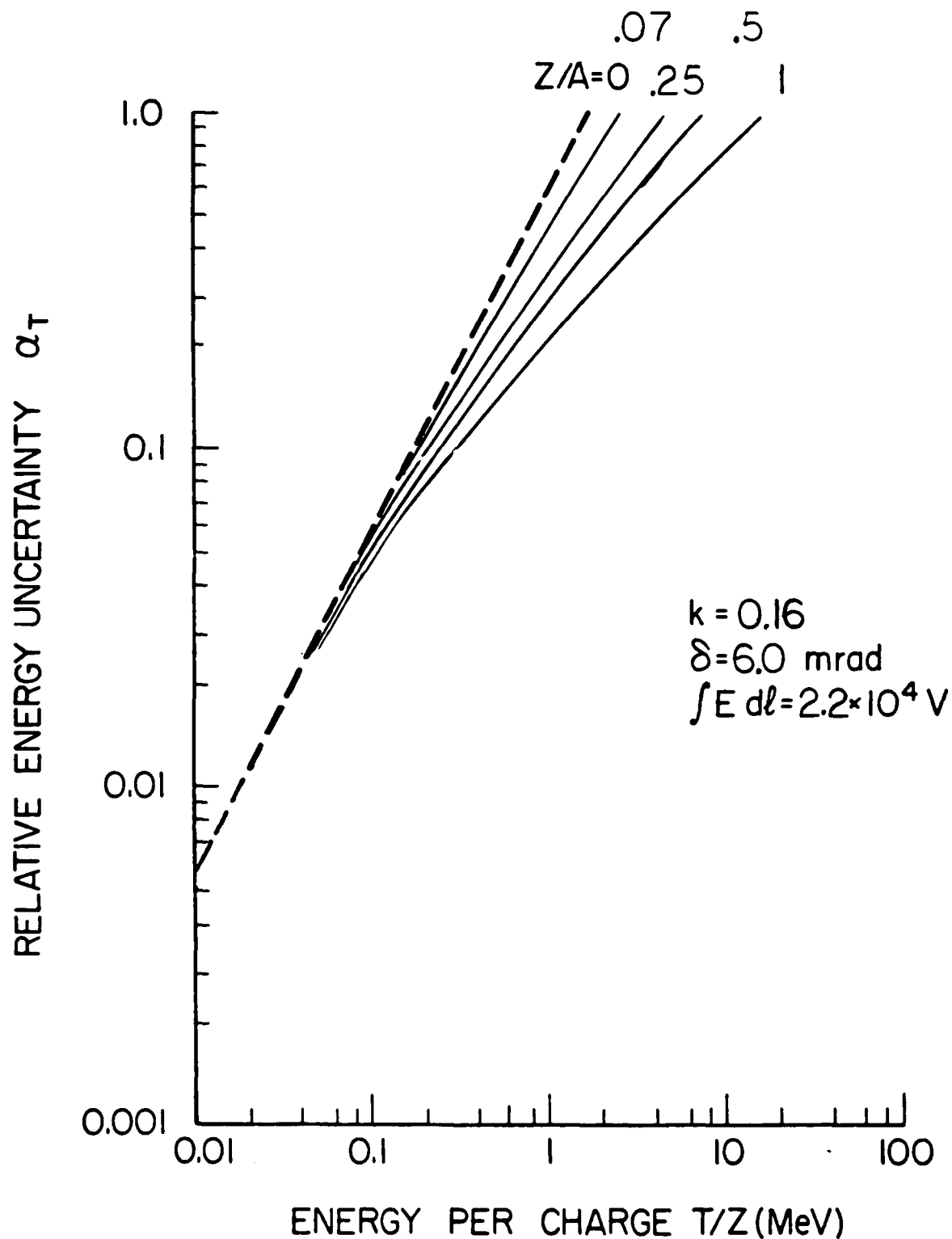


FIGURE B-7. PLOT OF RELATIVE UNCERTAINTY VERSUS ENERGY PER CHARGE FOR THE SPECTROMETER USED TO OBTAIN ION ENERGY SPECTRA

DISTRIBUTION

	<u>Copies</u>		<u>Copies</u>
Strategic Defense Initiative Organization		Internal Distribution:	
Attn: LTCOL R. L. Gullickson	1	R	1
Directed Energy Office		R40	1
The Pentagon		R41	1
Washington, DC 20301-7100		R41 (H. Uhm)	1
		R41 (D. Rule)	1
Defense Advanced Research Projects Agency		R41 (R. Fiorito)	1
Attn: Dr. Shen Shey	1	R41 (R. Chen)	1
Dr. H. Lee Buchanan	1	R41 (R. Stark)	1
Directed Energy Office		R41 (R. Schneider)	25
1400 Wilson Boulevard		R41 (W. Freeman)	1
Arlington, VA 22209-2308		R41 (M. Moffatt)	1
		R43 (K. Boulais)	1
Commander		R43 (J. Choe)	1
Naval Sea Systems Command		E231	2
Attn: Code PMW-145	1	E232	3
Washington, DC 20362			
Defense Technical Information Center			
Cameron Station			
Alexandria, VA 22304-6145	12		
Library of Congress			
Attn: Gift and Exchange Division	4		
Washington, DC 20549			